

# **Empirical Aspects of a Mini-Helicon Plasma Thruster Experiment (mHTX@MIT)**

by

Joseph Eugene Palaia, IV

B.S. Electrical Engineering (2002)  
New Jersey Institute of Technology

SUBMITTED TO THE DEPARTMENT OF NUCLEAR SCIENCE & ENGINEERING  
IN PARTIAL FULFILLMENT OF THE DEGREE OF

MASTER OF SCIENCE IN NUCLEAR SCIENCE & ENGINEERING  
at the

MASSACHUSETTS INSTITUTE OF TECHNOLOGY

June 2006

© 2006 Massachusetts Institute of Technology  
All rights reserved

Signature of Author.....  
Department of Nuclear Science and Engineering  
April 1, 2006

Certified by: .....  
Manuel Martinez-Sanchez  
Professor of Aeronautics and Astronautics  
Thesis Supervisor

Certified by:.....  
Kim Molvig  
Associate Professor of Nuclear Science and Engineering  
Thesis Supervisor

Accepted by:.....  
Jeffrey Coderre  
Chairman, Department Committee on Graduate Students



# **Empirical Aspects of a Mini-Helicon Plasma Thruster Experiment (mHTX@MIT)**

by

Joseph Eugene Palaia, IV

Submitted to the Department of Nuclear Science & Engineering  
April, 2006 in Partial Fulfillment of the  
requirements for the Degree of Master of Science  
at the Massachusetts Institute of Technology

## **ABSTRACT**

A helicon plasma source experiment has been developed and then constructed in the MIT Space Propulsion Laboratory (SPL) vacuum chamber. This experiment allows study of the intrinsic advantages of efficient helicon plasma production for use in space electric propulsion. Historical helicon experiment data have been applied to help size the experiment. The goal was to create a robust and flexible experimental system which would allow optimization of the source and system parameters for efficient thrust generation, and would permit for correlation between helicon theory and experiment. This effort may lead to the development of a new electric propulsion device, the Mini-Helicon Plasma Thruster.

A design process was undertaken for the creation of this experimental setup, with the aid of a number of students and researchers at the MIT SPL. This thesis will focus on the author's specific contributions to this larger effort, which included the following elements. A survey of past helicon experiment parameters was completed, made possible largely due to the wealth of data provided by helicon plasma use in academia and for research and development. An analysis of the flow of propellant through the thruster was completed, utilizing low Mach number flow theory. A metallic structure was designed, structurally analyzed and constructed to support the electromagnets used to provide the required magnetic field. In addition, a radio frequency matching network enclosure and suitable interconnections were designed and constructed as part of the RF power delivery system.

The result of the design and construction effort is a working, reliable, and flexible helicon plasma source system. This system provides the capability for future experimentation and helicon plasma thruster development.

Thesis Advisor: Manuel Martinez-Sanchez

Title: Professor, Department of Aeronautics and Astronautics

Thesis Advisor: Kim Molvig

Title: Associate Professor, Department of Nuclear Science & Engineering





## **BIOGRAPHICAL NOTE**

Joseph Eugene Palaia, IV was born in Philadelphia, PA on October 10, 1979. He is an Eagle Scout, having been a member of Boy Scout Troop 48, Berlin, NJ. As a senior student at Eastern Regional High School in Voorhees, NJ, Joe founded a robotics team and remained a mentor on the team for the following four years. He obtained his Bachelors of Science Magna Cum Laude in Electrical Engineering from New Jersey Institute of Technology in 2002.

Joseph is a coauthor of two technical papers. The first paper, the result of a nuclear reactor design class at MIT, is titled, "Mission to Mars: How to Get There and Back with Nuclear Energy." It was published in the MIT Center for Advanced Nuclear Studies in September 2004. The second paper, the result of an eight month-pre design study in which Joseph was an active participant, is titled, "A Permanent Settlement on Mars: The Architecture of the Mars Homestead Project." It was published at the 35<sup>th</sup> International Conference on Environmental Systems in July 2005. The design study was undertaken as a project of the non-profit Mars Foundation.

From January 2005 through January 2006, Joseph held a research assistantship working on the Mini-Helicon Plasma Thruster Experiment at the MIT Space Propulsion Laboratory. The results of that effort are presented in this thesis.

In September 2005, Joseph co-founded a space commerce company, the 4Frontiers Corporation. This new company seeks to design, fund, build and operate the first permanent settlement on Mars, and to pursue the economic development of the inner solar system. Joseph will occupy the role of Vice President of Operations and R&D for 4Frontiers after completing his Masters Degree at MIT.

A more complete biography is available at [www.4Frontiers.com](http://www.4Frontiers.com).



## ACKNOWLEDGEMENTS

First I would like to thank Professor Manuel Martinez-Sanchez and Oleg Batishchev for their guidance throughout the course of this research. Their patient instruction has guided me through this work. This thesis would not have been possible without their support.

Many long days and nights of hard work were required to bring this experiment to successful operation. Many thanks go to Justin Pucci and Nareg Sinenian who worked with me for many hours on literally the nuts and bolts of it, and additionally spent much time designing, tweaking, and rebuilding. Their camaraderie and assistance will never be forgotten.

The efforts of Adam Shabshelowitz and Zach LaBry also were critical in making the experiment a success, and thanks go out to them for their hard work.

My friends in the Nuclear Engineering Department and elsewhere at MIT have helped me to get through what has been some of the most challenging years of my life thus far. I have met some truly incredible and unique people, and they have helped me through the tough times.

Tony Mavretic has been an advisor, mentor and friend for a long time now. Thank you Tony for encouraging me to apply to MIT and to strive for excellence in all that I do.

I have been most appreciative of my friends in the Mars effort for their support as I have completed this degree. All great adventures must have a beginning, and with this done, I believe Chapter 1 is finally complete.

Martha Adams provided much positive insight and helped me shape this document to what it has ultimately become. Much thanks to her for that effort.

I would like to thank my family and friends back in New Jersey, because they are much of the reason that I am where I am today. My mother and father have been incredible role models for me, and my brothers have always been there to lend their support.

Finally, I would like to thank my wife, Melissa, for putting up with my long hours away from home. She has continued to advise me and I will be forever grateful for her love and support.

This research has been supported by the Air Force, through a contract with the MIT Space Propulsion Laboratory: Theoretical and Experimental Study of Mini-Helicon Thruster. Space Systems-MIT contract (PI. Dr. O.Batishchev, AAD). Thanks to their interest in experimental aspects of this plasma thruster concept, we have been able to see the project from conception, to first plasma, to a truly robust experimental setup.



<b>Abstract</b> .....	03
<b>Biographical Note</b> .....	05
<b>Acknowledgements</b> .....	07
<b>Chapter 1. INTRODUCTION</b> .....	<b>15</b>
1.1 Requirement for New Electric Propulsion (EP) Systems.....	15
1.2 Advantages of Helicon Plasma Sources.....	16
1.3 The Mini-Helicon Plasma Thruster Experiment.....	17
1.4 Overview of Author's Contribution.....	18
<b>Chapter 2. BACKGROUND ON HELICON PLASMA APPLICATIONS</b> .....	<b>21</b>
2.1 Helicon Use in Industry.....	21
2.2 Past Experimental Investigations.....	22
<b>Chapter 3. EXPERIMENT PARAMETERS</b> .....	<b>31</b>
3.1 Experimental Subsystems.....	31
3.1.1 Experiment Schematics.....	32
3.1.2 Gas Flow System.....	33
3.1.3 Vacuum System.....	35
3.1.4 Magnetic Field Generating System.....	36
3.1.5 Control & Sensor Systems.....	37
3.2 Experiment Sizing.....	39
3.2.1 1 <sup>st</sup> Order Thrust Calculations.....	40
3.2.2 Gas Selection and Chamber Pumping Capacity.....	42
3.2.3 Plasma Containment.....	43
<b>Chapter 4. PROPELLANT FLOW MODELING</b> .....	<b>47</b>
4.1 Viscous Flow.....	47
4.2 Molecular Flow.....	56
4.3 Parametric Analysis.....	63
4.3.1 Variation of Tube Radius.....	63
4.3.2 Variation of Temperature.....	72
<b>Chapter 5. MECHANICAL SUPPORT STRUCTURE DESIGN &amp; CONST</b> .....	<b>77</b>
5.1 Structure Requirements.....	77
5.2 CAD Design.....	78
5.3 Design Modifications.....	80
5.4 Structural Analysis.....	81
5.5 Construction.....	83

<b>Chapter 6. RADIO FREQUENCY POWER SYSTEM.....</b>	<b>85</b>
6.1 Description of Experimental Configuration.....	85
6.2 Experiment Shielding and Grounding Considerations.....	86
6.3 Matching Network Enclosure.....	89
6.4 Network Tuning Procedure.....	91
<b>Chapter 7. PRELIMINARY RESULTS.....</b>	<b>95</b>
7.1 Completed Experimental Assembly.....	95
7.2 Early Plasmas in Various Operating Regimes.....	103
<b>Chapter 8 CONCLUSIONS.....</b>	<b>109</b>
8.1 Suggestions for Experiment Improvements & Future Research.....	110
<b>References.....</b>	<b>115</b>
<b>Appendix A. Experiment Component Data</b>	
<b>Appendix B. Additional Experiment CAD Drawings</b>	
<b>Appendix C. Physical Constants</b>	
<b>Appendix D. Useful Conversions and Relations</b>	

Figure 1.1	Simple Depiction of the Proposed Experimental Setup.....	17
Figure 2.1	The MORI Helicon Plasma Etching Tool.....	21
Figure 2.2	Schematic Diagram of the Vortex Helicon Etcher.....	22
Figure 2.3	Picture of the Marada Helicon Plasma Etching System.....	22
Figure 2.4	West Virginia University Space Simulation Laboratory Chamber and Helicon Plasma Source.....	24
Figure 2.5	Auburn Linear Experiment for Space Plasma Investigations (ALESPI)...	24
Figure 2.6	Helicon Plasma Facility at the University of Wisconsin-Madison.....	25
Figure 2.7	Articulated Large-area Plasma Helicon Array at New Mexico Tech.....	26
Figure 2.8	VASIMR Engine Laboratory Experiment.....	27
Figure 2.9	ORNL Helicon Antenna Installed at the Advanced Space Propulsion Laboratory (ASPL) at NASA Johnson Space Center.....	27
Figure 2.10	M2P2 Experimental Apparatus at University of Washington.....	28
Figure 2.11	Power Helicon Thruster at the University of Washington.....	28
Figure 2.12	Helicon Double Layer Thruster at the Laboratoire de Physique et Technologie des Plasmas, Ecole Polytechnique, Paris, France....	29
Figure 3.1	Subsystems Comprising the mHTX@MIT Experimental Setup.....	31
Figure 3.2	Cross Sectional Schematic of the Experiment.....	32
Figure 3.3	CAD Rendering, to Scale, of the Experimental Setup within the MIT SPL Vacuum Chamber.....	33
Figure 3.4	Gas Flow System of the mHTX@MIT.....	34
Figure 3.5	MIT SPL - ASTROVAC Block Diagram.....	35
Figure 3.6	MIT SPL – ASTROVAC System with Primary Components Labeled....	35
Figure 3.7	Cross Section of Electromagnetic Coil and Bobbin.....	36
Figure 3.8	Magnetic Field Generating System Schematic Diagram .....	37
Figure 3.9	Control & Sensor Systems of the mHTX@MIT.....	38
Figure 3.10	SPL Vacuum Chamber with Viewing Ports Indicated.....	39
Figure 4.1	Quartz Tube Component of the Mini-Helicon Thruster Experiment.....	47
Figure 4.2	Viscous Flow – Parabolic Velocity Profile Development.....	48
Figure 4.3	Mach Number vs. Distance Down the Tube.....	53

Figure 4.4	Knudsen Number vs. Distance Down the Tube, According to Viscous Flow Calculations.....	56
Figure 4.5	Free Molecular Flow Through a Tube.....	57
Figure 4.6	Pressure vs. Distance Down the Tube – for a 1.5cm Radius, 25cm Long Tube.....	59
Figure 4.7	Mach Number vs. Distance Down the Tube – for a 1.5cm Radius, 25cm Long Tube.....	60
Figure 4.8	Number Density vs. Distance Down the Tube – for a 1.5cm Radius, 25cm Long Tube.....	61
Figure 4.9	Knudsen Number vs. Distance Down the Tube – for a 1.5cm Radius, 25cm Long Tube.....	62
Figure 4.10	Tube Outlet Pressure vs. Tube Radius, $M=1$ at Outlet Boundary Condition.....	63
Figure 4.11	Knudsen Number at Tube Outlet vs. Tube Radius, $M=1$ at Outlet Boundary Condition.....	64
Figure 4.12	Knudsen Number at Tube Inlet vs. Tube Radius, Assume All Molecular Flow.....	65
Figure 4.13	Pressure vs. Distance Down the Tube – for Various Tube Radii.....	66
Figure 4.14	Pressure vs. Distance Down the Tube for Various Radii – Including Both Molecular and Transition Regions.....	70
Figure 4.15	Mach Number vs. Distance Down the Tube for Various Radii – Including Both Molecular and Transition Regions.....	70
Figure 4.16	Number Density vs. Distance Down the Tube for Various Radii – Including Both Molecular and Transition Regions.....	71
Figure 4.17	Knudsen Number vs. Distance Down the Tube for Various Radii – Including Both Molecular and Transition Regions.....	71
Figure 4.18	Tube Outlet Pressure vs. Gas Temperature, $M=1$ at Outlet Boundary Condition.....	73
Figure 4.19	Pressure vs. Distance Down the Tube – for Various Gas Temperatures...	74
Figure 4.20	Mach Number vs. Distance Down the Tube – for Various Gas Inlet Temperatures.....	75



Figure 4.21	Number Density vs. Distance Down the Tube – for Various Gas Inlet Temperatures.....	75
Figure 5.1	Electromagnetic Coil on Aluminum Bobbin.....	77
Figure 5.2	CAD Rendering of Experiment Setup.....	78
Figure 5.3	CAD Rendering of Proposed Mechanical Support Structure, Side and Front Views.....	79
Figure 5.4	CAD Rendering of Proposed Mechanical Support Structure Components, Top and Bottom Plates.....	79
Figure 5.5	CAD Rendering Showing the Proposed Plume Swing Arm in its Maximum Angular Displacement.....	80
Figure 5.6	CAD Rendering of Mechanical Support Structure, Side View. Additional Cross Beam Location Indicated.....	81
Figure 5.7	Simplified Model of the Mechanical Support Structure.....	81
Figure 5.8	Cross Section of the Support Beam, Dimensions in mm.....	82
Figure 5.9	Assembled Mechanical Support Structure, Installed in SPL Vacuum Chamber.....	84
Figure 6.1	RF Power Delivery Subsystem of the mHTX@MIT.....	85
Figure 6.2	RF Shielding Braid - Covering Thermocouple Wires.....	86
Figure 6.3	Low Impedance Chamber Grounding Strap.....	87
Figure 6.4	RF Shielding Mesh, Placed Over Chamber View Ports.....	88
Figure 6.5	Basic Impedance Matching Circuit.....	89
Figure 6.6	CAD Rendering of Matching Network.....	89
Figure 6.7	CAD Diagram of Matching Network with Labeled Components.....	90
Figure 6.8	Matching Network Mounted to the SPL Vacuum Chamber.....	92
Figure 6.9	Resistive Divider Used During Network Tuning.....	92
Figure 7.1	Experimental Apparatus of the mHTX@MIT.....	95
Figure 7.2	Electrical Feedthrough for Electromagnet Power Supply.....	96
Figure 7.3	Electromagnet DC Power Supplies.....	96
Figure 7.4	Electrical Feedthrough for Various Sensors.....	97
Figure 7.5	Side of SPL Vacuum Chamber Showing Matching Network, Electromagnet Power Supply Feedthrough and Sensor Feedthrough.....	97

Figure 7.6	Gas Flow System, Including Mass Flow Controller.....	98
Figure 7.7	Custom Coaxial Cable, Connected to 8 Inch Reducing Flange.....	98
Figure 7.8	Coaxial RF Connection with Ground Strap and Teflon Gap Spacer Shown.....	99
Figure 7.9	Coaxial RF Connection with Ground Strap and Teflon Spacers.....	100
Figure 7.10	Copper Helicon Antenna, with Tape Measure for Scale.....	100
Figure 7.11	Helicon Antenna Installed in Experimental Setup.....	101
Figure 7.12	Helmholtz Pair of Electromagnetic Coils, With Quartz Tube and Helicon Antenna Visible Along Their Axis.....	101
Figure 7.13	Experimental Apparatus of the mHTX@MIT.....	102
Figure 7.14	First Plasma of the mHTX@MIT, as Viewed from the Chamber Side View Port. 40W, N <sub>2</sub> , 10 sccm, ICP.....	103
Figure 7.15	First Plasma, as Viewed from Chamber End View Port. 40W, N <sub>2</sub> , 10 sccm, ICP.....	103
Figure 7.16	Plasma Discharge, ~450W, N <sub>2</sub> , 8 sccm, ICP.....	105
Figure 7.17	Helicon Discharge ~700W, N <sub>2</sub> , 8 sccm, ~1500G.....	105
Figure 7.18	Color and Intensity Change Indicative of a Mode Change to Helicon Wave Propagation. ~700W, N <sub>2</sub> , 8 sccm, ~1500G.....	106
Figure 7.19	Abnormal Operation - Glow Discharge Visible Within the Entire Vacuum Chamber.....	107
Figure 7.20	Helicon Discharge with Visible Plume, ~500W, Ar, 20 sccm, ~850G...108	
Figure 7.21	Helicon Discharge with Concentrated Plume, ~500W, Ar, 20 sccm, ~2200G.....	108
Table 2.1	Comparison of Experiment Parameters in Various Helicon Apparatus...23	
Table 4.1	Molecular to Transitional Flow Regime – Transition Distances and Pressures for Three Different Tube Radii.....	66
Table 4.2	Pressures Calculated in Transitional Flow Regime for Three Different Tube Radii.....	69
Table 4.3	Variation of Gas Characteristics with Inlet Temperature.....	73

# Chapter 1

## INTRODUCTION

A laboratory experimental apparatus has been developed and constructed at the MIT Space Propulsion Laboratory to investigate the application of a helicon plasma source for space propulsion. Elements of the apparatus design and construction are the subject of study in this present thesis. An overview of the need for new electric propulsion systems such as the mini-Helicon Plasma Thruster, is presented as an introduction. Some of the advantages of helicon plasma sources are presented, followed by a brief description of the experimental apparatus and of the author's contribution to the larger effort.

### 1.1 Requirement for New Electric Propulsion (EP) Systems

Existing and new space efforts call for the use of propulsion systems meeting various design requirements. Many applications call for propulsion systems whose requirements match those afforded by electric propulsion systems. These requirements typically include high specific impulse (ISP), low thrust, and long operating lifetime; and mission applications include, "stationkeeping, drag compensation, attitude control, station repositioning, orbit transfer/raising, and for trajectory control and maneuvering of interplanetary spacecraft" [Filliben, 1996B]. New and innovative technologies are being explored, both to provide new thruster solutions and to improve existing designs.

Advanced propulsion systems are being sought by NASA and other governmental space agencies to, "...allow more exhaustive, long-term surveys of planets and their moons, as well as comets, asteroids, and other bodies..." [David, 2002]. In this vein, research efforts are being focused on a number of propulsion technologies including next generation electric propulsion systems. "High throughput, lightweight and more powerful ion engines, for example, enable a host of future space missions, including a Europa Lander, a Saturn Ring Observer, a Neptune Orbiter, and a Venus Surface Sample Return probe..." [David, 2002]

New and improved electric propulsion systems are also being pursued by the commercial sector. Hughes Corporation has introduced new xenon ion propulsion systems for use in commercial satellite stationkeeping. [Sankovic, 2002]. Arcjet thrusters and pulsed plasma thrusters have been launched by Japanese public and private efforts [Filliben, 1996A]. "Hall thrusters are routinely used on Russian communication satellites for both East-West and North-South Stationkeeping" [Sankovic, 2002]. These are but a few examples of electric propulsion system use by the commercial sector, and with recent increased interest in commercial space efforts, the need for these systems is expected to increase.

Finally, the military has shown recent interest in pursuing new electric propulsion systems. Commercial applications have focused on using propulsion systems in high power

communication satellites, whereas many future military satellites offer lower power levels for use with the propulsion system. McFall et al. state that, "...the development of high performance, low power thrusters is important to the support of Air Force missions," and that, "the use of electric propulsion for stationkeeping and orbit repositioning missions offers significant advantages to Air Force users" [McFall, 1995]. This interest is further illustrated by Air Force support of this thesis research on the creation of an experimental apparatus for use in developing a new space electric thruster.

Existing electric propulsion systems suffer from a variety of limitations, which are described for a number of different systems by Martinez-Sanchez and Pollard [Martinez-Sanchez, 1998]. The majority of these existing systems share common limitations. Many systems utilize expensive heavy fuels such as xenon and krypton. Many suffer from a high cost of electron-ion pair production and a low percentage of propellant ionization. Finally, virtually all existing systems suffer from limited operation lifetime due to electrode sputtering and degradation. Thus there exists a need for new electric propulsion systems which do not suffer from these limitations.

## 1.2 Advantages of Helicon Plasma Sources

There is much information in the literature describing helicon theory and application in industry. Historically, helicon sources have been utilized in many semiconductor manufacturing applications, due to their ability to yield plasmas of high density and uniformity [Chen, 1997]. Chen states that with helicon discharges, "...plasma densities  $n$  achieved are almost an order of magnitude higher than in other discharges at comparable pressures and input powers" [Chen, 1996]. Helicon plasmas with densities up to  $10^{12} \text{ cm}^{-3}$  and uniformities of +/-3% have been produced for use in materials processing devices [Chen, 2001]. Chen also states that the reasons for this increased density in helicon sources are yet to be satisfactorily explained.

Much work is being done to further theoretical studies of helicon plasmas. Justin Pucci presents an overview of present knowledge in his work, "Helicon Wave Theory: Current Understanding." In this work, it is stated that, "helicon waves are a special case of the right-hand circularly polarized (RCP) electromagnetic wave in that they propagate only in bounded magnetized media." In the present experimental apparatus, this environment is provided by use of a quartz tube and applied axial magnetic field to achieve plasma containment. Further, Pucci explains how helicon plasmas are produced:

"Helicon plasmas are produced in cylindrical geometries with a DC magnetic field applied along the z-axis. The gas is first weakly ionized by the electrostatic antenna voltages and then circularly polarized helicon waves are launched into the plasma as a result of the application of the magnetic field. The plasma is then further ionized from conversion of the wave energy to particle energy. However, since helicon waves are only weakly damped, the mechanism of conversion from wave energy to particle energy is still a much debated topic. It is thought that there is a coupling between the helicon wave and an electron cyclotron mode at the boundary of the cylinder. The Trivelpiece-Gould (TG) mode, as it is referred to, is then

responsible for deposition of energy to the plasma resulting in ionization.” [Pucci, 2004]

Whichever mechanism is ultimately found responsible for energy deposition into the plasma, the fact remains that electromagnetic waves are emitted by the helical antenna which does not make contact with the produced plasma. The antenna and plasma are isolated by the applied magnetic field. Thus helicon sources do not suffer from electrode wear commonly found in capacitively coupled plasma sources.

Helicon sources produce more plasma at a given power than other RF and DC source configurations, operate utilizing light gases, and result in no erosion of operational components. These characteristics seem to indicate that application of this technology to space electric propulsion may be desirable.

### 1.3 The Mini-Helicon Plasma Thruster Experiment

A laboratory experimental apparatus has been constructed, called the Mini-Helicon Plasma Thruster Experiment (mHTX). Work based upon this experiment, consisting of theoretical and experimental investigations by a number of students, is being conducted at the MIT Space Propulsion Laboratory (SPL). The Principal Investigator of this research is Oleg Batishchev, Principal Research Scientist in the MIT Department of Aeronautics and Astronautics. The research is being conducted in coordination with SPL director and MIT Professor of Aeronautics and Astronautics, Manuel Martinez-Sanchez.

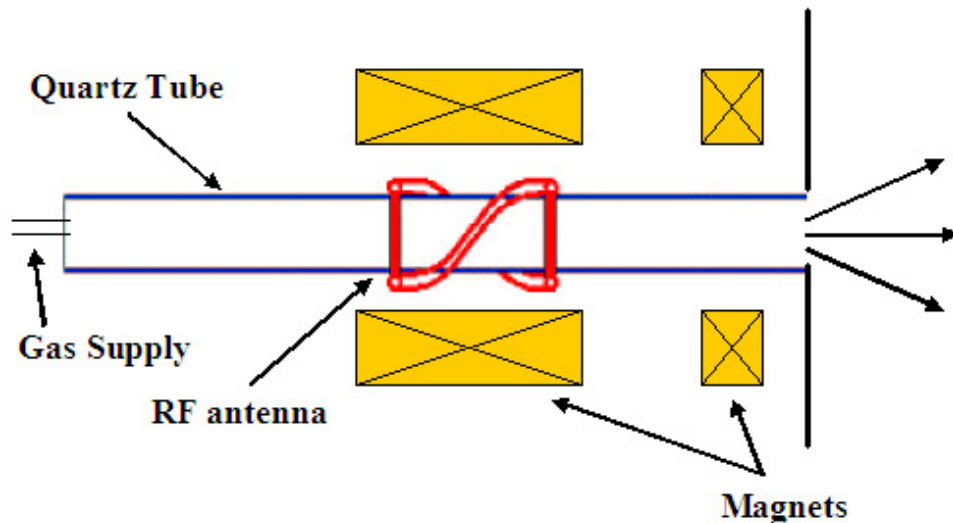


Figure 1.1 Simple Depiction of the Proposed Experimental Apparatus

The core elements of the experimental apparatus are illustrated in Figure 1.1 above. The apparatus consists at its core of a quartz tube. This tube is connected at one end to a gas supply system which delivers a regulated flow of thruster propellant to the experiment. The opposite tube end exhausts into the vacuum chamber. Surrounding this tube is a helicon antenna which transfers radio frequency power into the gas flowing through the

system, resulting in plasma formation. Surrounding the tube and antenna is an electromagnet system, which provides an axial magnetic field. This field contains the plasma and is required to achieve helicon wave coupling between the antenna and the gas flow.

The experimental apparatus is described in more detail in various sections of this thesis. Chapter 3 provides an overview of the experiment subsystems, providing overall experiment schematics as well as detail on the gas flow, vacuum, magnetic field generating, and control and sensor subsystems. Chapter 5 describes in detail the mechanical support structure. Chapter 6 describes the radio frequency power delivery system. A discussion and pictures of the completed experiment apparatus are provided in Section 7.1.

There are many potential advantages of applying a helicon plasma source to a space electric propulsion system. These include:

- Operation using light, inexpensive gases ( $H_2$ ,  $H_2O$ ,  $H_2O_2$ , etc.).
- Low cost of electron-ion pair production.
- Intrinsically longer operating life due to its electrode-less, inductively coupled source.

The experimental apparatus provides control of a number of parameters. These include:

- RF power level, (10 - 1000 W).
- Propellant gas, ( $N_2$  & Ar, followed by other gases and mixtures).
- Propellant flow rate, (0 - 100 sccm).
- Axial magnetic field amplitude and profile (0-2400G).
- Quartz tube diameter (tubes may be swapped between runs).
- Antenna geometry (antennas may be swapped between runs).

## 1.4 Overview of Author's Contribution

The development and construction of the mHTX@MIT experimental apparatus has been the combined effort of a number of students in the MIT Space Propulsion Laboratory. Acknowledgements will be made throughout this thesis for work performed by other students. Clear distinction will be made regarding the author's work and that of others.

Some efforts were undertaken prior to the author's initial participation in the project in January 2005. Prior to this time, MIT graduate student Justin Pucci examined helicon plasma mathematical theory in some detail. An exposition of this work can be found in his paper, "Helicon Wave Theory: Current Understanding" [Pucci, 2004]. Also, two electromagnets for use in the experiment, were designed, built and tested by MIT undergraduate students Loretta Trevino and Adam Shabshelowitz. These electromagnets, while ultimately not used in the experimental apparatus, yielded much insight into coil design and manufacture which was applied to the actual coils used in the experiment.

Between January and June 2005, the author performed background research on past helicon experimental investigations in order to gain insight which could be applied to the design and operation of the mHTX@MIT experimental apparatus. Some initial calculations were also carried out during this time period in order to aid in sizing the experiment.

Beginning in June 2005 the work focus shifted from theoretical to experimental studies, and additional students began to work on the experimental aspects of the project. These students included Justin Pucci and Adam Shabshelowitz (mentioned earlier) as well as Nareg Sinenian and Zach LaBry. The author worked with these students to design, construct, and test the operation of the experimental apparatus.

Specific contributions of the author during this time period included the following:

- Collection and comparison of background data on helicon sources, both in experimental and industrial applications. (Chapter 2)
- Creation of CAD renderings which aided in the development of the experiment. (Section 3.1.1)
- 1<sup>st</sup> order thrust calculations, an estimate of chamber pumping capacity and plasma containment calculations. (Section 3.2)
- Propellant flow modeling. (Chapter 4)
- Design, CAD rendering, analysis and construction of the mechanical support structure. (Chapter 5)
- Aided in the construction of the custom RF connection. (Sections 6.1, 7.1)
- Installation of chamber grounding system. (Section 6.2)
- Design, CAD rendering, and construction of the matching network enclosure. (Section 6.3)
- Development of matching network tuning procedure. (Section 6.4)
- Acquisition of various components of the experimental apparatus including the RF generator.
- Aided in the construction and installation of various components of the experimental apparatus.
- Aided in the troubleshooting of various elements of the experimental apparatus including sensor and control systems, RF connections, and matching network tuning.
- Aided in the operation of the experimental apparatus for preliminary data collection.





# Chapter 2

## BACKGROUND ON HELICON PLASMA APPLICATIONS

### 2.1 Helicon Use in Industry

Due to the advantages outlined in Section 1.3, helicon plasma sources find application in the semiconductor industry. There they are used to generate plasma in systems performing material deposition and etching processes. Helicon sources are also being investigated for application in waste abatement systems, where the energetic plasma produced breaks down complex polluting species.

Two commercially sold helicon plasma sources are presently used in the semiconductor industry. The first is the M=0 Reactive Ion etcher, originally sold as the MORI 200. It was developed and produced by Plasma and Materials Technologies, Inc., was later produced by Trikon Technologies, Inc., and is presently produced by Aviza Technology Inc. of Scotts Valley, California. A schematic of the MORI etching tool is presented in Figure 2.1 below.

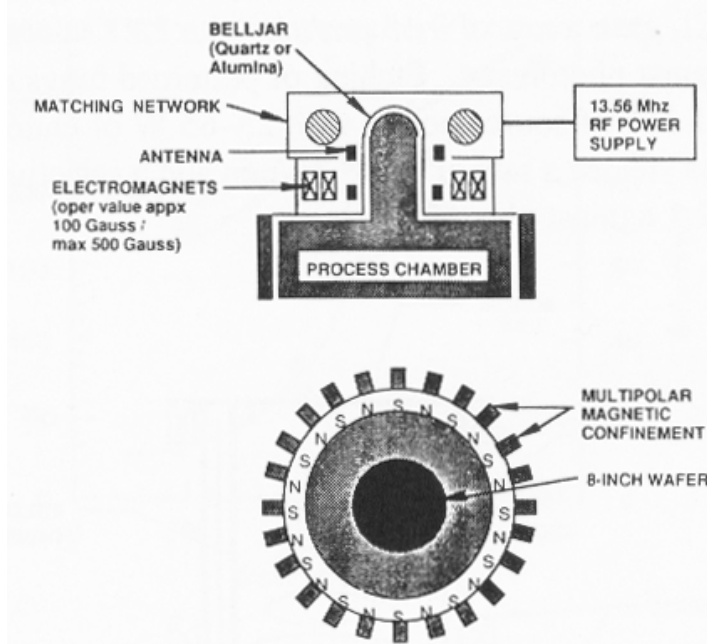


**Figure 2.1** The MORI Helicon Plasma Etching Tool [Campbell, 1992]

The second helicon plasma source used in industry is no longer commercially available. This was a system produced by Lucas Signatone Corporation of Sunnyvale California. It was sold as both the Vortex and the Marada helicon etcher. Figure 2.2 shows a schematic diagram of the Vortex helicon etcher and Figure 2.3 shows the Marada helicon etcher.

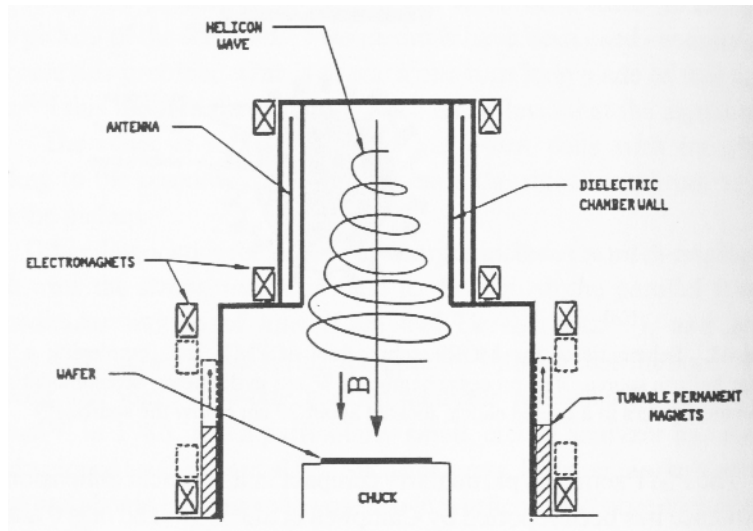


**Figure 2.2** Schematic Diagram of the Vortex Helicon Etcher. [Chapman, 1991]

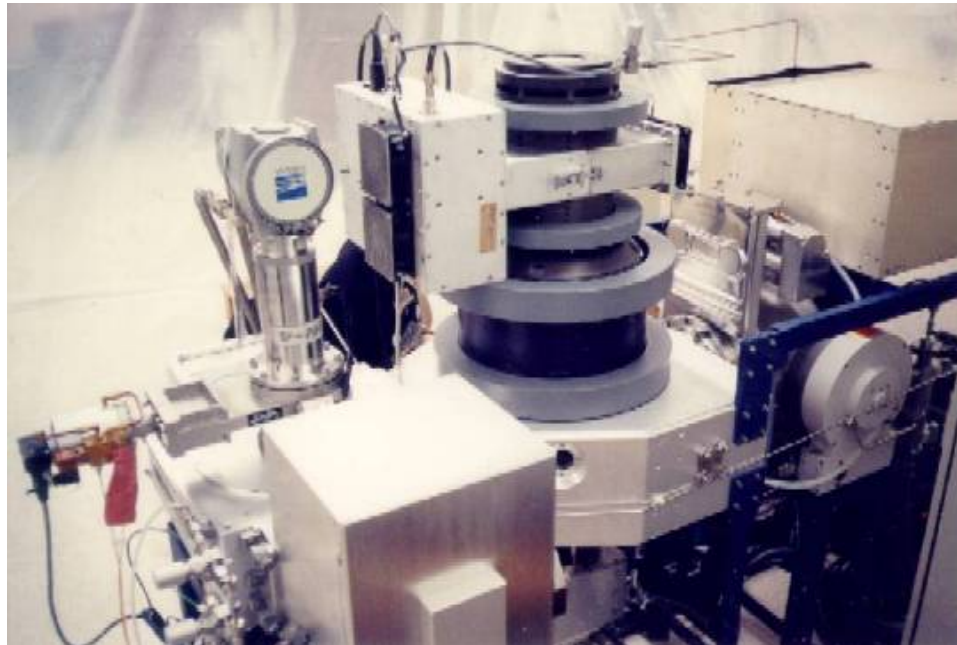


**Figure 2.3** Picture of the Marada Helicon Plasma Etching System. [Schofield, 2001]

## 2.2 Past Experimental Investigations

Numerous helicon sources have been utilized in experimental investigations. A number of these investigations are mentioned and compared here, to provide a frame of reference for the MIT mini-Helicon Plasma Thruster experiment. Information from some of these investigations has aided in sizing the present apparatus. A sampling of experimental investigations and some of their parameters is shown in Table 2.1 below, with the mHTX@MIT included for comparison.

Experiment	Helicon Power Level	Helicon Source Freq (MHz)	Gas(s)	Gas Flow Rate or fill pressure	Applied axial B-Field (G)	Quartz Tube Dia (cm)	Quartz Tube Length (cm)	Helicon Antenna(s)	Te (eV)	Source
ALESPI	500 W	10	Argon, Helium	4 mTorr	0 to 1000	10	250	Helical		[ALESPI, 2001]
ALPHA - NMT	5kW ea		Argon, Helium	5 mTorr	0-2000	50	400	7 helicon sources	3	[Watts, 2001]
Chi-Kung	250W and 800W	13.56	Argon	3 mTorr	90	15	32	Double saddle		[Charles, 2000]
Chi-Kung	250	13.56	Argon	0.35 mTorr	250	15	32	Double saddle	8-10	[Charles, 2004B]
Chi-Kung	800	13.56	Argon	0.3 mTorr	250	15	32	Double saddle		[Charles, 2004A]
Helicon Plasma Etching Reactor	3kW	13.56	Argon	2.5 mTorr	60	15	25	double loop (m=1)		[Perry, 2002]
HELIX / LEIA - WVU		0.3 - 35	Argon	2.2 mTorr	700		160		5	[Scime, 2000]
HPRL @ UWM	1.3kW	13.56	Argon, Nitrogen	3 mTorr	0 to 1000	10	175	half-turn double helix antenna	3.5 - 4.3	[UWM, 2002], [Tysk, 2004]
mHTX@MIT	800W	13.56	Nitrogen, Argon	10 sccm	0 to 2500	2	25	RH Helical		
Unnamed Exp A	2kW	27.12	Argon fill	15 mTorr	800	5	160	Nagoya Type III, RH and LH Helical antennas		[Chen, 1996]
Unnamed Exp B		13.56			100 & 50	10	200	Single Loop	2.5 - 4	[Chen, 2003]
Unnamed Exp C	800W	31.2	Argon	4 mTorr	0 to 1000	2	90	Half wavelength, m=1. 12cm long		[Chen, 1992]
VASIMR	20kW	13.56	Deuterium, Helium		1500	9	107	10cm long double saddle		[Squire, 2004]
VASIMR	up to 3.5kW	25	Helium	110 sccm	800	9	107	10cm long double saddle		[Boswell, 2004]
WOMBAT	2kW	13.56	Argon	0.5 to 3 mTorr	20 to 150	18	50	Double saddle, double half-turn		[Degeling, 1997]

WOMBAT = Waves on Magnetized Beams and Turbulence  
VASIMR = Variable Specific Impulse Magnetoplasma Rocket

**Table 2.1** Comparison of Experiment Parameters in Various Helicon Apparatus

Several universities and research centers are presently investigating use of helicon discharges for a number of different applications. It is hoped that insight gained through examination of other helicon sources in academic and R&D settings can be applied to improving the design and operation of the mHTX@MIT experimental apparatus.

### West Virginia University - Hot hELIcon eXperiment (HELIX) & Large Experiment on Instabilities and Anisotropies (LEIA)

The Hot hELIcon eXperiment (HELIX) and Large Experiment on Instabilities and Anisotropies (LEIA) both utilize the same experimental apparatus at the West Virginia University Space Simulation Laboratory. This experimental apparatus has been designed to provide the capability to perform a number of plasma experimental investigations, and operates under steady state conditions. The apparatus provides, “high beta (high plasma pressure compared to magnetic pressure) plasmas such as those found in the magnetosphere or in fusion experiments,” and also in provides, “capability for additional ion heating - required for our investigations of ion temperature anisotropy driven instabilities” [HELIX, 2000]. Some experimental parameters are included in Table 2.1 above. Additionally the experimental setup is depicted in Figure 2.4 below.

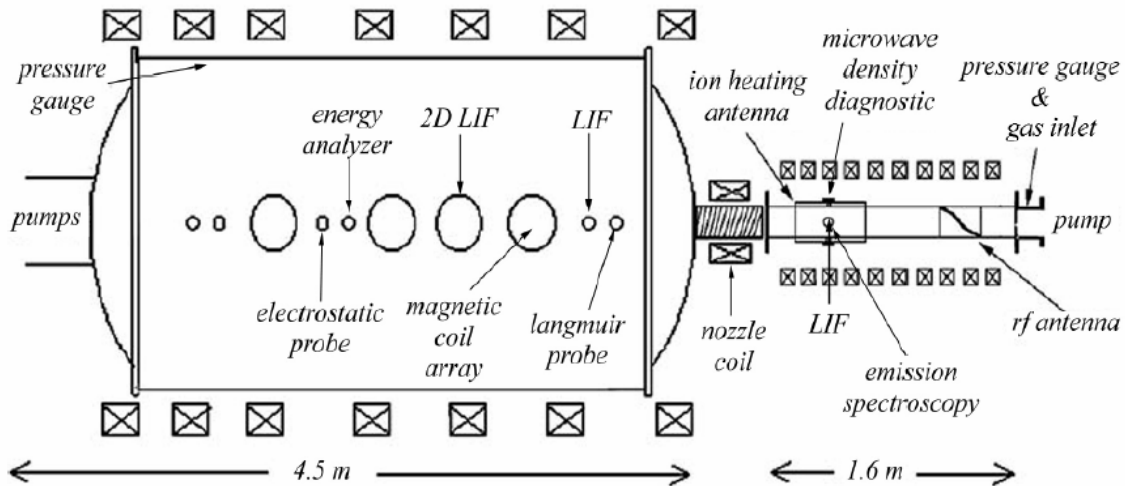


**Figure 2.4** West Virginia University Space Simulation Laboratory Chamber and Helicon Plasma Source. [Scime, 2000]

Auburn University – Auburn Linear Exp. for Space Plasma Investigations (ALESPI)

The Auburn Linear Experiment for Space Plasma Investigations (ALESPI) utilizes an experimental apparatus at Auburn University in Auburn, AL. The apparatus, which is designed to operate under steady state conditions, is used to investigate a number of space plasma phenomena by exploring, “individual processes thought to contribute to the complex interactions in space. These processes include Double Layers and Alfvén waves” [ALESPI, 2001]. Additional investigations will utilize Electron Cyclotron Heating. Some experimental parameters are included in Table 2.1 above, and the experimental setup is depicted in Figure 2.5 below.

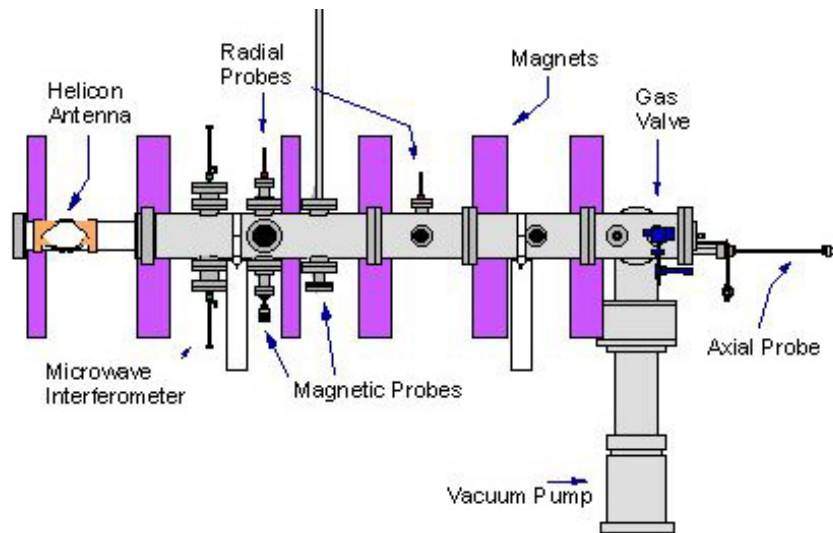


**Figure 2.5** Auburn Linear Experiment for Space Plasma Investigations (ALESPI) [ALESPI, 2001]

University of Wisconsin at Madison - Helicon Plasma Research Laboratory

The Helicon Plasma Research Laboratory utilizes an experimental apparatus at the University of Wisconsin at Madison. The apparatus, which operates using 13.56 MHz RF that is pulsed at 6 ms pulse width and 10% duty cycle, is used to perform a number of investigations. Topics include, “basic antenna coupling, plasma wave, plasma heating and optical emission research relevant to these very efficient plasma sources” [UWM, 2002]. Some experimental parameters are included in Table 2.1 above, and the experimental setup is depicted in Figure 2.6 below.

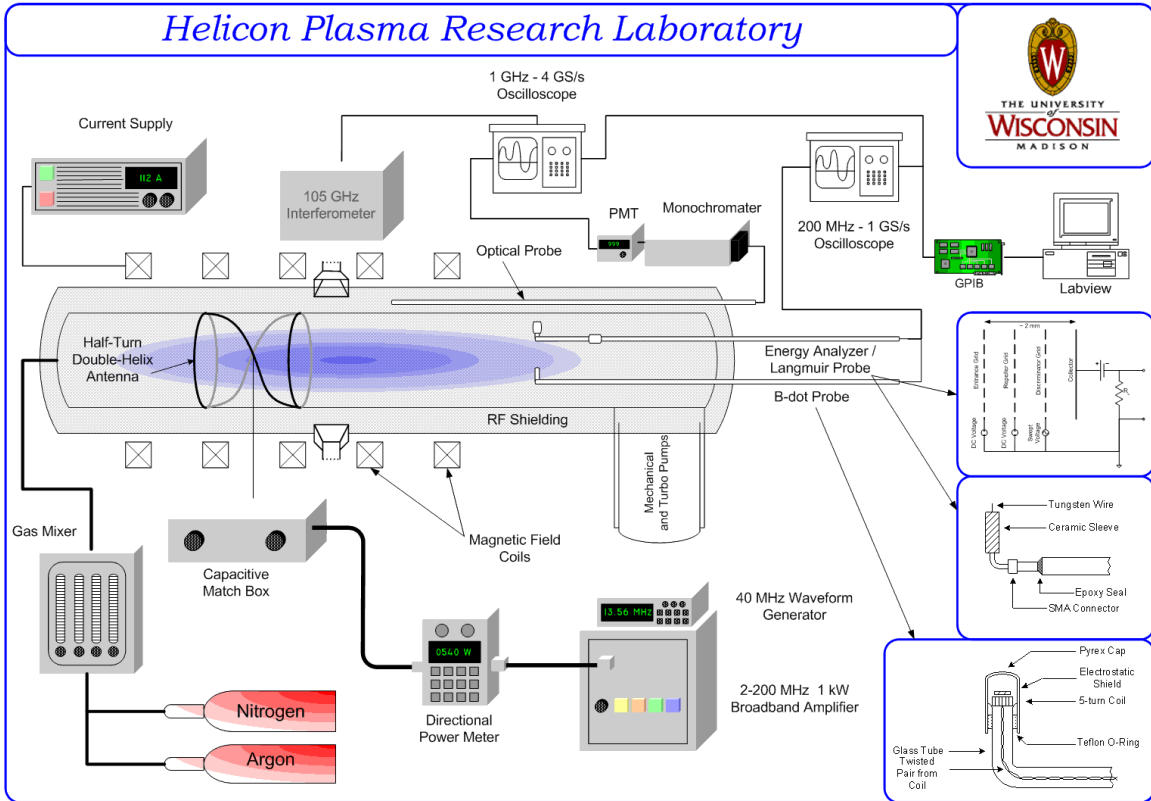


**Figure 2.6** Helicon Plasma Facility at the University of Wisconsin-Madison [UWM, 2002]

New Mexico Tech - Articulated Large-area Plasma Helicon Array (Alpha)

The Articulated Large-area Plasma Helicon Array (Alpha) utilizes an experimental apparatus at New Mexico Institute of Technology. This apparatus includes an array of seven helicon antennas, which may operate simultaneously creating a large plasma volume, or may be operated as separate plasma columns. Experimental investigations seek insight into, “the dynamics of solar flares and mechanisms responsible for the formation of Earth's aurora.” Early studies have included Alfvén wave investigations. Some experimental parameters are included in Table 2.1 above, and the experimental setup is depicted in Figure 2.7 below.



**Figure 2.7** Articulated Large-area Plasma Helicon Array at New Mexico Tech  
[Watts, 2001]

### **Application to Space Propulsion Systems**

A number of organizations are investigating the application of helicon plasma sources to space propulsion systems. These include the Variable Specific Impulse Magnetoplasma Rocket (VASIMR) program at the Advanced Space Propulsion Lab (ASPL) of NASA Johnson Space Center, the Mini-Magnetospheric Plasma Propulsion (M2P2) experiment and High Power Helicon (HPH) Plasma Thruster at the University of Washington, and the Helicon Double Layer Thruster being developed by the Australian National University.

### **Variable Specific Impulse Magnetoplasma Rocket (VASIMR)**

The Variable Specific Impulse Magnetoplasma Rocket (VASIMR) has been under development at the NASA Johnson Space Center - Advanced Space Propulsion Lab for many years. It consists of three main sections. In the first section, a helicon antenna produces plasma from a neutral gas, typically hydrogen or deuterium. Additional energy is then added to the plasma by Ion Cyclotron Resonant heating. The plasma is then expanded through a magnetic nozzle which converts radial plasma motion into axial thrust. A depiction of the VASIMR experimental apparatus is provided in Figure 2.8 below, and some experimental parameters are provided in Table 2.1.

The VASIMR program utilizes a helicon antenna provided by Oak Ridge National Labs (ORNL). That antenna, and antennas of identical design, have been used at ORNL for various studies of light ion heating and arc formation [ORNL, 2001]. The antenna is pictured in Figure 2.9 below.



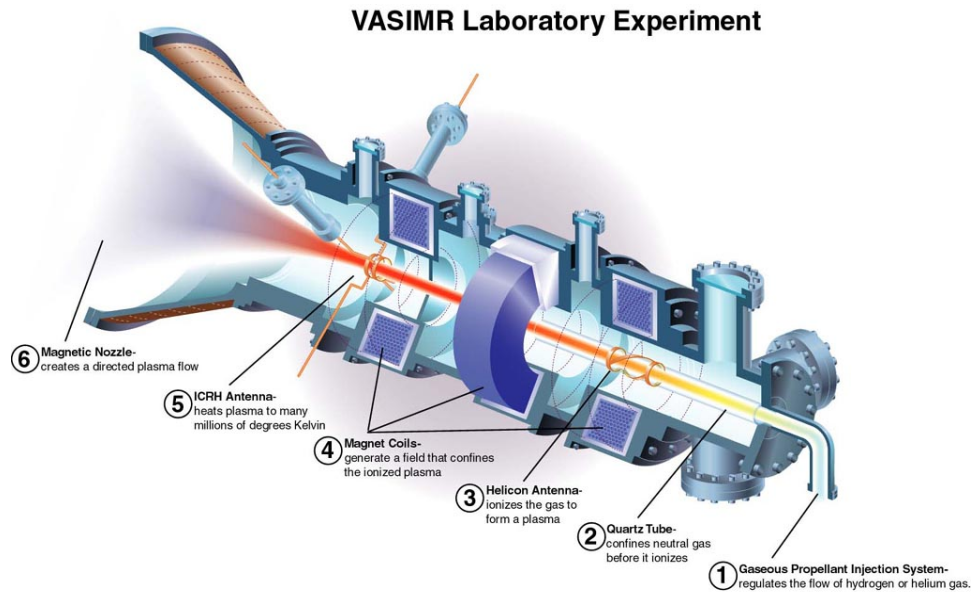


**Figure 2.8** VASIMR Engine Laboratory Experiment [ASPL, 2003]

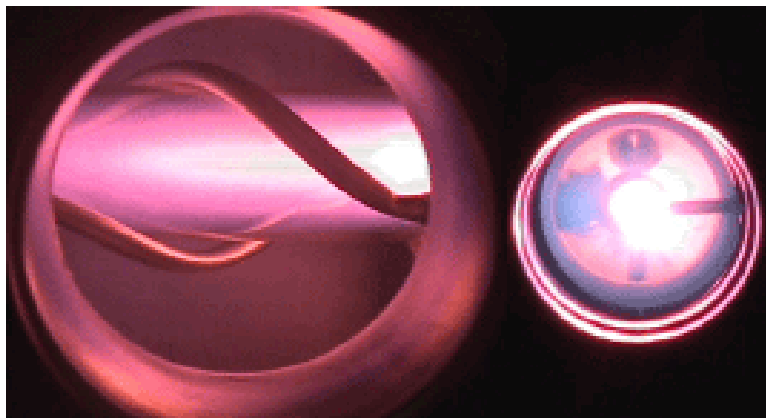


**Figure 2.9** ORNL Helicon Antenna Installed at the Advanced Space Propulsion Laboratory (ASPL) at NASA Johnson Space Center. [ORNL, 2001]

It should be noted that the potential exists to utilize a small scale helicon plasma source to gain insight into the design and operation of larger systems, like that used in the VASIMR program. It is known that the development and testing of these large systems can be both complex and costly. It is hoped that the mHTX@MIT experiment will yield this insight into larger helicon systems, through relatively low cost and effort.

#### Mini-Magnetospheric Plasma Propulsion (M2P2)

The Mini-Magnetospheric Plasma Propulsion (M2P2) experiment is being developed at the University of Washington. The M2P2 system uses the interaction between a spacecraft generated magnetic bubble, or mini-magnetosphere, and the high speed solar wind to generate thrust. Plasma generated by a helicon source is injected into the spacecraft's magnetic fields to generate this mini-magnetosphere. With the M2P2, the energy of the solar wind is utilized as in a more conventional solar sail, but material and

deployment issues are eliminated. High specific impulses are predicted since no onboard propellant is necessary. The experimental apparatus of the M2P2 is depicted in Figure 2.10 below.



**Figure 2.10** M2P2 Experimental Apparatus at University of Washington. [M2P2, 2001]

### High Power Helicon (HPH) Plasma Thruster

Another space propulsion experiment utilizing a helicon plasma source is being conducted at the University of Washington, this being the High Power Helicon (HPH) Plasma Thruster. The experiment, which is pictured during operation in Figure 2.11 below, is designed to operate with many different propellants at power levels between 10 and 100 kW, and with a force generation of several Newtons. The HPH, like the mHTX@MIT, seeks to utilize the advantages provided by helicon plasma sources to create an innovative space propulsion system. The mission applications of this thruster would be different from those of the mHTX, due to its higher thrust levels and power requirements.



**Figure 2.11** High Power Helicon Thruster at the University of Washington. [HPHT, 2004]



## Helicon Double Layer Thruster

The Helicon Double Layer Thruster is being developed by the Space Plasma Power and Propulsion group of the Australian National University, in collaboration with the European Space Agency. The device involves the creation of a double layer, which is described on the HDLT webpage. “This double layer can be thought of as a thin standing shock wave across which there exists a strong electric field gradient. It is this electric field that accelerates ions from the source plasma to very high exhaust velocities creating thrust” [HDLT,2004]. Present focus is on optimizing this double layer, which is spontaneously created when certain parameters are met within the plasma. The thruster would find use in applications similar to those of the mHTX@MIT.

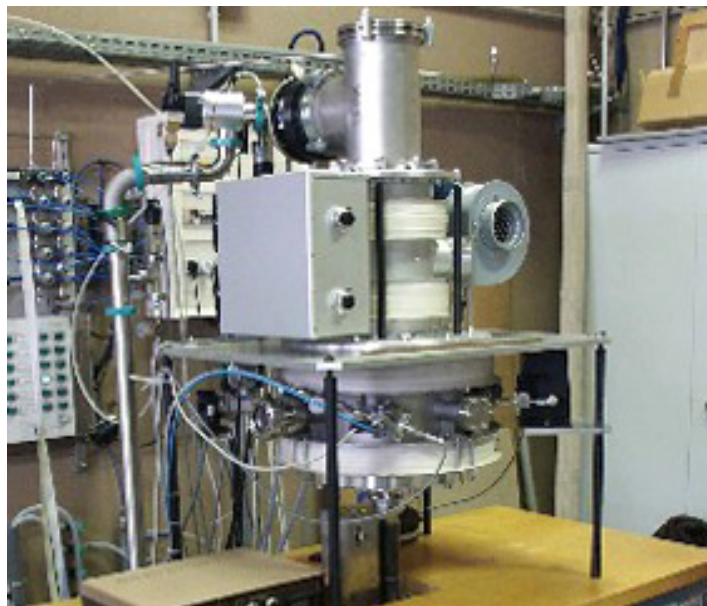


**Figure 2.12** Helicon Double Layer Thruster at the Laboratoire de Physique et Technologie des Plasmas, Ecole Polytechnique, Paris, France. [ESA, 2005]



# Chapter 3

## EXPERIMENT PARAMETERS

The experiment scope was to design, construct and operate a laboratory experiment to validate theoretical investigations in small-scale helicon discharges, and further, to provide a test bed through which optimization of helicon source design and overall thruster design can be achieved. In order to accomplish this, a system of systems approach was taken. The total experiment was broken down into a number of subsystems, each with its own respective subcomponents. Each of these systems was sized according to various constraints, including desired thruster characteristics, requirements for a helicon discharge, and limitations of available hardware.

### 3.1 Experiment Subsystems

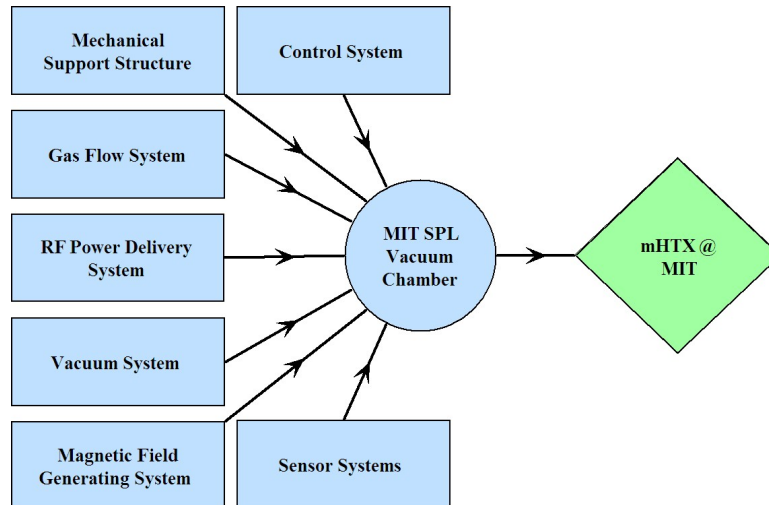


**Figure 3.1** Subsystems Comprising the mHTX@MIT Experimental Setup

The experimental setup consists of a number of subsystems, each with its own subcomponents, as illustrated in Figure 3.1 above. These include the mechanical support structure, the gas flow system, the RF power delivery system, the vacuum system, the magnetic field generating system, the control system, and various sensor systems. These systems have been integrated, taking into account the constraints imposed by our use of the MIT Space Propulsion Laboratory vacuum chamber and laboratory resources.

This section describes the various components and subcomponents of the experiment in a general sense. The actual components used are shown in Chapter 5 for the mechanical support structure, Chapter 6 for the RF power delivery system, and in Section 7.1. Part numbers, model numbers and other detailed information for various pieces of equipment and materials used in the experimental setup are provided in Appendix A. Fully

dimensioned CAD drawings of the most critical experiment components are provided in Appendix B.

### 3.1.1 Experiment Schematics

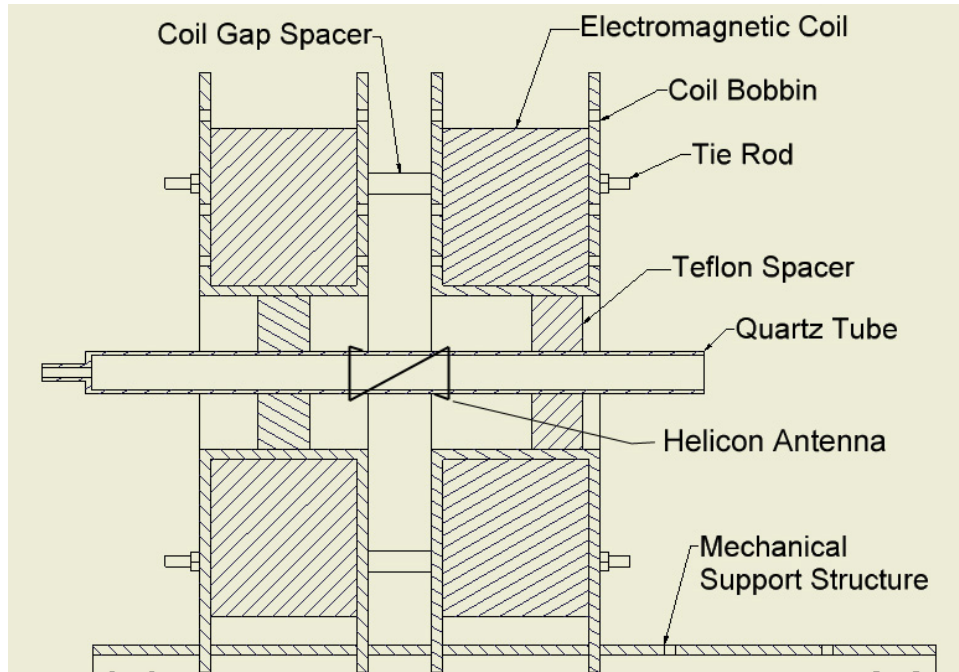


**Figure 3.2** Cross Sectional Schematic of the Experiment

The experimental apparatus consists at its core of a quartz tube. This tube opens at one end into the SPL vacuum chamber. The other end of the tube terminates in an electrically floating stainless steel Swagelock fitting, which is then connected to a plastic tube. This plastic tube leads to gas metering hardware for the delivery of regulated gas flow (i.e. thruster propellant).

Surrounding the quartz tube is a right hand (RH) helical antenna which transfers energy to the gas flowing through the system, resulting in gas ionization. The antenna's inner diameter is just larger than the outer diameter of the tube, and thus it is mechanically supported by the tube and is concentric. A RH helical antenna has been selected because it launches RF waves preferentially in one direction. In this case, this has been selected to coincide with the downstream direction.

Surrounding the tube and antenna are two electromagnetic coils wound on aluminum bobbins. These coils provide an axial magnetic field, which contains the plasma and is required to achieve helicon coupling. Two Teflon spacers are positioned within the inner diameter of the coil bobbins, where they then support the quartz tube and antenna.

The distance between the two coils is maintained by 1/4" threaded tie-rods, nuts, and aluminum spacers. These coils, and thus the remainder of the experimental setup, rest on

the aluminum mechanical support structure, the detailed design of which is described in Chapter 5.

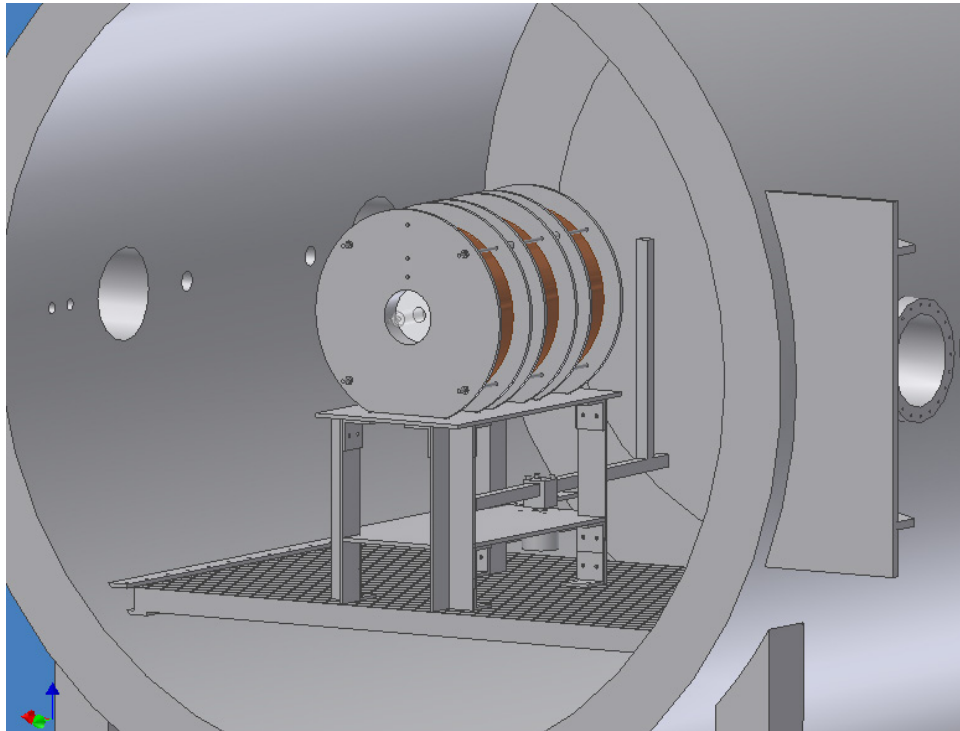


**Figure 3.3** CAD Rendering, to Scale, of the Experimental Setup within the MIT SPL Vacuum Chamber

Since the experiment is contained within the SPL vacuum chamber, it is required to interface with the experiment through the chamber walls. This requires several feed-throughs, including those for gas flow, RF power, magnet power, thermocouples, and other sensors. The matching network, RF power supply, magnet power supply, and computer control are all external to the vacuum tank.

Operator feedback on the status of the experiment is achieved through a number of channels. The experiment can be visually inspected for the presence of a plasma by observations through the chamber 8” viewing ports. Also, forward and reflected power can be observed through the digital display on the front of the RF generator, and this will give additional indication as to the status of the plasma. Thermocouples and other sensors provide operator feedback, and the level of instrumentation will increase with time.

### **3.1.2 Gas Flow System**

A gas flow system was designed and constructed for use with the mHTX.<sup>1</sup> It consists of several components as illustrated in Figure 3.4 below. Gas is supplied from one of a number of bottles, depending upon which particular gas is being run through the

---

1. By Zach LaBry.

experiment. The pressure output of the gas tank is controlled via a standard, manually set regulator. Gas flows from this regulator through a manual cutoff valve and to a mass flow controller, which interfaces with the experiment control computer. The mass flow controller is an Omega FMA6508ST, which is capable of providing 0 – 100 mL / min of nitrogen, and utilizes an onboard correction algorithm to provide correct measurement and control of other gases.

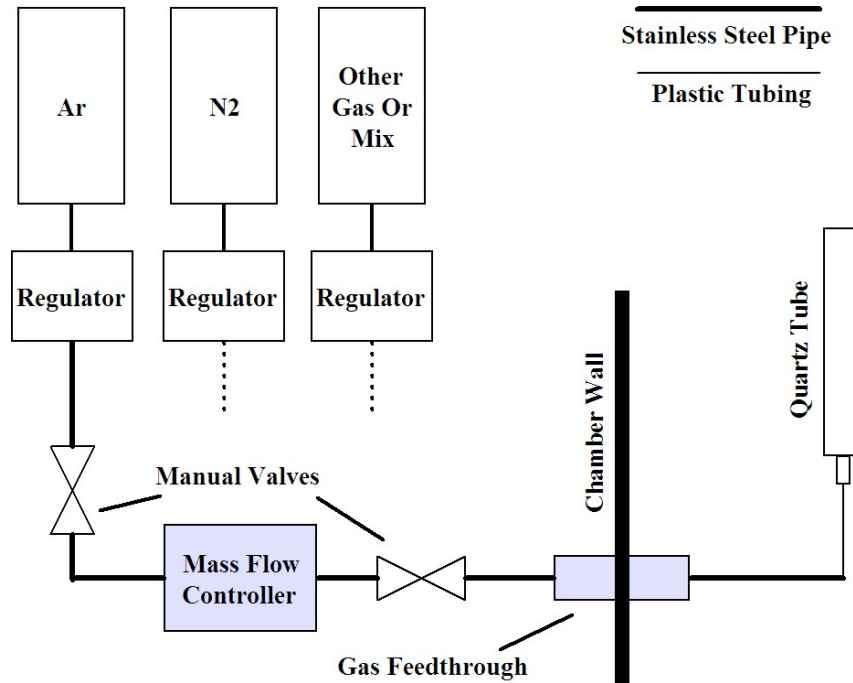


**Figure 3.4** Gas Flow System of the mHTX

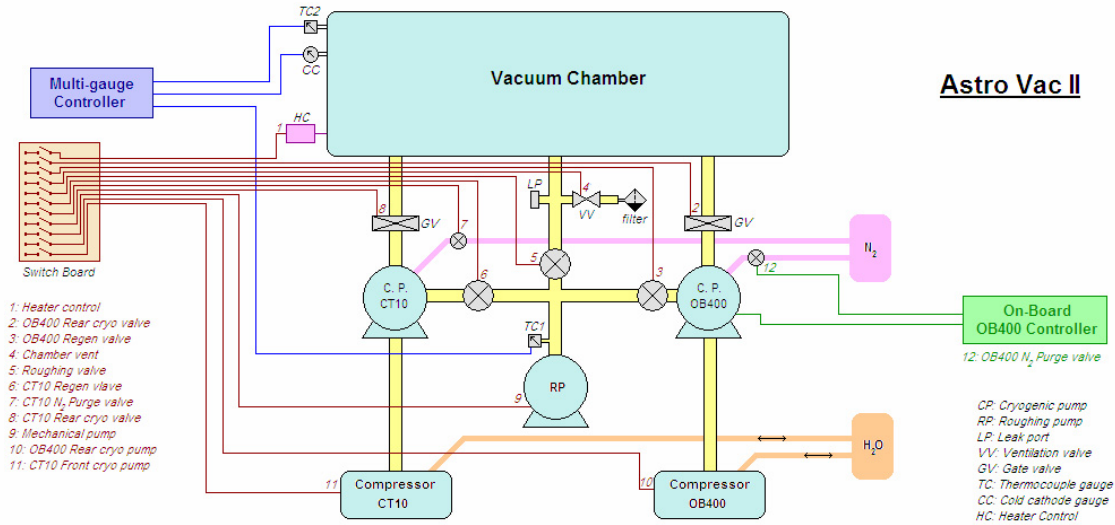
When the mass flow controller is set to an output other than zero, gas flows through another manual cutoff valve. It then flows through a gas feedthrough into the vacuum chamber. All plumbing to this point consists of stainless steel tubing, with stainless steel Swagelok connections. An additional length of stainless steel tubing continues from the gas feedthrough to within one foot of the end of the quartz tube. At this point, a piece of plastic tubing completes the connection to the tube.

The interconnection between the plastic tubing and the quartz tube takes the form of a stainless steel Swagelok connector. It is important to note that this metallic connector is electrically floating. Thus it does not present itself as a conduction path for any plasma which may propagate upstream to this interconnection.

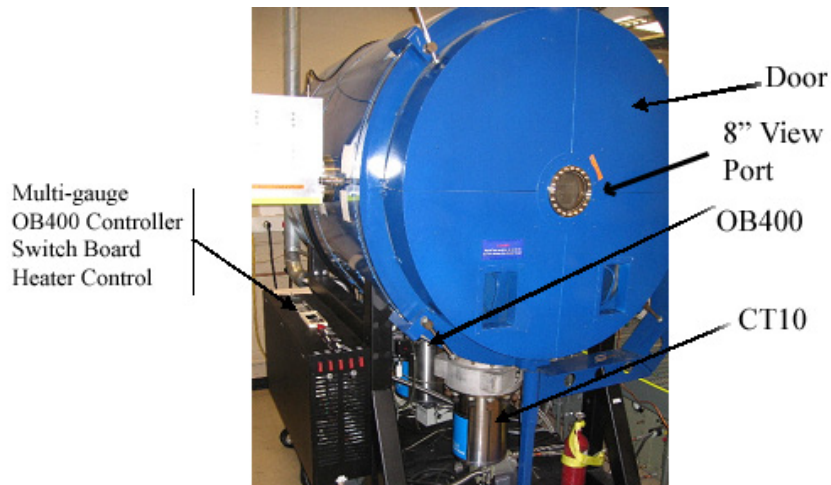
Gas that flows through the system ultimately arrives within the body of the vacuum chamber. There it remains until acted on by the vacuum system. Early propellants that were used in the experiment include nitrogen and argon. These will be followed by hydrogen and other gas mixtures at a later date.

### 3.1.3 Vacuum System

An existing ASTROVAC, vacuum chamber and system available in the MIT Space Propulsion Laboratory were utilized for this experiment.<sup>1</sup> A block diagram of the system is presented in Figure 3.5 below.



The system contains a 1.6m by 1.5m cylindrical vacuum chamber. It is evacuated by two Cryo-Torr 10 cryopumps manufactured by CTI-Cryogenics, each having a pumping capacity of approximately 7500 L/s of Xe. The system is bakeable with included heaters and controller, allowing for removal of surface contaminants. The system is capable of pumping all gases except helium.



1. The system was designed by Professor Manuel Martinez-Sanchez and MIT Research Scientist Paulo Lozano, and installed by Varian Inc.



### 3.1.4 Magnetic Field Generating System

An axial magnetic field is required for two essential purposes, plasma containment and wave coupling. For the first purpose, plasma containment, the parameters of the magnetic field are selected such that the ionized gas will, to a large extent, be prevented from impinging on the walls of the tube. This is made possible due to ion cyclotron motion where ions oscillate around the applied magnetic field lines. The required magnetic field to achieve this effect is calculated in Section 3.2.3 below.

The axial magnetic field is also essential to couple energy from the antenna to the plasma. Plasmas created without the addition of this field are known as Inductively Coupled Plasmas (ICP). In order to achieve the desired helicon discharge, the axial magnetic field is required, resulting in the launch of helicon waves into the plasma. An in depth investigation into this phenomenon is provided by Pucci [Pucci, 2004].

Electromagnetic coils were designed and constructed for use with the experiment.<sup>1</sup> They consist of a square cross section conductor, wound in an overlapping pattern onto bobbins. The bobbins were manufactured by welding cut aluminum plates and tube sections together. The wire is No. 10 AWG, and is coated with an insulative lacquer rated to 200C. Each coil contains 34 overlapping layers, with approximately 960 turns.

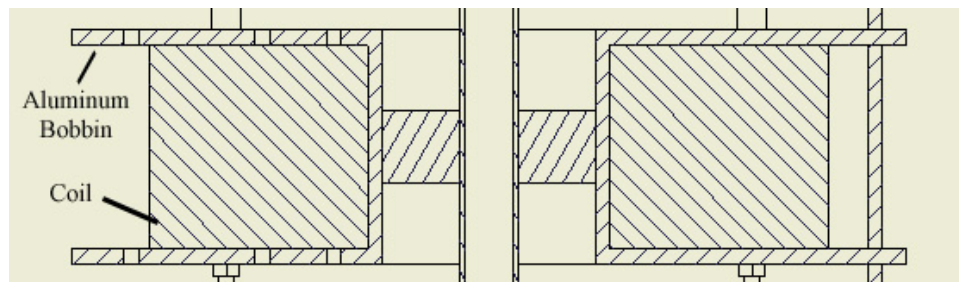


**Figure 3.7** Cross Section of Electromagnetic Coil and Bobbin

These coils have been designed as Helmholtz pairs, meaning that the distance between each coil and the next is fixed equal to the inner radius of the coil, in this case 5cm. Helmholtz pairs were used because they produce a uniform axial magnetic field with few or no perturbations.

Each coil is connected to an independent DC power supply. These supplies are located outside the vacuum chamber, with the connection being made through a suitably rated electrical vacuum feedthrough. This setup is illustrated in Figure 3.8 below. The coils produce a peak axial magnetic field of approximately 2,400 Gauss, which occurs at a coil current of 34A. The correlation between coil current and magnetic field intensity is linear, and is equal to  $\sim 73$  gauss per amp.

<sup>1</sup>. By Justin Pucci and Nareg Sinenian.



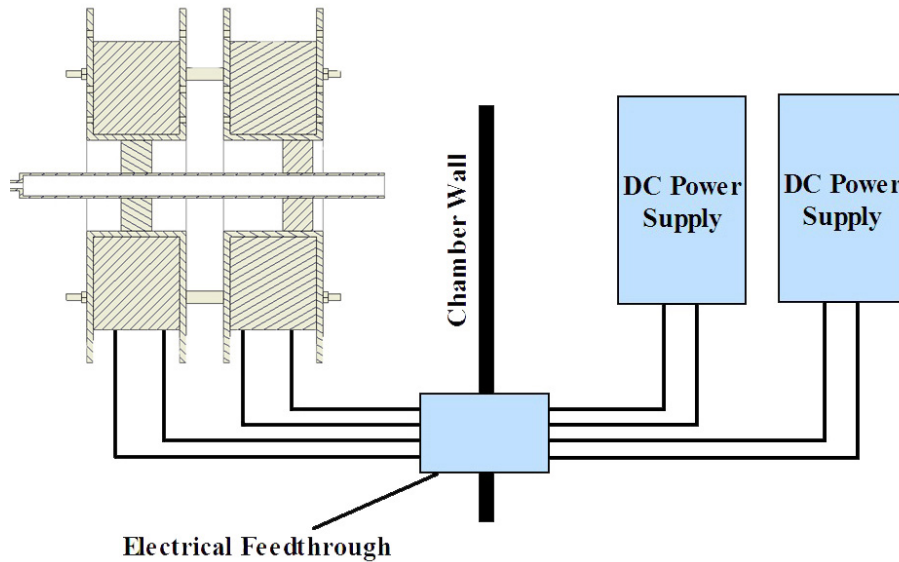


**Figure 3.8** Magnetic Field Generating System Schematic Diagram

During the course of experiment operation, the electromagnets increase in temperature due to ohmic heating. Heat which builds up in the coils is dissipated through radiation and through conduction via the mechanical support structure, by which it is further conducted to the chamber wall. The coils have sufficient thermal mass such that the experiment can operate for several minutes continuously without reaching the 200C operating temperature limit of the coil lacquer insulation. This temperature increase is monitored by use of T-type thermocouples which were incorporated into the coils during their construction. They are located between the 1st and 2nd and between the 16<sup>th</sup> and 17<sup>th</sup> conductor layers. Future coil designs may include a water cooling system to allow for operation of the magnets, and therefore the experiment, for longer durations.

In order to provide experimental flexibility, the mechanical support structure has been designed to accommodate a third electromagnetic coil. Addition of this coil may be desirable in the future as it will allow for further manipulation of the magnetic field profile. The structure can support a coil identical to the first two which, if appropriately spaced and supplied with the same current, would form a Helmholtz pair with the adjacent coil. This would further extend the uniform, axial magnetic field. The addition of this coil, and adjustment of its current relative to the current flowing through the other coils would also allow for magnetic nozzle investigations.

### 3.1.5 Control & Sensor Systems

Control and monitoring of the experiment is effected through use of a central control computer. This computer is an IBM PC, running Windows XP and Labview version 7.1. It is interfaced with a National Instruments PCI-6071E, 12-bit data acquisition system, having a 1 Megasample /sec sampling rate. A Labview program has been developed<sup>1</sup> which allows operation of the experiment and monitoring of various sensors.

<sup>1</sup>. By Nareg Sinenian

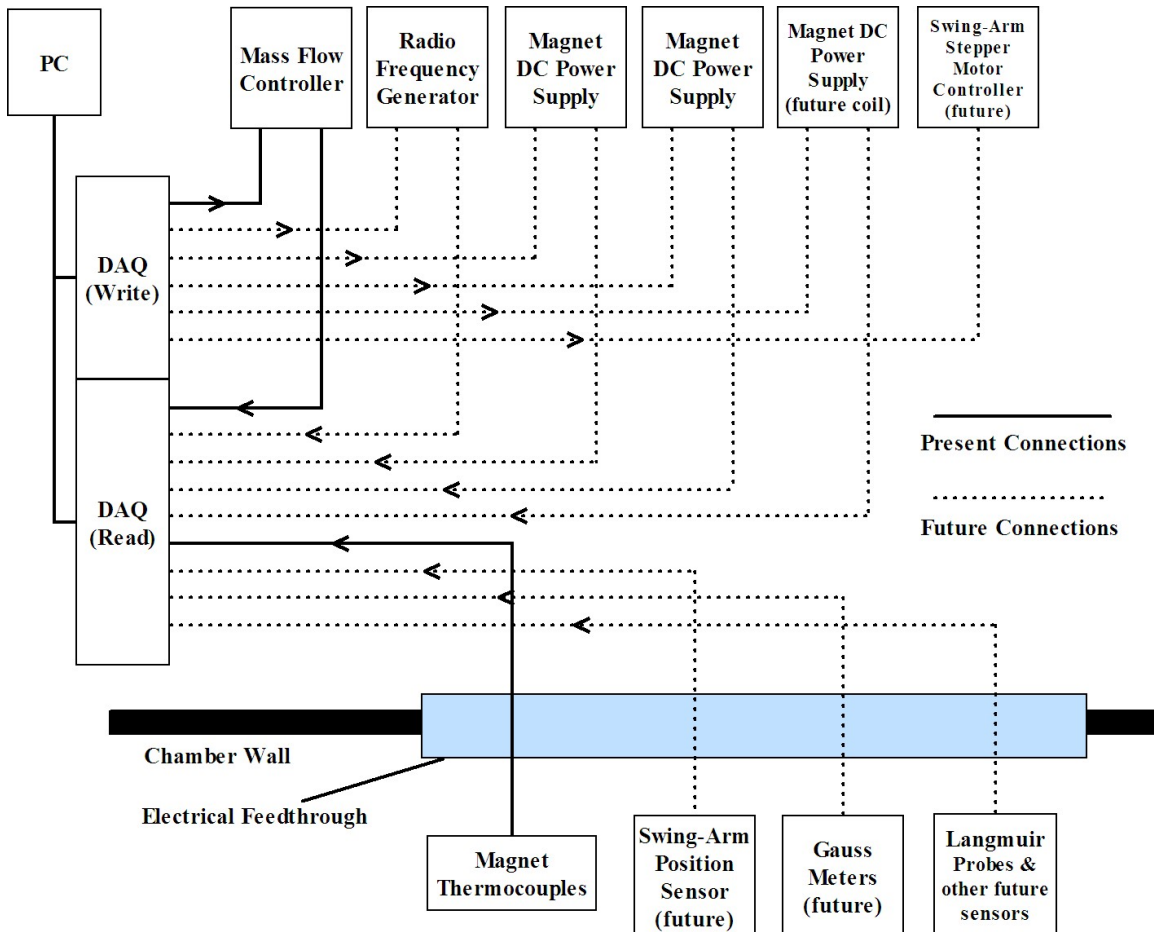


**Figure 3.9** Control & Sensor Systems of the mHTX@MIT

The data acquisition system (DAQ) is presently connected to the mass flow controller. A flow set point is entered via the Labview controls, and a measurement of actual flow rate is shown on the display. In addition, the T-type thermocouples, which are built into the two electromagnetic coils, are also presently connected to the DAQ. Temperatures for each thermocouple are visible on the Labview display.

Much work remains to be accomplished regarding centralized data acquisition and system control. Presently, the radio frequency generator is operated via front panel controls, which allows, among other options, the ability to set desired RF power level and displays forward and reflected power. The electromagnet DC power supplies are also controlled and monitored via front panel controls. The control and monitoring of these systems will be automated in the near term.

The addition of a number of systems will take place in the near future, but are not in the scope of the present investigation. The mechanical support structure has been designed to allow incorporation of a mechanical swing arm, which will allow for the accurate positioning of sensor systems throughout the plume region. This swing arm, when added, will most likely utilize a stepper motor for precise arm location, and this motor will require the use of a stepper motor controller. This controller will be interfaced with the

DAQ system. Also, a swing-arm position sensor may be required, and will also be interfaced with the DAQ. Other systems which will be added at a later date include a third electromagnet DC power supply (which would correspond to the addition of a third coil to the experiment), gaussmeters for the real-time measurement of magnetic field strength, and various plasma diagnostics including Langmuir probes. These systems will be incorporated into the central control and monitoring computer system as they are implemented.

Visual measurements played an important role in the troubleshooting of the experimental setup. Two 8" viewing ports, indicated in Figure 3.10 below, were used to observe the emissions of the discharge in the visible spectrum. Interpretation of this discharge provided valuable feedback regarding the functionality of the experiment, and the plasma mode, as is discussed in Section 7.2. Additionally, spectroscopy data were collected<sup>1</sup> utilizing a fiber-optic pickup which was mounted on the chamber side viewing port. This data will be published at a future date.

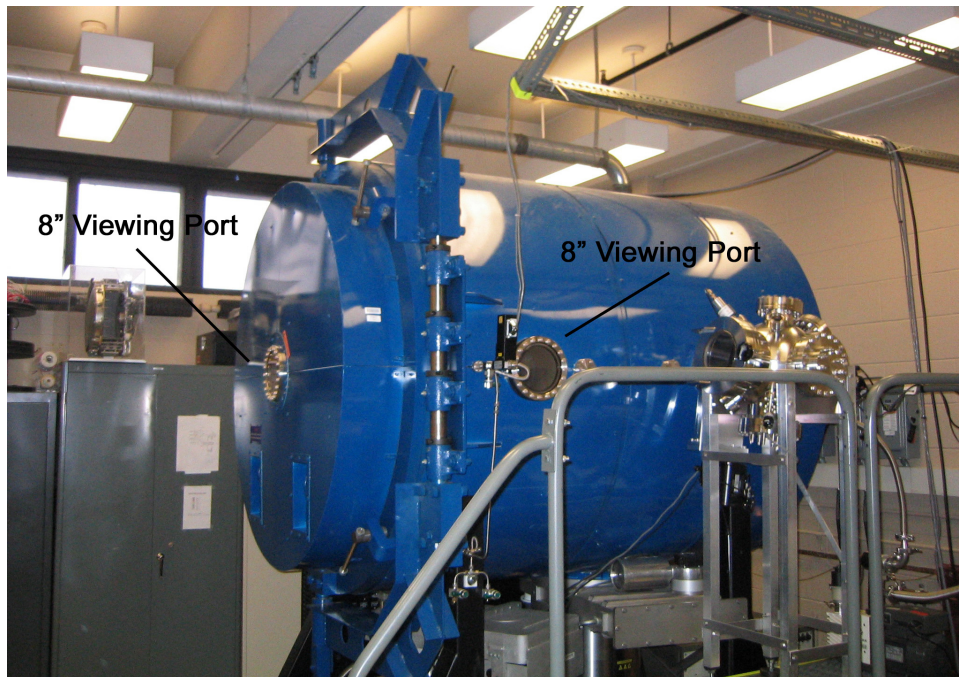


**Figure 3.10** SPL Vacuum Chamber with Viewing Ports Indicated

## 3.2 Experiment Sizing

It was necessary to size each of the subsystems identified in Section 3.1 in order to achieve an operational experiment. Each of these systems was sized according to various constraints, in an iterative process. Sizing criteria included, but was not limited to, desired thruster characteristics, requirements for a helicon discharge, limitations of available hardware, and safety considerations.

---

1. Data collected by Murat Celik.

### 3.2.1 1<sup>st</sup> Order Thrust Calculations<sup>1</sup>

In order to estimate the thrust produced by the proposed device, it will be required to make a number of assumptions. First, we assume, for calculation purposes, that pure hydrogen is being utilized. Gas flow into the system will be assumed constant at a flow rate of ( $\dot{V}_0$ ).

#### Flow Rate Calculations

Radius of Tube (R) [cm]

Length of Tube (L) [cm]

Volumetric Flow Rate of H<sub>2</sub> Gas into Cylinder ( $\dot{V}_0$ ) [sccm]

- sccm = Standard Cubic Centimeter Per Minute =  $\left[ \frac{cm^3}{min} \right]$  at 1 atm.

Volume of 1 mole of gas at 1atm = 22.4 L

$$22.4 \left[ \frac{L}{mole} \right] \times \frac{1000}{1} \left[ \frac{cm^3}{L} \right] = 22,400 \left[ \frac{cm^3}{mole} \right]$$

$$(\dot{V}_0) \left[ \frac{cm^3}{min} \right] \times \frac{1}{22400} \left[ \frac{mole}{cm^3} \right] = \frac{\dot{V}_0}{22400} \left[ \frac{mole}{min} \right]$$

$$\frac{\dot{V}_0}{22400} \left[ \frac{mole}{min} \right] \times N_A \left[ \frac{molecules}{mole} \right] \times \frac{1}{60} \left[ \frac{min}{sec} \right] = \frac{N_A}{(22400)(60)} \dot{V}_0 \left[ \frac{molecules}{sec} \right]$$

**Incoming Molecular flow rate per second ( $\dot{N}_{H_2}$ ) =**

$$4.48 \times 10^{17} \dot{V}_0 \left[ \frac{molecules}{sec} \right] = 4.48 \times 10^{18} \left[ \frac{molecules}{sec} \right] \text{ into the tube.}$$

**Atomic flow rate per second ( $\dot{N}_H$ ) =**

$$4.48 \times 10^{17} \dot{V}_0 \left[ \frac{molecules}{sec} \right] \times K \left[ \frac{atoms}{molecule} \right] = 4.48 \times 10^{17} \dot{V}_0 K \left[ \frac{atoms}{sec} \right]$$

For hydrogen (H<sub>2</sub>), K=2. Thus:

$$8.96 \times 10^{17} \dot{V}_0 \left[ \frac{atoms}{sec} \right] = 8.96 \times 10^{18} \left[ \frac{atoms}{sec} \right]$$

1. All calculations presented in this thesis are the work of this author, with exceptions where noted.

It can be assumed that the atomic flow rate remains constant throughout the tube due to conservation of mass. However, as the gas flows through the tube, it is dissociated and ionized by the energy deposited by the helicon antenna. A treatment of the flow conditions under the circumstances of changing molecules / ion composition mid-stream would require analysis using partial pressure of each species. For simplicity in the first cut calculations, this effect will be neglected and we will assume the gas in the tube is entirely comprised of one species, namely dissociated H atoms.

The mass flow rate through the tube can be calculated given the above atomic flow rate and the mass per atom:

$$\dot{m}_{H@1} = \dot{m}_{H@2} = \text{const} = (1.6727 \times 10^{-27}) \left[ \frac{\text{kg}}{\text{atom}} \right] \times (8.96 \times 10^{18}) \left[ \frac{\text{atoms}}{\text{sec}} \right] = 1.499 \times 10^{-8} \left[ \frac{\text{kg}}{\text{s}} \right]$$

### Thrust Force – Initial Estimate

An initial estimate of the thrust generated by the device can be made. This calculation is based upon the flow rate of atoms through the device, the mass of those atoms, and their average outward velocity. In the case of hydrogen gas, it is assumed that the ionization process results in a stream of  $H^+$  ions emitted from the device. These are the primary contributors to the thrust, as the electrons are less massive by four orders of magnitude. Literature review yields experimental data indicating kinetic energy magnitudes of the departing ions on the order of  $2T_e$ .

$$\text{Kinetic Energy } E \sim 2T_e = 2(10[eV]) = 20[eV] \times 1.6 \times 10^{-19} \left[ \frac{J}{eV} \right] = 3.2 \times 10^{-18} [J]$$

$$E = \frac{mv^2}{2}$$

$$v = \sqrt{\frac{2E}{m}} \left[ \sqrt{\frac{J}{K}} = \sqrt{\frac{\text{kgm}^2}{\text{s}^2 \text{kg}}} = \frac{m}{s} \right] = \sqrt{\frac{2(3.2 \times 10^{-18})}{1.67 \times 10^{-27}}} = 6.191 \times 10^4 \left[ \frac{m}{\text{sec}} \right]$$

Thrust Force

$$= \dot{N}_{H^+ (\text{at-outlet})} \left[ \frac{\text{ions}}{\text{sec}} \right] m_{H^+} \left[ \frac{\text{kg}}{\text{ion}} \right] v \left[ \frac{m}{\text{sec}} \right] = \dot{N}_{H^+} m_{H^+} v \left[ \frac{\text{ion kg m}}{\text{sec ion sec}} = \frac{\text{kgm}}{\text{sec}^2} = N \right]$$

Thrust Force

$$= (8.96 \times 10^{18}) \left[ \frac{\text{ions}}{\text{sec}} \right] (1.6726 \times 10^{-27}) \left[ \frac{\text{kg}}{\text{ion}} \right] (6.191 \times 10^4) \left[ \frac{m}{\text{sec}} \right] = 0.928 \times 10^{-3} [N]$$

Thus a flow rate of 10 sccm of hydrogen should yield a thrust of approximately 1mN.

### 3.2.2 Gas Selection and Chamber Pumping Capacity

A necessary decision was the selection of gas to be used as thruster propellant. Traditional electric propulsion systems utilize heavy gases such as xenon or argon. Helicons, however, can efficiently ionize light gases. Hydrogen represents an especially attractive choice, however use of hydrogen in the laboratory requires nontrivial safety considerations to prevent combustion hazards. Early gases which will be utilized in this experiment will be nitrogen and argon, as they are readily available and inexpensive. Later experimentation will involve use of various gases and gas mixtures, including the storable fluids water and ammonia, and may include hydrogen if safety requirements are met.

As the helicon experiment operates, gas flows through the quartz tube and into the vacuum chamber. Simultaneously, the pumping system removes gas from the chamber. If the pressure is allowed to increase beyond a certain point, it will begin to negatively impact the operation of the experiment. In such a case, the experiment cannot be operated in a steady state manner, but rather pulsed operation must be employed. It is desirable to determine if the experiment can be operated in a steady state manner, and if it cannot then we desire the allowable time duration of experiment operation, and consequently the time required to restore the chamber to its original background pressure.

The following assumptions are used in this calculation:

- 1) The worst tolerable chamber pressure is  $10^{-4}$  Torr.
- 2) The initial pressure in the chamber before the experiment begins is  $10^{-5}$  Torr.
- 3) Mass flow rate of hydrogen gas into the chamber through the experiment is:

$$\dot{m}_in = 1.499 \times 10^{-8} \left[ \frac{kg}{s} \right]$$

- 4) SPL Vacuum Chamber Cyropump Limitations
  - a. Pump 1: 12,000 L/sec of hydrogen
  - b. Pump 2: 6,000 L/sec of hydrogen

Further details regarding the vacuum system utilized is described in Section 3.1.3 above.

Pumping Speed:

$$1800 \left[ \frac{L}{satm} \right] \times \left[ \frac{1atm}{760torr} \right] \times 10^{-4} [torr] = 2.3 \times 10^{-4} \left[ \frac{L}{s} \right]$$

Experiment Gas Input Speed:

$$10 [sccm] = 10 \left[ \frac{cm^3}{min atm} \right] \times \left[ \frac{L}{1000cm^3} \right] \times \left[ \frac{min}{60s} \right] \times \left[ \frac{1atm}{760torr} \right] \times 10^{-4} [torr] = 2.19 \times 10^{-11} \left[ \frac{L}{s} \right]$$

Hence the pumping system should be capable of maintaining a constant pressure in the vacuum chamber for an input flow rate of 10 sccm hydrogen.

### 3.2.3 Plasma Containment

We desire to contain the plasma within the tube, such that it does not impinge on the tube inner surface. Such interaction is undesirable as surface collisions will involve the transfer of energy from the gas to the colder walls, resulting in recombination, loss of plasma and heating of the wall. A known effect in plasma physics is that plasma motion across magnetic field lines is limited. Thus some measure of containment can be accomplished by applying an axial magnetic field of strength (B). Electrons and ions traveling along these magnetic field lines will undergo cyclotron motion around these vectors. To prevent plasma from encountering the tube inner surface in the course of this motion, it is necessary that their respective gyro radii, also known as Larmor Radii ( $r_{Le}$ ,  $r_{Li}$ ) be less than the tube radius. We seek therefore the necessary strength of the axial magnetic field for this to be the case.

We define ( $T_e$ ) and ( $T_i$ ) respectively as the temperature of the electrons and the ions. Typical experimental values for  $T_e$  and  $T_i$  have been obtained from the literature. Charles and Boswell have obtained  $T_e \sim 8\text{eV}$  in the Chi-Kung helicon apparatus [Charles, 2004B]. Other experimental results have yielded  $T_i \sim 1\text{eV}$ . For purposes of initial rough analysis it is assumed that  $T_e = 10\text{eV}$  and  $T_i = 1\text{eV}$ .

As stated in Section 3.1.4, a set of electromagnetic coils have been assembled, which produce an axial magnetic field of up to  $0.24\text{T} = 2400\text{G}$ . The inner diameter of these magnets is 10cm. Within this 10 cm magnet inner diameter, it is necessary to locate both the quartz tube as well as the surrounding helicon antenna. A quartz tube inner diameter of 2 cm has been selected, i.e., a tube radius of 1 cm. The assumption is made that the gyro radii must be  $\leq 1/10^{\text{th}}$  of the tube radius. Given this condition and the radius of the tube,  $r_L$  must  $\leq 0.10$  [cm].

We assume that all ions produced in the plasma are of the form  $\text{H}^+$ , hence the charge state of the ions ( $Z$ ) here equals 1. The mass of a proton is ( $m_p$ ). We define  $\mu_m = m_i / m_p$ , and therefore the mass of an ion ( $m_i$ ) =  $\mu_m m_p$ . For the case of  $\text{H}^+$  ions,  $\mu_m = 1$  and ( $m_i$ ) =  $m_p$ .

#### Electron Larmor Radius ( $r_{Le}$ )

$$r_{Le} = 2.38T_e^{1/2}B^{-1}, \text{ (} T_e \text{ in eV, } B \text{ in Gauss)} \quad [\text{NRL,2004}]$$

For  $r_{Le}$  set equal to 0.10cm:

$$B \geq \frac{2.38T_e^{1/2}}{r_{Le}} = \frac{(2.38)(10)^{1/2}}{0.10} = 75\text{G}$$

#### Ion Larmor Radius ( $r_{Li}$ )

$$r_{Li} = 1.02 \times 10^2 \mu^{1/2} Z^{-1} T_i^{1/2} B^{-1}, \text{ (} T_e \text{ in eV, } B \text{ in Gauss)} \quad [\text{NRL,2004}]$$

For  $r_{Li}$  set equal to 0.10cm:

$$B = \frac{1.02 \times 10^2 \mu^{1/2} T_i^{1/2}}{Z r_{Li}} \geq 1020\text{G}$$

We see that the more stringent requirement on B is set by the ions. They require a higher B field to limit their Larmor Radius than do the electrons. This also implies that  $r_{Li}$  is always greater than  $r_{Le}$  for a given applied magnetic field. The required magnetic field strength of 1020G = 0.102T should be obtainable using the present electromagnets.

To verify the validity of these calculations, we can arrive at the definition for the gyro radius by first determining some other useful parameters using this value (0.102T) for B. First we calculate the cyclotron frequencies, which are the frequencies at which ions and electrons respectively circle the magnetic field lines. Here the value  $|q|$  is equal to  $|e|$ , the elementary charge. Also the mass of an electron is ( $m_e$ ).

### Electron Cyclotron Frequency ( $\omega_{ce}$ )

$$\omega_{ce} = \frac{|q|B}{m_e} \left[ \frac{CT}{kg} = As \frac{kg}{s^2 A kg} \right] = 1.76 \times 10^{11} B \left[ \frac{rad}{sec} \right] = 1.795 \times 10^{10} \left[ \frac{rad}{sec} \right]$$

$$f_{ce} = \omega_{ce} \left[ \frac{rad}{sec} \right] \times \frac{1}{2\pi} \left[ \frac{cycle}{rad} \right] = \frac{\omega_{ce}}{2\pi} \left[ \frac{cycle}{sec} = Hz \right] = 2.801 \times 10^{10} B [Hz] = 2.86 [GHz]$$

### Ion Cyclotron Frequency ( $\omega_{ci}$ )

$$\omega_{ci} = \frac{Z|q|B}{m_i} \left[ \frac{rad}{sec} \right] = 9.57 \times 10^7 \mu_m^{-1} B \left[ \frac{rad}{sec} \right] = 9.57 \times 10^7 B \left[ \frac{rad}{sec} \right] = 9.76 \times 10^6 \left[ \frac{rad}{sec} \right]$$

$$f_{ci} = \frac{\omega_{ci}}{2\pi} [Hz] = 1.523 \times 10^7 B [Hz] = 1.55 [MHz]$$

Next we can calculate the electron and ion thermal velocities. Here (k) is the Boltzmann constant.

Boltzmann Constant (k) =

$$1.3807 \times 10^{-23} \left[ \frac{J}{deg K} = \frac{kgm^2}{s^2 deg K} = \frac{(100)(100)kgcm^2}{s^2 deg K} \right] = 1.3807 \times 10^{-19} \left[ \frac{kgcm^2}{s^2 deg K} \right]$$

$$T_e = 10 [eV] = 10 [eV] \times (11,605) \left[ \frac{deg K}{eV} \right] = 1.16 \times 10^5 [deg K]$$

$$T_i = 1 [eV] = 1 [eV] \times (11,605) \left[ \frac{deg K}{eV} \right] = 1.16 \times 10^4 [deg K]$$

### Electron Thermal Velocity ( $v_{Te}$ )

$$v_{Te} = \sqrt{\frac{kT_e}{m_e}} \left[ \sqrt{\frac{kgcm^2}{s^2 deg K} deg K \frac{1}{kg}} \right] = 3.89 \times 10^5 T_e^{1/2} \left[ \frac{cm}{sec} \right] = 1.32 \times 10^8 \left[ \frac{cm}{sec} \right]$$



**Ion Thermal Velocity ( $v_{Ti}$ )**

$$v_{Ti} = \sqrt{\frac{kT_i}{m_i}} \left[ \sqrt{\frac{kgcm^2}{s^2 \text{ deg } K} \text{ deg } K \frac{1}{kg}} \right] = 9085 \mu^{-1/2} T_i^{1/2} \left[ \frac{cm}{sec} \right] = 9.78 \times 10^5 \left[ \frac{cm}{sec} \right]$$

Thus we can see that the more massive ions travel at less than 1/100<sup>th</sup> of the speed of the electrons. We can now verify the 0.10cm ion gyro radii, and find the electron gyro radius, for an applied axial magnetic field of 0.102T.

**Electron Larmor Radius ( $r_{Le}$ )**

$$r_{Le} = \frac{v_{Te}}{\omega_{ce}} [cm] = \frac{(1.32 \times 10^8)}{(1.795 \times 10^{10})} = 0.007 [cm]$$

**Ion Larmor Radius ( $r_{Li}$ )**

$$r_{Li} = \frac{v_{Ti}}{\omega_{ci}} [cm] = \frac{(9.78 \times 10^5)}{(9.76 \times 10^6)} = 0.10 [cm]$$

So for applied magnetic fields above 1020G, the electron and ion Larmor radii remain within the acceptable limit.



# Chapter 4

## PROPELLANT FLOW MODELING

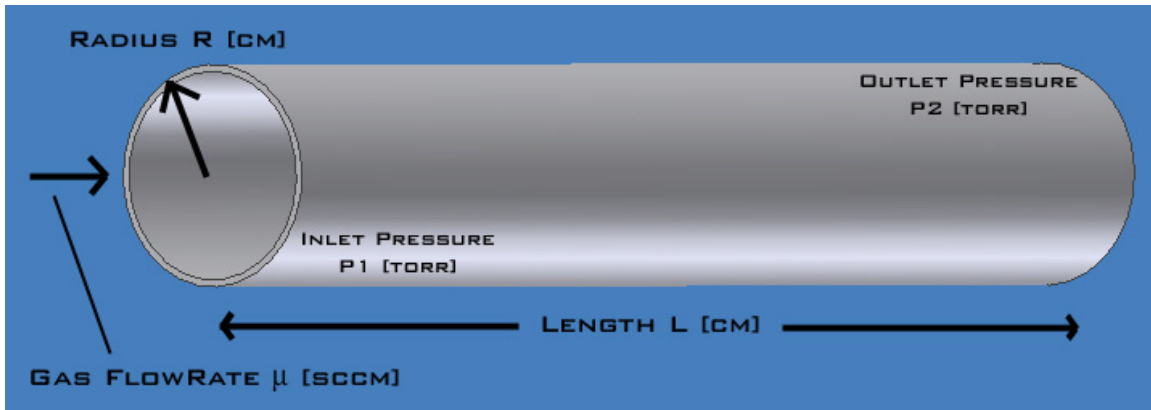


**Figure 4.1** Quartz Tube Component of the Mini-Helicon Thruster Experiment

Within the experimental setup, gas flows through a quartz tube, illustrated in Figure 4.1 above, where it is acted upon by the helicon antenna. The flow then passes out of the tube and into the vacuum chamber. In order to gain greater understanding of this propellant flow, an analysis of it has been undertaken by this author. The result of such analysis is a characterization of gas flow parameters at each axial position along the length of the tube. Analysis is undertaken in a self consistent manner, by which certain assumptions are selected, and the validity of those assumptions is then tested. Low Mach number flow theory is applied to effect this analysis, and some parametric analysis is undertaken.

### Low Mach Number Flow Assumption

Approximations which do not account for inertia effects are known to be valid for Mach numbers less than  $1/3$ . Despite imposing a Mach number of 1 at the tube outlet, we will still make use of the low Mach number approximations, assuming that the tube region with Mach number greater than  $1/3$  is restricted to very near the tube exit. The validity of this assumption will be tested.

### **4.1 Viscous Flow**

Initially the following assumptions will be made:

- 1) The gas flow remains below Mach number =  $1/3$  for nearly the entire tube length.
- 2) The flow is viscous (or laminar).
- 3) The flow is fully developed
- 4) There is no turbulent motion
- 5) The flow velocity at the tube walls is zero (i.e., no slip condition).

By viscous or laminar flow, we refer to the development of a flow velocity profile whose magnitude varies parabolically with radius, caused by frictional or viscous effects of the gas. As the gas flows down the tube, frictional forces at the walls slow the layer of gas flowing nearby. This retarded layer then exerts frictional forces on the next inner layer of gas and so on, thus creating a parabolic velocity profile, as illustrated in Figure 4.2. The flow, which has velocities uniform across the tube radius at the inlet, gradually develops the parabolic velocity profile which is said to be “fully developed” when the profile remains unchanging as it propagates down the tube.



**Figure 4.2** Viscous Flow – Parabolic Velocity Profile Development

For a section of tube down which a gas is flowing as the result of a pressure difference at its two ends, Dushman presents the following equation for viscous flow, which is called the Poiseuille equation:

$$Q = \frac{\pi R^4}{8\eta L} P_a (P_1 - P_2) \quad [\text{Dushman, 1962}]$$

Where:

Q = the volumetric flow rate times pressure at the tube outlet:

$$Q = P\dot{V} = kT\dot{N} \quad [\text{Dushman, 1962}]$$

R = tube radius

P<sub>1</sub> = inlet pressure

P<sub>2</sub> = outlet pressure

P<sub>a</sub> = the arithmetic mean of P<sub>1</sub> and P<sub>2</sub> which equals  $\frac{P_1 + P_2}{2}$

η = gas coefficient of viscosity

L = length of tube

$$kT\dot{N}_{\text{gas-particles}} = \frac{\pi R^4}{8\eta L} \left( \frac{P_1 + P_2}{2} \right) (P_1 - P_2)$$

Given the gas-particle flow rate calculated above (based on 10 sccm) and the other parameters, one can use this formula to calculate the pressure drop in the tube. We assume a constant flow-rate of gas and a constant temperature.

$$\Delta P = \sqrt{\frac{16\eta L k T \dot{N}}{\pi R^4}}$$

Let us determine the other parameters in the equation:

The gas is assumed to be isothermal as it travels through the tube, and so its temperature remains constant at the inlet temperature. This inlet temperature is assumed room temperature  $T \sim 300\text{K}$ .

The coefficient of viscosity ( $\eta$ ) is a characteristic of the gas which is somewhat dependent on temperature and is generally independent of pressure. The viscosity of hydrogen at 300K is  $8.89 \times 10^{-6} \text{ [kg / ms]}$  [LMNO Eng, 2003].

$$\dot{N}_{@outlet} = 8.96 \times 10^{18} \left[ \frac{\text{particles}}{\text{sec}} \right] \text{ (from above)}$$

The tube radius chosen for these calculations is 1.5cm.

The length of tube has not yet been selected. A tube length is desirable such that the flow is fully developed, so that the simplified calculations above will remain valid. One must select a length, however, which is not unwieldy or unpractical from an experimental standpoint. Dushman quotes Langhaar in that the flow will be fully developed in a distance  $l_e$ , from the entrance of the tube, with  $l_e$  given by:

$$l_e = 0.227 a \text{ Re} \quad \text{[Dushman, 1962]}$$

Where:

$a$  = the radius of the tube

$\text{Re}$  = the Reynolds number of the flow

### Reynolds Number

We must first calculate the Reynolds number, which is a dimensionless parameter of the flow. Dushman defines the Reynolds number ( $\text{Re}$ ) as:

$$\text{Re} = \frac{a \rho U_{fa}}{\eta} \quad \text{[Dushman, 1962]}$$

Where:

$a$  = tube radius

$\rho$  = the gas density

$U_{fa}$  = the average velocity

$\eta$  = gas viscosity

The average flow velocity across a plane in the tube can be found as:

$$U_{fa} = \frac{Q}{\pi a^2 P} = \frac{P\dot{V}}{\pi a^2 P} = \frac{m_H k T \dot{N}_H}{\pi a^2 \rho k T} = \frac{m_H \dot{N}_H}{\pi a^2 \rho} \quad [\text{Dushman, 1962}]$$

Here Charles' law (or Gay-Lussac's law) has been used, which states:

$$\frac{P}{\rho} = \frac{k}{m} T, \quad \frac{1}{P} = \frac{m}{\rho k T} \quad [\text{Dushman, 1962}]$$

So we can redefine the Reynolds number as:

$$\text{Re} = \frac{m_H \dot{N}_H}{\pi a^2 \rho} \frac{a \rho}{\eta} = \frac{m_H \dot{N}_H}{\pi \eta a}$$

$$\text{Re} = \frac{m_H \dot{N}_H}{\pi \eta a} = \frac{(1.6726 \times 10^{-27}) [\text{kg}] (8.96 \times 10^{18}) [\#/\text{sec}]}{\pi (8.89 \times 10^{-6}) [\text{kg}/\text{ms}] (1.5) [\text{cm}] [m/100\text{cm}]} = 3.578 \times 10^{-2}$$

Dushman prescribes a critical Reynolds number of 1000 for smooth tubes with “well-rounded entrances” [Dushman, 1962]. Since the Reynolds number here is well below this critical value, the flow can be considered purely laminar (as opposed to being turbulent for higher Reynolds numbers).

The length needed for this flow to be fully developed, according to this analysis is:

$$l_e = 0.227 a \text{Re} = (0.227)(1.5\text{cm})(3.578 \times 10^{-2}) = 0.012\text{cm}$$

It should be noted that these calculations underestimate the length for fully developed flow when dealing with very low Reynolds numbers. According to Barber and Emerson, for Reynolds numbers of this magnitude, L/D is approximately 1 [Barber, 2002]. With a tube diameter of 3 cm, the length for fully developed flow is approximately 3 cm.

We therefore set our length to a reasonable value for an experimental setup: L=25cm

Given these parameters one can now calculate the pressure drop through the pipe to sustain a flow rate of 10 sccm.

$$\begin{aligned} \Delta P &= \sqrt{\frac{16\eta L k T \dot{N}_{@outlet}}{\pi R^4}} \\ &= \sqrt{\frac{(16)(8.89 \times 10^{-6}) \left[ \frac{\text{kg}}{\text{ms}} \right] (25) [\text{cm}] 1.3807 \times 10^{-23} \left[ \frac{\text{kgm}^2}{\text{Ks}^2} \right] (300) [\text{K}] (8.96 \times 10^{18}) \left[ \frac{\#}{\text{s}} \right]}{(\pi)(1.5^4) [\text{cm}^4] (1/100) [m/\text{cm}] (1/100) [m/\text{cm}] (1/100) [m/\text{cm}]} } \\ &= 2.88 \left[ \frac{\text{kg}}{\text{ms}^2} = \text{Pa} \right] = (2.88) [\text{Pa}] \left( \frac{1}{101.1\text{k}} \right) \left[ \frac{\text{atm}}{\text{Pa}} \right] (760) \left[ \frac{\text{torr}}{\text{atm}} \right] = 21.6\text{mtorr} \end{aligned}$$

## Mach Number & Pipe Outlet Pressure

$$M = \text{the Mach number of the flow} = \frac{U_{fa}}{c}$$

The Mach number is defined as the ratio of the flow velocity to the velocity of sound in the gas. The average flow velocity across a plane in the tube again is:

$$U_{fa} = \frac{Q}{\pi a^2 P} = \frac{kT\dot{N}_H}{\pi a^2 P} \quad [\text{Dushman, 1962}]$$

The speed of sound in this gas can be found by using:

$$c = \sqrt{\kappa T \frac{R_0}{M_H}} \quad [\text{Olsen, 1990}]$$

Where:

$$\kappa = \text{Adiabatic index for the gas} = \frac{c_p}{c_v} = 1.40 \text{ for H}_2 \quad [\text{Olsen, 1990}]$$

T = gas temperature

$$R_0 = \text{universal gas law constant} = (8.3145) \left[ \frac{J}{Kmol} \right]$$

$$M_H = \text{molar mass of the gas} = (1.00794) \left[ \frac{g}{mol} \right]$$

$$c = \sqrt{(1.40)(300)[K] \frac{(8.3145) \left[ \frac{kgm^2}{s^2 Kmol} \right]}{1.00794 \left[ \frac{g}{mol} \right] \left[ \frac{kg}{1000g} \right]}} = 1861.3 \left[ \frac{m}{s} \right] = 1.86 \times 10^5 \left[ \frac{cm}{s} \right]$$

As the gas flows down the tube, the pressure will steadily drop. As the pressure drops, the average velocity of the gas ( $U_{fa}$ ), which is proportional to  $1/P$ , increases. As a result, the Mach number will increase, until the flow reaches the end of the tube. At this point, one can apply a boundary condition which is that the Mach number at the outlet of the tube should equal approximately 1. Beyond this point, the gas disperses into the low pressure vacuum tank, and additional pressure drop occurs between the outlet pressure and the vacuum tank background pressure. This additional pressure drop forces the Mach number to exceed 1, and the flow will become supersonic as it expands into the vacuum chamber.

$$M = \frac{U_{fa}}{c}, \quad U_{fa} = \frac{kT\dot{N}_H}{\pi a^2 P}$$

Combining equations and solving for P:  $P = \frac{kT\dot{N}_H}{\pi a^2 M c}$

At the outlet,  $M = 1$  so the pressure can be determined as:

$$P_{outlet} = \frac{(1.3807 \times 10^{-23}) \left[ \frac{kgm^2}{Ks^2} \right] (300) [K] (8.96 \times 10^{18}) \left[ \frac{1}{s} \right]}{(\pi)(0.015)^2 [m^2] (1)(1861.3) \left[ \frac{m}{s} \right]} = 0.028 [Pa]$$

$$= (0.028) [Pa] \left( \frac{1}{101.1k} \right) \left[ \frac{atm}{Pa} \right] (760) \left[ \frac{torr}{atm} \right] = 0.21 mtorr$$

Beyond the outlet of the tube, a pressure gradient exists between this outlet pressure, and the vacuum tank background pressure of  $\sim 10^{-5} [torr] = 1.33 \times 10^{-3} Pa$ .

Given the calculated outlet pressure and knowing the  $\Delta P$  in the tube, the inlet pressure can be found as:

$$P_{inlet} = P_{outlet} + \Delta P = (0.028) [Pa] + (2.88) [Pa] = 2.91 [Pa] = 21.81 [mtorr]$$

### Gas Inertia Effects

One of the assumptions made in the course of these calculations was that the Mach number remained below 1/3 and therefore inertia effects could be ignored. Dushman states that the inertial effects of the gas can be neglected if the following criteria is met:

$$\frac{1}{2} M^2 \ll 1 \quad [Dushman, 1962]$$

At the pipe inlet, where the pressure is  $2.908 \left[ \frac{kg}{ms^2} \right]$ :

$$U_{fa} = \frac{(1.3807 \times 10^{-23}) \left[ \frac{kgm^2}{s^2 K} \right] (300) [K] (8.96 \times 10^{18}) \left[ \frac{\#}{sec} \right] \left[ \frac{100cm}{m} \right] \left[ \frac{100cm}{m} \right]}{\pi (1.5^2) [cm^2] (2.908) \left[ \frac{kg}{ms^2} \right]}$$

$$= 18.06 [m/s] = 1805.5 [cm/s]$$

So the Mach number is:

$$M = \frac{U_{fa}}{c} = \frac{1805.5 [cm/s]}{1.86 \times 10^5 [cm/s]} = 0.0097$$



This indicates that the flow is subsonic at the inlet. According to Dushman, who quotes Schlichting, to ignore inertial effects a maximum limit of  $M=1/3$  should be observed [Dushman, 1962]. The present flow is well below this threshold for nearly the entire length of the tube. Only at the very end of the tube (last 2%) does the Mach number exceed  $1/3$ , indicating that inertial corrections must be employed. See Figure 4.3 below.

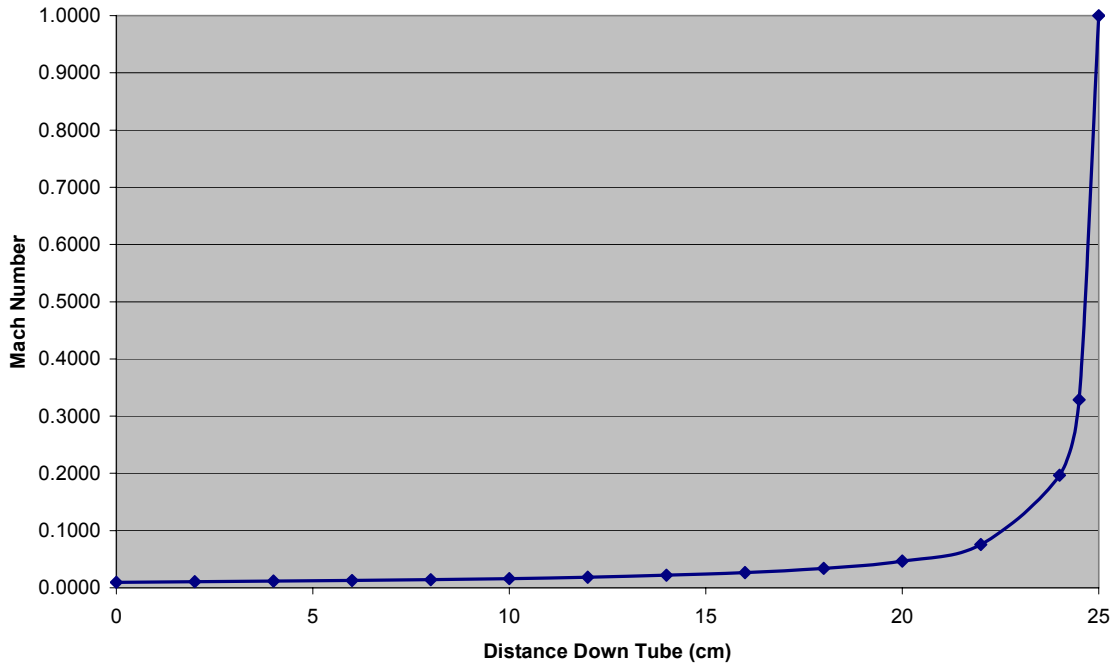


**Figure 4.3** Mach Number vs. Distance Down the Tube

### Gas Density

We can assume that the pressure varies linearly with distance down the tube, from a maximum value at the inlet to a minimum value at the outlet. The relationship between gas pressure and distance down the tube is:

$$P(z) = \left( \frac{0.028 - 2.908}{L} z + 2.908 \right) [Pa] = \left( \frac{0.028 - 2.908}{25} z + 2.908 \right) [Pa], \quad z \text{ in cm}$$

$$= (-0.1152z + 2.908) [Pa]$$

The gas density can be found as:

$$\rho = \frac{m_H P}{kT} = \frac{(1.6726 \times 10^{-27}) [kg]}{(1.3807 \times 10^{-23}) \left[ \frac{kgm^2}{s^2K} \right] (300) [K]} (-0.1152z + 2.908) \left[ \frac{kg}{ms^2} \right]$$

$$= (4.038 \times 10^{-7}) (-0.1152z + 2.908) \left[ \frac{kg}{m^3} \right]$$

This formula yields the density at the tube inlet as:

$$\rho = (4.038 \times 10^{-7})(-0.1152(0) + 2.908) = 1.17 \times 10^{-6} \left[ \frac{kg}{m^3} \right] = 1.17 \times 10^{-12} \left[ \frac{kg}{cm^3} \right]$$

The number density can be calculated as:

$$\begin{aligned} n &= \frac{\rho N_A}{M_H} = \frac{(6.022 \times 10^{23}) \left[ \frac{\#}{mole} \right]}{(1.00794) \left[ \frac{g}{mole} \right] \left( \frac{1}{1000} \right) \left[ \frac{kg}{g} \right]} \left( (4.038 \times 10^{-7})(-0.1152z + 2.908) \right) \left[ \frac{kg}{m^3} \right] \\ &= 2.41 \times 10^{20} (-0.1152z + 2.908) \left[ m^{-3} \right] \end{aligned}$$

At the tube inlet, the number density is:

$$n = 2.41 \times 10^{20} (-0.1152(0) + 2.908) \left[ m^{-3} \right] = 7.008 \times 10^{20} \left[ m^{-3} \right] = 7.008 \times 10^{14} \left[ cm^{-3} \right]$$

As the flow progresses through the pipe the following occurs:

- The pressure decreases from the inlet pressure to the outlet pressure
- The average velocity in the cross section increases.
- The density decreases.
- The Reynolds number remains constant (density decreases at same rate the velocity increases)

Also since we have assumed purely laminar flow, then we can assume that there is no radial velocity component. As the flow progresses, the gas layers formed tend to not mix with each other, and thus the velocity remains completely in the axial direction. This implies that there is no radial density gradient, because if such a gradient existed, then it would drive a radial velocity.

### Mean Free Path

It is assumed that molecules do not travel in straight-line paths down the length of the tube, but rather interact with other molecules in a large number of collisions. These collisions are inelastic in nature and result in a much reduced propagation velocity of gas down the tube, as opposed to a particle traveling in the straight-line path from the inlet to the outlet. The *mean free path* ( $L_m$ ) can be defined as the average distance a molecule travels before undergoing a collision.

$$\eta = 0.499 \rho v_a L_m$$

[Dushman, 1962]

$$L_m = \frac{\eta}{0.499 \rho v_a}$$

Where:

$\eta$  = gas viscosity

$\rho$  = gas density

$v_a$  = mean molecular speed (not to be confused with the average gas velocity down the tube)

$L_m$  = mean free path

The mean molecular speed is determined as:

$$v_a = \left( \frac{8kT}{\pi m_H} \right)^{1/2} = \left( \frac{(8)(1.3807 \times 10^{-23}) \left[ \frac{kgm^2}{Ks^2} \right] (300)[K]}{(\pi)(1.6726 \times 10^{-27} [kg])} \right)^{1/2} = 2511 [m/s] \text{ [Dushman, 1962]}$$

At the inlet to the tube, the mean free path is:

$$L_m = \frac{\eta}{0.499 \rho v_a} = \frac{(8.89 \times 10^{-6}) \left[ \frac{kg}{ms} \right]}{(0.499)(1.17 \times 10^{-12}) \left[ \frac{kg}{cm^3} \right] \left[ \frac{100^2 cm^2}{m^2} \right] (2511) [m/s]} = 0.606 \text{ cm}$$

### Knudsen number

To verify the flow regime (Viscous, Molecular, or Transition), it is necessary to compare the Knudsen number to known threshold values for each regime. The Knudsen number is a dimensionless parameter, and is defined as the ratio of the mean free path of a molecule to the characteristic dimension of the path, in this case the tube radius.

$$Kn = \frac{L_m}{a} = \frac{(0.606) [cm]}{(1.5) [cm]} = 0.404$$

For  $Kn < 0.01$ , the flow is viscous.

For  $Kn > 1.00$ , the flow is molecular.

For  $0.01 < Kn < 1.00$  the flow is in the transition range.

According to the above calculations, the flow through the tube is initially in the transition region, and the above calculations performed using the assumption of viscous flow are invalid. However, it must be noted that this calculation of the Knudsen number is based on a calculation for the mean free path. This in turn is based on a calculation of density assuming viscous flow, which we know to be invalid. According to these calculations, as the flow travels down the length of the tube, the pressure decreases, the density

decreases, the mean free path increases, and the Knudsen number increases. Thus the flow will initially be in the transition region, and for the latter part of the tube it will be molecular.

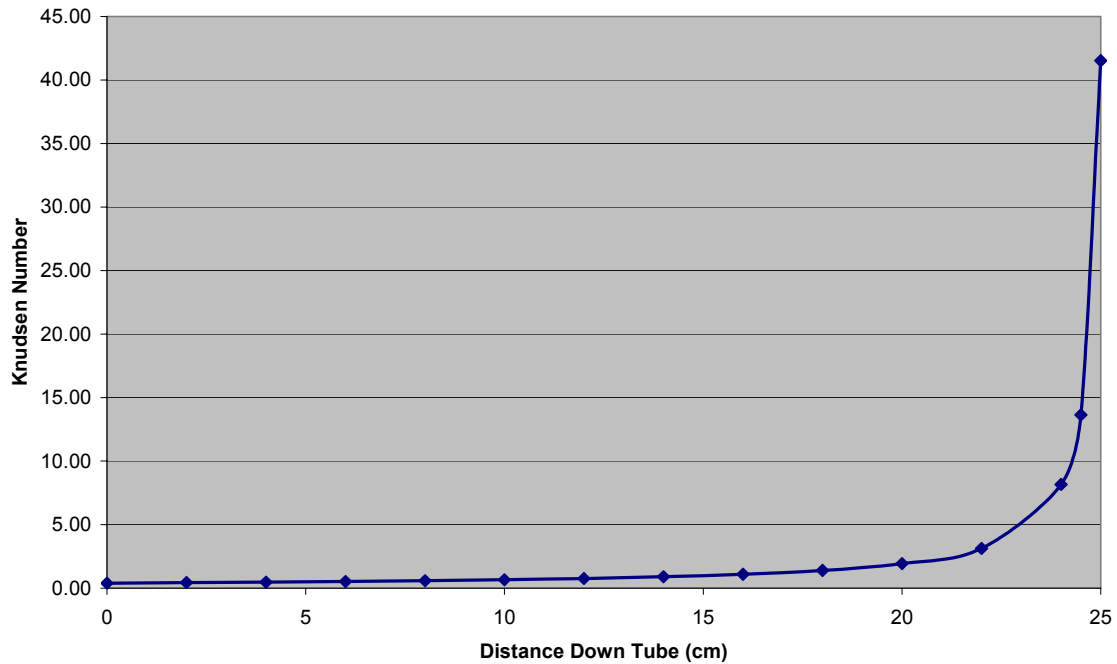


**Figure 4.4** Knudsen Number vs. Distance Down the Tube, According to Viscous Flow Calculations

## 4.2 Molecular Flow

Since the Knudsen number calculated above did not agree with the initial assumption of viscous flow at the tube inlet, we must disregard the results of those calculations and recalculate using a different assumption. We now make the assumption that the flow is in the molecular regime.

### Pressure and Flow at the Outlet:

Given the gas particle flow rate through the tube, gas temperature, tube radius, speed of sound in the gas, and using the assumption of  $M=1$  at the tube outlet; the pressure at the tube outlet is fixed. Copied from above:

$$M = \frac{U_{fa}}{c}, \quad U_{fa} = \frac{kT\dot{N}_H}{\pi a^2 P}$$

Combining equations and solving for P: 
$$P = \frac{kT\dot{N}_H}{\pi a^2 M c}$$

At the outlet,  $M = 1$  so the outlet pressure can be determined as:

$$P_{outlet} = \frac{(1.3807 \times 10^{-23}) \left[ \frac{kgm^2}{Ks^2} \right] (300) [K] (8.96 \times 10^{18}) \left[ \frac{1}{s} \right]}{(\pi)(0.015)^2 [m^2] (1)(1861.3) \left[ \frac{m}{s} \right]} = 0.028 [Pa]$$

$$= (0.028) [Pa] \left( \frac{1}{101.1k} \right) \left[ \frac{atm}{Pa} \right] (760) \left[ \frac{torr}{atm} \right] = 0.21 mtorr$$

The flow regime at this outlet pressure can be verified by calculating the Knudsen number. This is done by making use of the following definitions:

$$\text{Knudsen Number: } Kn = \frac{Lm}{a},$$

$$\text{Mean Free Path: } Lm = \frac{\eta}{0.499 \rho v_a},$$

$$\text{Gas Density: } \rho = \frac{m_H P}{kT}$$

$$\text{Mean molecular speed: } v_a = \left( \frac{8kT}{\pi m_H} \right)^{1/2} = 2511 \left[ \frac{m}{s} \right]$$

So:

$$Kn = \frac{Lm}{a} = \frac{\eta kT}{0.499 v_a a m_H P} = \frac{(8.99 \times 10^{-6}) \left[ \frac{kg}{ms} \right] (1.3807 \times 10^{-23}) \left[ \frac{kgm^2}{Ks^2} \right] (300) [K]}{(0.499)(2511) \left[ \frac{m}{s} \right] (0.015) [m] (1.67 \times 10^{-27}) [kg] P \left[ \frac{kg}{ms^2} \right]}$$

$$Kn = \frac{1.186}{P [Pa]}$$

At the tube outlet,  $P = 0.028 [Pa]$ , and  $Kn = 42.36$ . This indicates that the flow is molecular at the tube outlet.

For mean free paths greater than the characteristic dimension (tube radius in this case), or for Knudsen numbers greater than 1.00, the flow rate is controlled by gas particle collisions with the walls, as opposed to with other particles (as is the case with viscous flow). See the Figure 4.5 below.

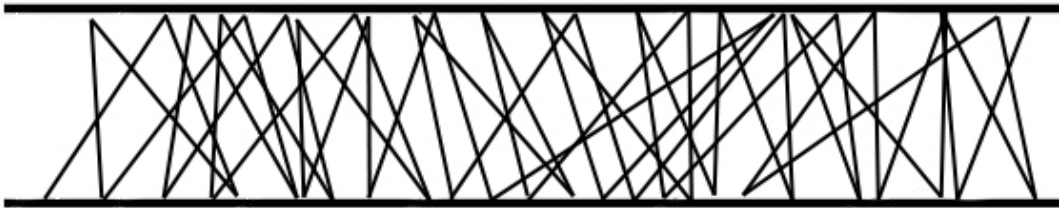


**Figure 4.5** Free Molecular Flow Through a Tube

Dushman provides a relation determined by Knudsen for gas molecular flow. Although not specified by Dushman, it is most likely derived by assuming diffuse collisions:

$$Q = \frac{4 v_a (\Delta P)}{3 \int_0^l \frac{H}{A^2} dl} \quad [\text{Dushman, 1962}]$$

Where:

$v_a$  = the mean molecular speed, calculated above as 2511[m/s]

$\Delta P$  = the pressure drop in the selected tube segment

$Q$  = volumetric flow rate times pressure:  $P\dot{V} = kT\dot{N}_H$

$H$  = perimeter of the tube =  $2\pi R$

$A$  = cross sectional area of the tube =  $\pi R^2$

The integration is to be performed from the beginning to the end of the tube segment. As a first approach, we will set the investigated tube segment to be the entire length of the tube, and determine if the molecular flow regime, and therefore this relationship for pressure drop in the tube, is valid across the entire tube length. If it is determined that it is valid, then no further calculation need be done to determine pressure along the tube. If the Reynolds number indicates that at some point along the tube, the flow enters the transitional regime, then the pressure can be determined from the end of the tube to that point through use of this relationship, and transitional flow relationships must be employed to determine the pressure throughout the rest of the tube.

$$\int_0^l \frac{H}{A^2} dl = \int_0^l \frac{2\pi R}{(\pi R^2)^2} dl = \frac{2}{\pi R^3} \int_0^l dl = \frac{2L}{\pi R^3}$$

$$Q = \frac{4 v_a (P_1 - P_2)}{3 \int_0^l \frac{H}{A^2} dl} = \frac{4 v_a (P_1 - P_2) \pi R^3}{3 (2)L} = \frac{2 \pi v_a (P_1 - P_2) R^3}{3 L}$$

$$\Delta P = \frac{3QL}{2\pi v_a R^3} = \frac{3kTL\dot{N}_H}{2\pi v_a R^3}$$

$$= \frac{(3)(1.3807 \times 10^{-23}) \left[ \frac{kgm^2}{Ks^2} \right] (300)[K](0.25)[m](8.96 \times 10^{18}) \left[ \frac{\#}{sec} \right]}{(2)(\pi)(2511) \left[ \frac{m}{s} \right] (0.015^3) [m^3]}$$

$$= 0.522 [Pa] = (0.522) [Pa] \left( \frac{1}{101.1k} \right) \left[ \frac{atm}{Pa} \right] (760) \left[ \frac{torr}{atm} \right] = 3.93 mtorr$$

The pressure at the tube inlet equals the pressure drop in the tube, plus the outlet pressure.

$$P_{inlet} = P_{outlet} + \Delta P = (0.028) [Pa] + (0.522) [Pa] = 0.55 [Pa] = 4.13 [mtorr]$$

Now one can use this input pressure to attempt to verify the flow regime at the inlet, and find other useful parameters.

### Knudsen Number at Inlet – Flow Regime Verification

Using the above derived relation,  $Kn = \frac{1.186}{P[Pa]}$

We find the Knudsen number at the inlet to be:  $Kn = \frac{1.186}{0.55} = 2.16$

Since  $Kn > 1$ , the flow is still in the molecular regime at the tube inlet, thus the above calculations for pressure throughout the tube are valid.

### Pressure as a Function of Distance Down the Tube (z)

Again we assume that the pressure varies linearly with distance down the tube, from a maximum value at the inlet to a minimum value at the outlet. This assumption can be considered valid, due to the fact that the flow does not change regime (it is molecular) throughout the entire length of the tube. The relationship between gas pressure and distance down the tube is:

$$P(z) = \left( \frac{0.028 - 0.55}{L} z + 0.55 \right) [Pa] = \left( \frac{0.028 - 0.55}{25} z + 0.55 \right) [Pa], \quad z \text{ in cm}$$

$$= (-2.088 \times 10^{-2} z + 0.55) [Pa], \quad z \text{ in cm}$$

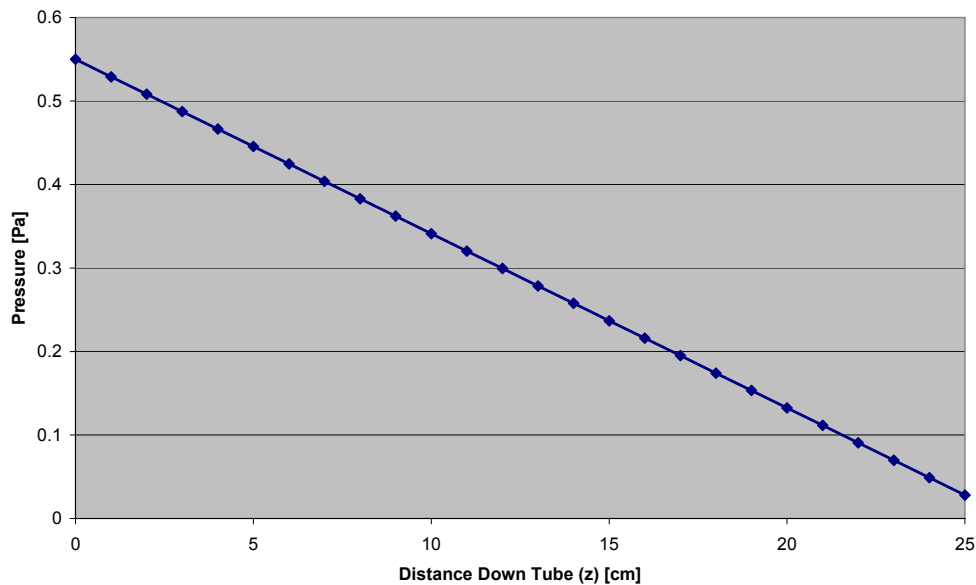


**Figure 4.6** Pressure vs. Distance Down the Tube – for a 1.5cm Radius, 25cm Long Tube

### Average Flow Velocity

$$U_{fa} = \frac{kT\dot{N}_H}{\pi R^2 P} = \frac{kT\dot{N}_H}{\pi R^2 (-2.088 \times 10^{-2} z + 0.55)}, \quad z \text{ in cm}$$

At the tube input,  $U_{fa} = 1875$  [m/s]

Mach Number

$$M = \frac{U_{fa}}{c}$$

At the tube input,  $M = 0.051$

Since  $M$  is  $< 1/3$ , the flow is subsonic at the inlet, and inertial effects can be neglected for much of the tube length. See Figure 4.7 below.

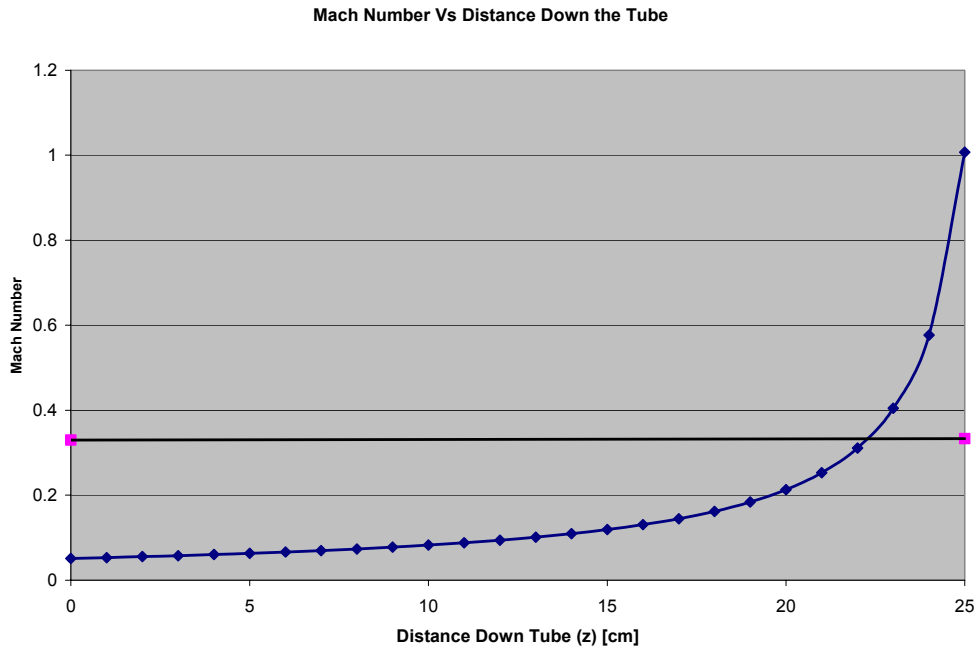


**Figure 4.7** Mach Number vs. Distance Down the Tube – for a 1.5cm Radius, 25cm Long Tube

Again it is observed that as the gas flows down the tube, the pressure will steadily drop until it reaches the outlet pressure. As the pressure drops, the average velocity of the gas ( $U_{fa}$ ), which is proportional to  $1/P$ , will increase. As a result, the Mach number will also increase, until the flow reaches  $M=1$  at the outlet. From the above graph of Mach number versus distance down the tube, we can see that for the last ~12% of the tube,  $M > 1/3$ , so flow inertial effects should be taken into account.

Gas Density as a Function of (z)

$$\rho = \frac{m_H P}{kT} = \frac{(1.6726 \times 10^{-27}) [kg]}{(1.3807 \times 10^{-23}) \left[ \frac{kgm^2}{s^2K} \right] (300) [K]} (-2.088 \times 10^{-2} z + 0.55) \left[ \frac{kg}{ms^2} \right]$$



$$= (4.038 \times 10^{-7}) (-2.088 \times 10^{-2} z + 0.55) \left[ \frac{kg}{m^3} \right], z \text{ in cm}$$

This formula yields the density at the tube inlet as:

$$\rho = (4.038 \times 10^{-7}) (-2.088 \times 10^{-2} (0) + 0.55) = 2.22 \times 10^{-7} \left[ \frac{kg}{m^3} \right] = 2.22 \times 10^{-13} \left[ \frac{kg}{cm^3} \right]$$

The number density can be calculated as:

$$n = \frac{\rho N_A}{M_H} = \frac{(6.022 \times 10^{23}) \left[ \frac{\#}{mole} \right]}{(1.00794) \left[ \frac{g}{mole} \right] \left( \frac{1}{1000} \right) \left[ \frac{kg}{g} \right]} \left( (4.038 \times 10^{-7}) (-2.088 \times 10^{-2} z + 0.55) \right) \left[ \frac{kg}{m^3} \right]$$

$$= 2.41 \times 10^{20} (-2.088 \times 10^{-2} z + 0.55) \left[ m^{-3} \right], z \text{ in cm}$$

At the tube inlet, the number density is:

$$n = 2.41 \times 10^{20} (-2.088 \times 10^{-2} (0) + 0.55) \left[ m^{-3} \right] = 1.33 \times 10^{20} \left[ m^{-3} \right] = 1.33 \times 10^{14} \left[ cm^{-3} \right]$$

Figure 4.8 below shows number density versus distance down the tube.

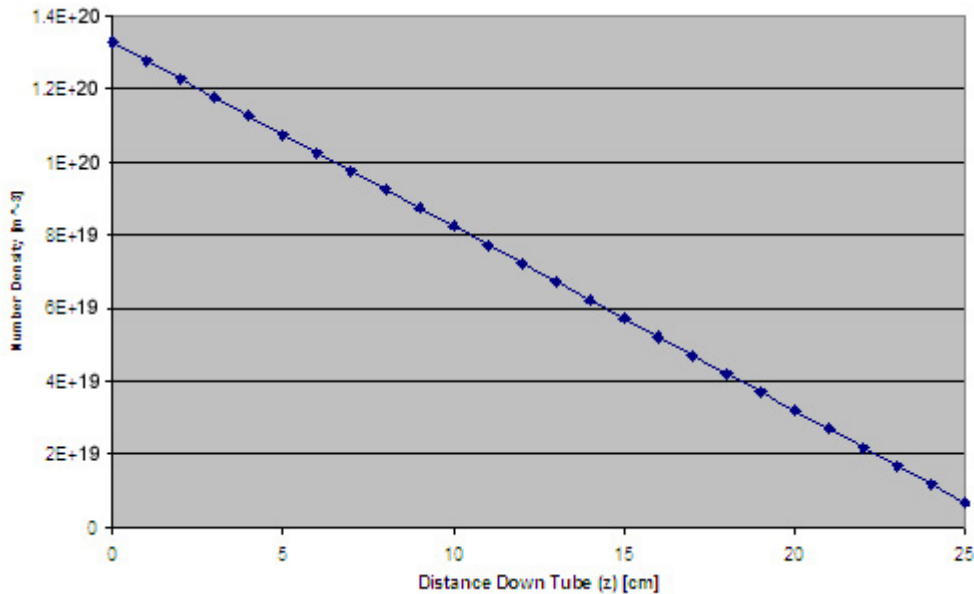


**Figure 4.8** Number Density vs. Distance Down the Tube – for a 1.5cm Radius, 25cm Long Tube

Mean Free Path as a Function of z

$$L_m = \frac{\eta}{0.499 \rho v_a} = \frac{(8.89 \times 10^{-6}) \left[ \frac{kg}{ms} \right]}{(0.499) \left( (4.038 \times 10^{-7}) (-2.088 \times 10^{-2} z + 0.55) \right) \left[ \frac{kg}{m^3} \right] (2511) [m/s]}$$

$$= \frac{1.76 \times 10^{-2}}{\left( (-2.088 \times 10^{-2} z + 0.55) \right)} [m], z \text{ in cm}$$

At the inlet to the tube (z=0), the mean free path is:

$$L_m = 0.032 [m] = 3.2 [cm]$$

Knudsen Number – Revisited

For completeness, the Knudsen number along the length of the tube can be plotted, as shown in Figure 4.9 below.

$$Kn = \frac{1.186}{P [Pa]} = \frac{1.186}{(-2.088 \times 10^{-2} z + 0.55)}$$

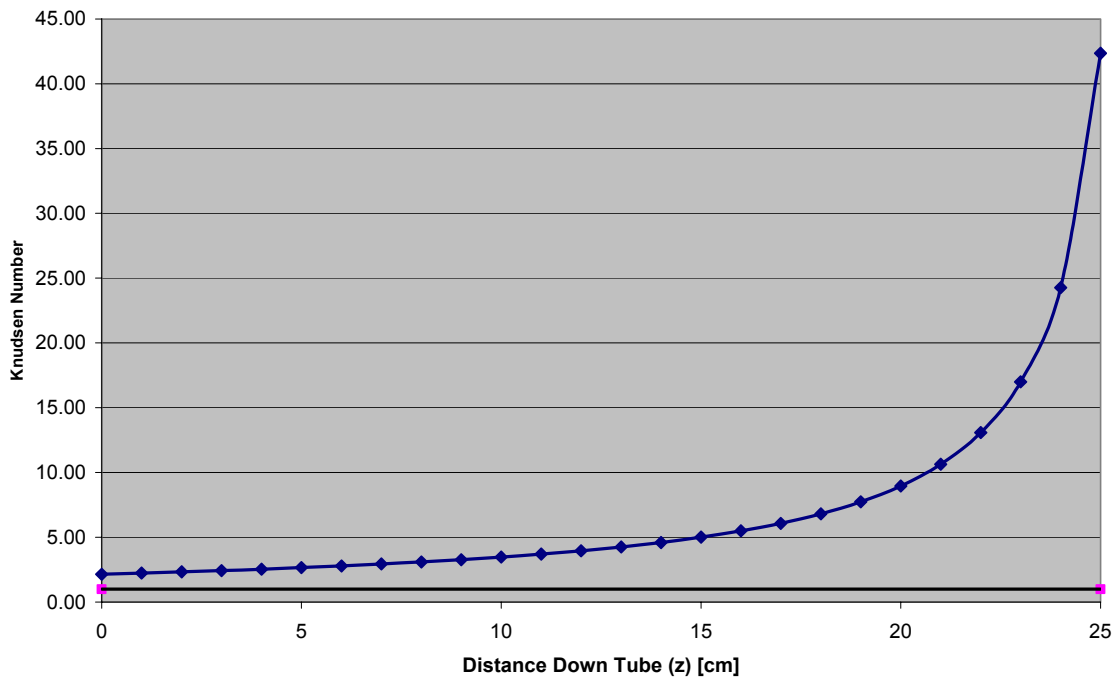


**Figure 4.9** Knudsen Number vs. Distance Down the Tube – for a 1.5cm Radius, 25cm Long Tube

One can see from this graph that the Knudsen number remains above the transition regime. The flow is in the molecular regime throughout the tube, for this set of parameters.

### 4.3 Parametric Analysis

To gain greater understanding of the physical relationships involved, parametric analysis was completed. Variation in flow parameters was examined for a range of tube radius values, and for a range of inlet temperatures.

#### 4.3.1 Variation of Radius

First we will vary the radius of the tube (constant along tube length) and see the effect on the gas flow. The radius is still limited by the size of the available magnet, and thus cannot be larger than 5cm. The intention is to create a compact device, thus we will focus on smaller tube diameters, examining a range of values between 0.25 cm and 2.5cm.

Note that other parameters remain unchanged from the baseline calculations. This includes  $T=300K$ ,  $L=25cm$ , and  $\dot{V}_{in} = 10 \text{ scfm}$ .

##### Effect on Output Pressure:

Assuming  $M=1$  at the outlet,  $P$  at the outlet can be determined as:

$$P_{outlet} = \frac{kT\dot{N}_H}{\pi a^2 M c} = \frac{kT\dot{N}_H}{\pi a^2 (1)c}$$

This result is illustrated in Figure 4.10 below for tube radii between 0.25 and 2.5 cm.

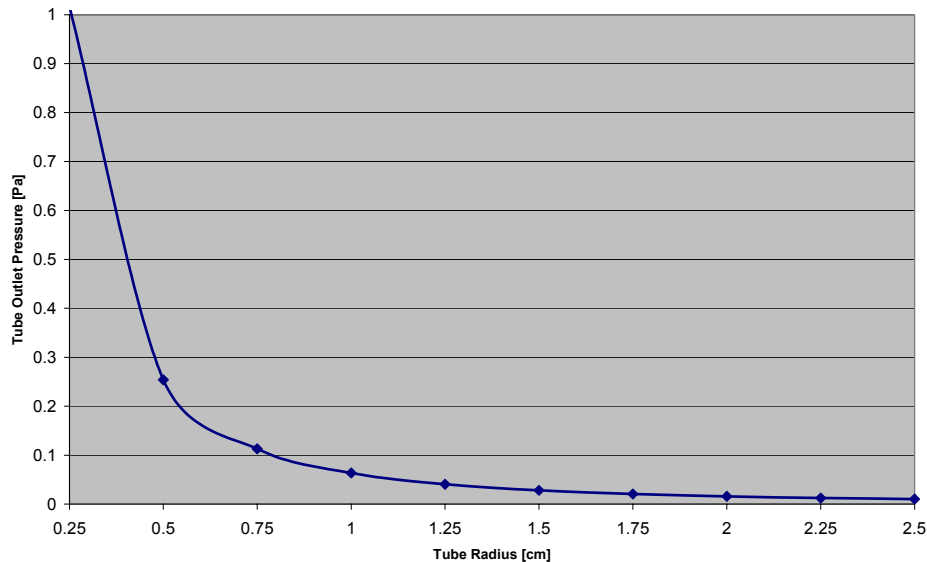


**Figure 4.10** Tube Outlet Pressure vs. Tube Radius,  $M=1$  at Outlet Boundary Condition

The mean molecular speed is independent of tube radius,  $v_a = 2511 \left[ \frac{m}{s} \right]$ .

We verify the flow regime at the tube outlet by calculating the Knudsen number:

$$Kn_{outlet} = \frac{Lm_{outlet}}{a} = \frac{\eta kT}{0.499v_a a m_H P_{outlet}} = \frac{\pi a^2 c \eta kT}{0.499v_a a m_H kT \dot{N}_H} = \frac{\pi a c \eta}{0.499v_a m_H \dot{N}_H}$$

We can see in the figure below that the Knudsen number at the tube outlet increases linearly with radius, and remains at all times in the molecular regime at the outlet ( $Kn > 1$ ).

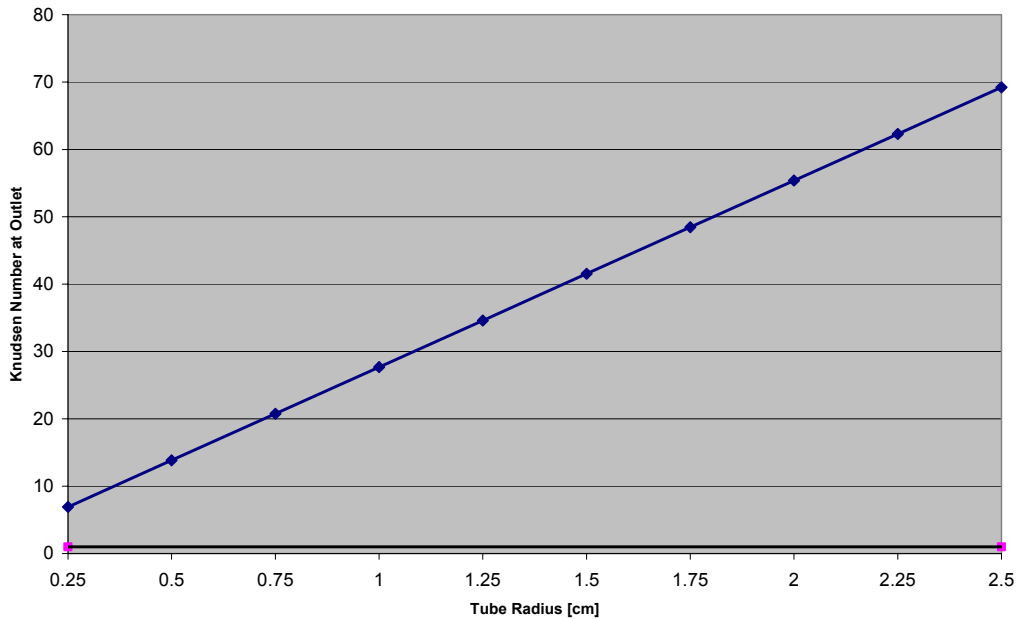


**Figure 4.11** Knudsen Number at Tube Outlet vs. Tube Radius,  $M=1$  at Outlet Boundary Condition

Using the relations for molecular flow,  $\Delta P$  can be calculated for a segment of tube:

$$\Delta P = \frac{3kT\dot{N}_H}{2\pi v_a} \frac{L}{R^3}, \text{ where } L[\text{m}] \text{ is the length of the tube segment.}$$

We will again assume that the flow is molecular throughout the length of the tube, and thus use the molecular flow relation above to calculate the pressure drop in the entire tube length, and the pressure at the tube inlet. Then we can verify the validity of this assumption by calculating the Knudsen number at the tube inlet.

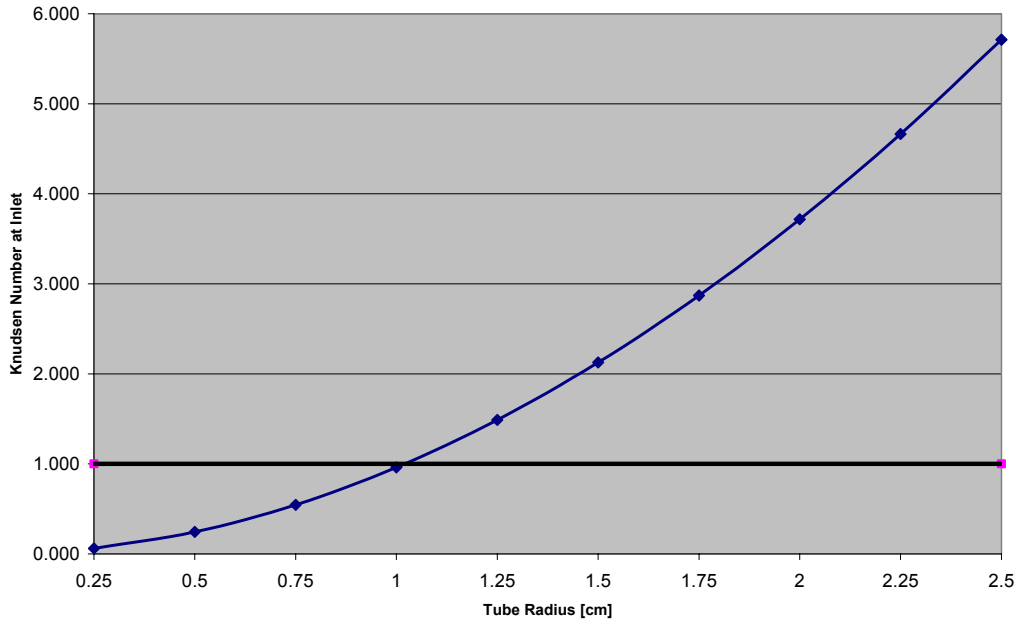


**Figure 4.12** Knudsen Number at Tube Inlet vs. Tube Radius, Assume All Molecular Flow

$$Kn = \frac{Lm}{a} = \frac{\eta k T}{0.499 v_a m_H P}$$

We can see from this graph, that for tube radii larger than or equal to 1 cm, one can assume the flow through the tube to be molecular throughout, and the molecular flow relations for pressure along the tube valid. For radii smaller than 1 cm, the molecular flow relations are only valid for a portion of the tube length, and the pressure must be calculated using transitional flow or viscous flow relations.

We seek the pressure distribution along the length of the tube, for each tube radius selected. For those radii where the flow remains molecular throughout, one can use the molecular flow relations above to obtain the pressure distribution in a straightforward manner.

$$P(z) = \Delta P_{OutletToZ} + P_{outlet}$$

$$\Delta P_{OutletToZ} = \frac{3kTL_i \dot{N}_H}{2\pi v_a R^3} = \frac{3kT \dot{N}_H}{2\pi v_a R^3} (L - z),$$

Where :

L is length of tube.

z is the distance to the point of interest down the tube from the inlet.

For radii greater than or equal to 1 cm, where we can assume the flow is molecular throughout, pressure distribution throughout the tube has been calculated. For radii

smaller than 1 cm, the molecular flow relations are only valid for a portion of the tube length. To determine the point at which this transition takes place, the pressure is calculated at 1 cm increments along the tube, and the Knudsen number is determined at each location. The point at which the Knudsen number drops below 1, marks the limit of validity of the molecular pressure relation. Pressure values for shorter distances down the tube, where the Knudsen number is less than one, will be calculated through another method detailed shortly. The pressure distribution throughout the tube, where the molecular relations are valid, is graphed in Figure 4.13 below.

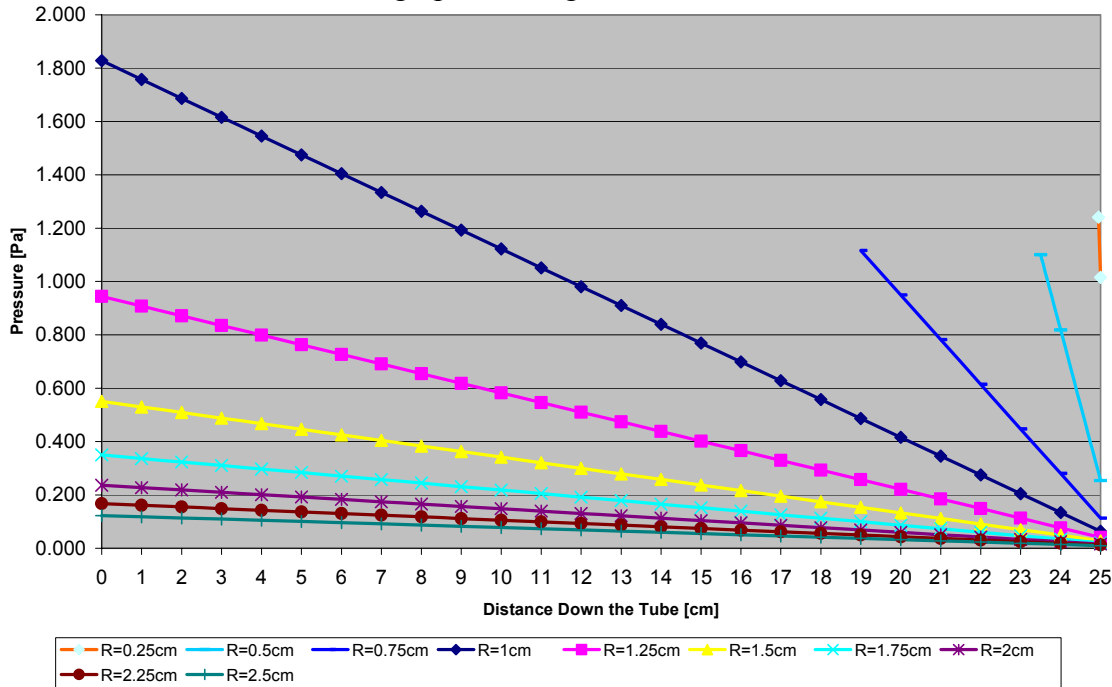


**Figure 4.13** Pressure vs. Distance Down the Tube – for Various Tube Radii

Tube Radius [cm]	Length Down the Tube (z) at which change from molecular to transitional flow occurs [cm]	Pressure at this point [Pa]
0.25	24.95	1.241
0.5	23.5	1.101
0.75	19	1.117

**Table 4.1** Molecular to Transitional Flow Regime – Transition Distances and Pressures for Three Different Tube Radii

For distances down the length of the tube, where the Knudsen number is less than 1, pressure drop must be calculated using either transitional flow or viscous flow relations. We will make an assumption that the flow through the remainder of the tube length will remain in the transition region, and thus use the transitional flow relations to determine the pressure drop in the remaining length of the tube. The pressure at the tube inlet can then be calculated by adding this pressure drop to the now known pressure at the boundary point where the flow becomes molecular. Again the assumption of transitional

flow in the remainder of the tube length will be checked by calculating the Knudsen number at the tube inlet.

A formula for the conductance of a long cylindrical tube was determined by Knudsen as:

$$F = F_v + ZF_t \quad [\text{Dushman, 1962}]$$

Where:

$F_v$  is the “slip-free” viscous conductance

$F_t$  is the molecular flow conductance of a long tube

$$F_v = \frac{\pi R^4}{8\eta L} P_a = \frac{\pi R^4 (P_1 + P_2)}{16\eta L} \quad [\text{Dushman, 1962}]$$

$$F_t = \frac{2\pi R^3}{3L} v_a = \frac{2\pi R^3}{3L} \left( \frac{8kT}{\pi m_H} \right)^{1/2} \quad [\text{Dushman, 1962}]$$

$$Z = \frac{1 + 2.507(R/L_a)}{1 + 3.095(R/L_a)}$$

Where:

$L_a$  is the mean free path corresponding to the average pressure  $P_a$ .

$$L_a = \frac{\eta}{0.499 \rho v_a} = \frac{\eta}{0.499 \left( \frac{m_H P_a}{kT} \right) \left( \frac{8kT}{\pi m_H} \right)^{1/2}} = \frac{\eta}{0.499 \left( \frac{m_H (P_1 + P_2)}{2kT} \right) \left( \frac{8kT}{\pi m_H} \right)^{1/2}}$$

Flow conductance (F) is defined in general as:

$$F = \frac{Q}{P_1 - P_2} = \frac{kT \dot{N}_H}{(P_1 - P_2)} \quad [\text{Dushman, 1962}]$$

$$\frac{kT \dot{N}_H}{(P_1 - P_2)} = F_v + ZF_t$$

$$\frac{kT \dot{N}_H}{(P_1 - P_2)} = \left( \frac{\pi R^4 (P_1 + P_2)}{16\eta L} \right) + \left( \frac{1 + 2.507(R/L_a)}{1 + 3.095(R/L_a)} \right) \left( \frac{2\pi R^3}{3L} \left( \frac{8kT}{\pi m_H} \right)^{1/2} \right)$$

$$\frac{kT\dot{N}_H}{(P_1 - P_2)} = \left( \frac{\pi R^4 (P_1 + P_2)}{16\eta L} \right) + \frac{\left( 1 + \frac{2.507R}{\frac{\eta}{0.499 \left( \frac{m_H (P_1 + P_2)}{2kT} \right) \left( \frac{8kT}{\pi m_H} \right)^{1/2}}} \right)}{\left( 1 + \frac{3.095R}{\frac{\eta}{0.499 \left( \frac{m_H (P_1 + P_2)}{2kT} \right) \left( \frac{8kT}{\pi m_H} \right)^{1/2}}} \right)} \left( \frac{2\pi R^3}{3L} \left( \frac{8kT}{\pi m_H} \right)^{1/2} \right)$$

$$\Delta P = P_1 - P_2, \quad P_1 = \Delta P + P_2$$

$$\frac{kT\dot{N}_H}{\Delta P} = \left( \frac{\pi R^4 (\Delta P + 2P_2)}{16\eta L} \right) + \frac{\left( \frac{2\eta kT + (2.507)R(0.499)m_H (\Delta P + 2P_2)v_a}{2\eta kT} \right)}{\left( \frac{2\eta kT + (3.095)R(0.499)m_H (\Delta P + 2P_2)v_a}{2\eta kT} \right)} \left( \frac{2\pi R^3}{3L} v_a \right)$$

$$\frac{kT\dot{N}_H}{\Delta P} \frac{\pi R^4}{16\eta L} \Delta P + \frac{\pi R^4 P_2}{8\eta L} = + \left( \frac{2\eta kT + (2.507)R(0.499)m_H v_a \Delta P + (2)(2.507)R(0.499)m_H v_a P_2}{2\eta kT + (3.095)R(0.499)m_H v_a \Delta P + (2)(3.095)R(0.499)m_H v_a P_2} \right) \left( \frac{2\pi R^3}{3L} v_a \right)$$

$$\frac{a}{\Delta P} = b\Delta P + c + \left( \frac{d + e\Delta P + f}{d + g\Delta P + h} \right) i$$

$$a = b(\Delta P)^2 + c\Delta P + \left( \frac{di\Delta P + ei(\Delta P)^2 + fi\Delta P}{d + g\Delta P + h} \right)$$

$$a - b(\Delta P)^2 - c\Delta P = \left( \frac{di\Delta P + ei(\Delta P)^2 + fi\Delta P}{d + g\Delta P + h} \right)$$

$$(a - b(\Delta P)^2 - c\Delta P)(d + g\Delta P + h) = (di\Delta P + ei(\Delta P)^2 + fi\Delta P)$$

And we arrive at a cubic equation for pressure drop in the tube segment:

$$(bg)(\Delta P)^3 + (ei + bd + bh + cg)(\Delta P)^2 + (di + fi - ag + cd + ch)\Delta P - a(d + h) = 0$$

Where:

$$a = kT\dot{N}_H$$

$$b = \frac{\pi R^4}{16\eta l}$$

$$c = \frac{\pi R^4 P_2}{8\eta l}$$

$$d = 2\eta kT$$

$$e = (2.507)(0.499)Rm_H v_a$$



$$f = e(2)(P_2)$$

$$g = (3.095)(0.499)Rm_H v_a$$

$$h = g(2)(P_2)$$

$$i = \frac{2\pi R^3 v_a}{3l}$$

A Matlab program has been created to find the solution of this cubic equation. Adding this pressure drop to the value of the pressure at the molecular / transitional flow boundary, we obtain the pressure at the tube inlet, and then can calculate the Knudsen number at the inlet. The results are depicted in Table 4.2 below.

$$Kn = \frac{Lm}{a} = \frac{\eta kT}{0.499 v_a a m_H P} = \frac{(8.99 \times 10^{-6})(1.3807 \times 10^{-23})(300)}{(0.499)(2511)(R)(1.6726 \times 10^{-27})P}$$

Tube Radius [cm]	Length Down the Tube (z) at which change from molecular to transition flow occurs [cm]	Pressure at this point [Pa]	Pressure Drop from z to Tube Inlet (assume all transitional flow) [Pa]	Pressure at Tube Inlet [Pa]	Knudsen Number at Tube Inlet
0.25	24.95	1.241	70.83	72.071	0.099
0.5	23.5	1.101	11.75	12.851	0.277
0.75	19	1.117	3.12	4.237	0.559

**Table 4.2** Pressures Calculated in Transitional Flow Regime for 3 Different Tube Radii

Thus, since the Knudsen number at the tube inlet in each case is between 1 and 0.01, the flow is transitional through the remainder of the tube. Thus the transitional flow equations yield the correct values of the pressure at the inlet, and at all points between the inlet and the molecular / transitional flow boundary. The pressure distribution throughout the tube, including both the molecular and transition regions, is graphed below.

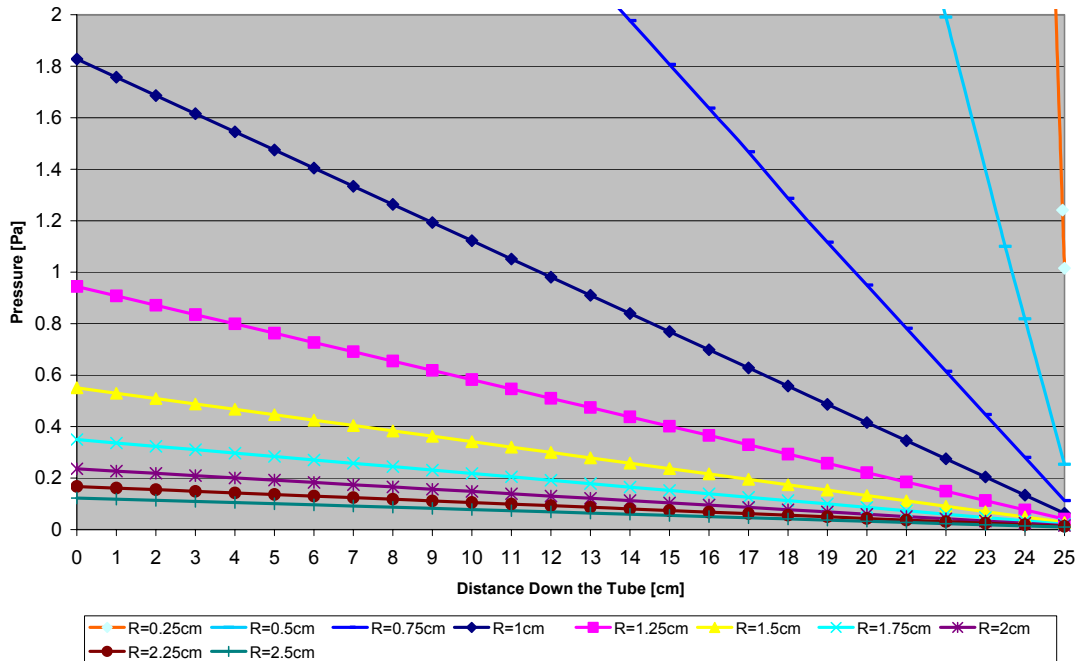


**Figure 4.14** Pressure vs. Distance Down the Tube for Various Radii – Including Both Molecular and Transition Regions

Effect on Other Parameters:

The effect of tube radius on other parameters has been calculated using the same relations detailed above. The results are depicted in the following graphs, for Mach Number, Number Density, and Knudsen Number vs. Distance Down the Tube.

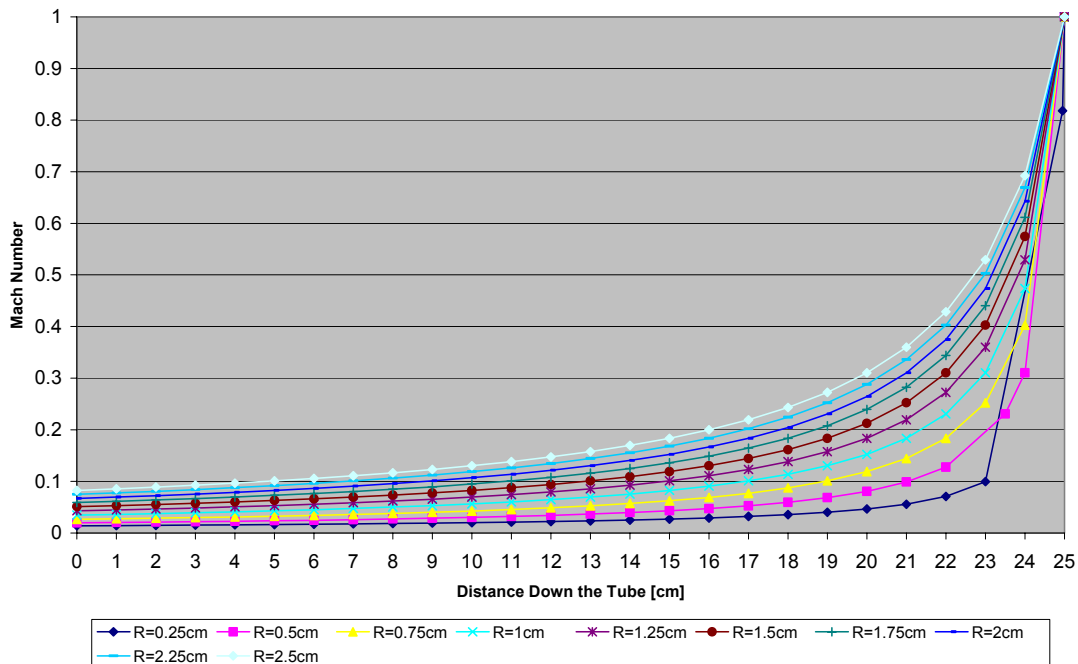


**Figure 4.15** Mach Number vs. Distance Down the Tube for Various Radii – Including Both Molecular and Transition Regions

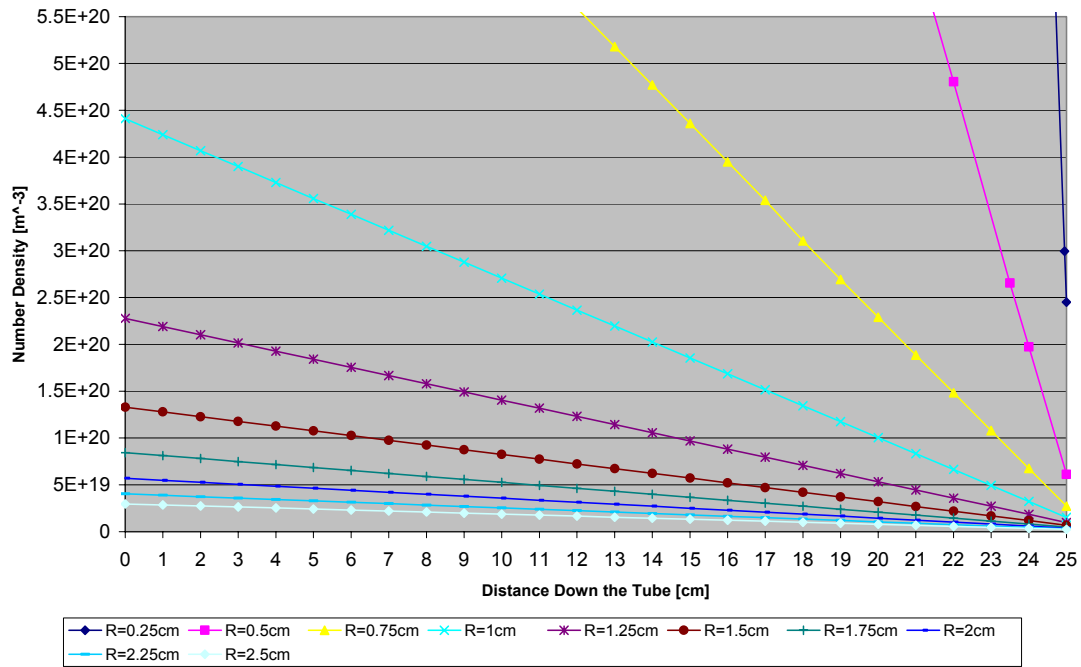


**Figure 4.16** Number Density vs. Distance Down the Tube for Various Radii – Including Both Molecular and Transition Regions

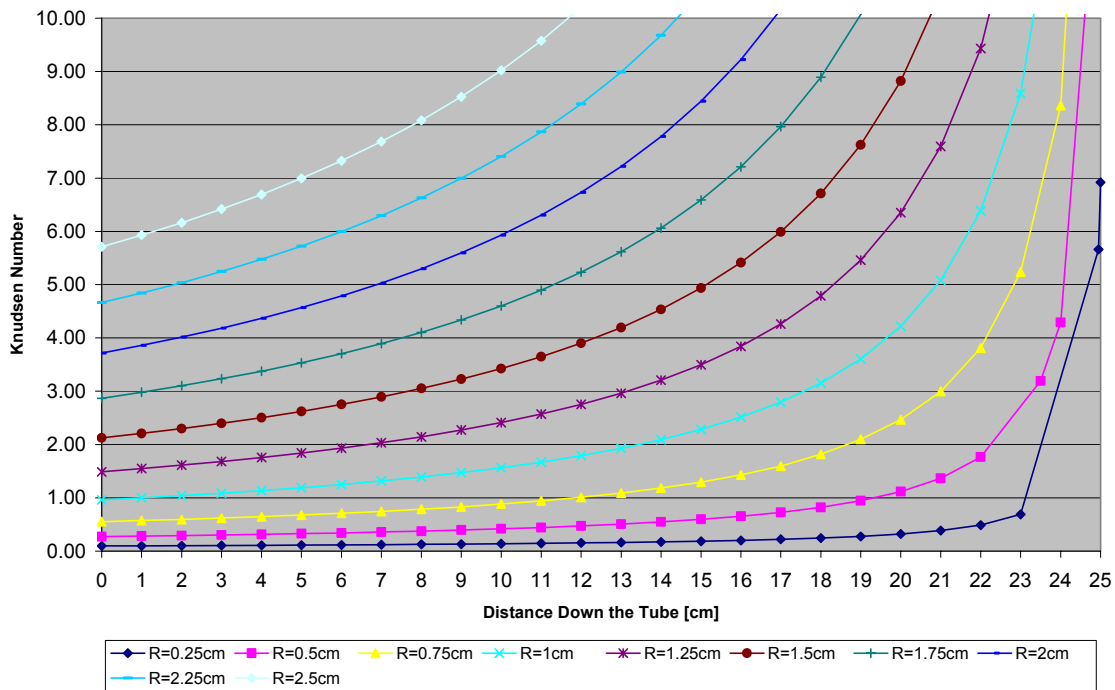


**Figure 4.17** Knudsen Number vs. Distance Down the Tube for Various Radii – Including Both Molecular and Transition Regions

### 4.3.2 Variation of Temperature

Now we will explore the effect of variation in inlet gas temperature. It is assumed that gas enters the tube at room temperature (~300K) and the flow is isothermal throughout. However, due to various effects, the inlet temperature may be elevated above this level. Variation in other parameters will be examined for a range of temperatures between 300K and 700K, in 100K increments.

Note that other parameters remain unchanged from the baseline calculations. This includes  $R=1.5\text{cm}$ ,  $L=25\text{cm}$ , and  $\dot{V}_{in} = 10 \text{ sccm}$ .

#### Effect on Output Pressure:

Assuming  $M=1$  at the outlet,  $P$  at the outlet can be determined as:

$$P_{outlet} = \frac{kT\dot{N}_H}{\pi a^2 M c} = \frac{kT\dot{N}_H}{\pi a^2 (1)c}$$

But the speed of sound in the gas is proportional to the square root of the gas temperature as:

$$c = \sqrt{\kappa T \frac{R_0}{M_H}} \quad [\text{Olsen, 1990}]$$

Where:

$$\kappa = \text{Adiabatic index for the gas} = \frac{c_p}{c_v} = 1.40 \text{ for } H_2 \quad [\text{Olsen, 1990}]$$

$T$  = gas temperature

$$R_0 = \text{universal gas law constant} = (8.3145) \left[ \frac{J}{Kmol} \right]$$

$$M_H = \text{molar mass of the gas} = (1.00794) \left[ \frac{g}{mol} \right] = 0.00101 \left[ \frac{kg}{mol} \right]$$

The pressure at the tube outlet, as a function of temperature, is graphed in Figure 4.18 below.

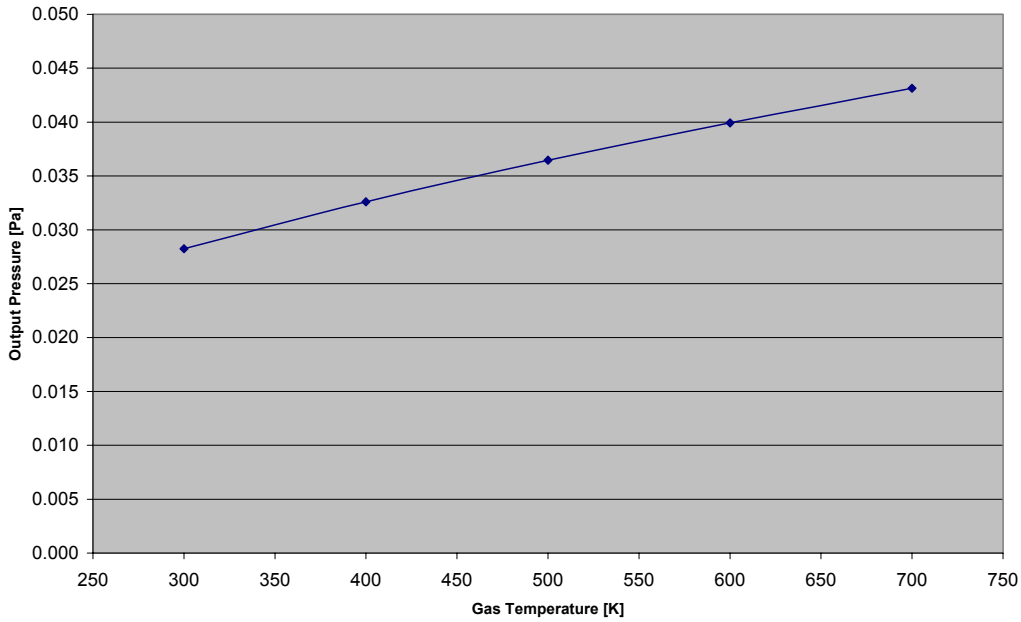


**Figure 4.18** Tube Outlet Pressure vs. Gas Temperature,  $M=1$  at Outlet Boundary Condition

The mean molecular speed is also dependent on temperature:

$$v_a = \left( \frac{8kT}{\pi m_H} \right)^{1/2}$$

Also the gas viscosity is dependant on temperature. Values have been obtained from the LNNO Engineering Gas Viscosity Calculator [LNNO Eng, 2003] for the temperatures of interest.

Table 4.3 below lists values for the speed of sound, tube outlet pressure, mean molecular speed and gas viscosity for different gas temperatures.

Gas Temperature [K]	Speed of Sound in the Gas [m/s]	Tube Outlet Pressure [Pa]	Mean Molecular Speed [m/s]	Gas Viscosity [kg/ms]
300	1859	0.028	2511	$8.89 \times 10^{-6}$
400	2147	0.033	2900	$1.07 \times 10^{-5}$
500	2401	0.036	3242	$1.24 \times 10^{-5}$
600	2630	0.04	3551	$1.39 \times 10^{-5}$
700	2840	0.043	3836	$1.53 \times 10^{-5}$

**Table 4.3** Variation of Gas Characteristics with Inlet Temperature

We verify the flow regime at the tube outlet by calculating the Knudsen number:

$$Kn_{outlet} = \frac{Lm_{outlet}}{a} = \frac{\eta k T}{0.499 v_a a m_H P_{outlet}}$$

Substitution of appropriate values yields Knudsen numbers at the tube outlet of 42, 49, 59, 65, and 72 for temperatures between 300K and 700K. Thus the tube outlet remains for all temperatures in the molecular region.

Using the relations for molecular flow, delta P can be calculated for a segment of tube:

$$\Delta P = \frac{3kT\dot{N}_H}{2\pi v_a} \frac{L}{a^3}, \text{ where } L[\text{m}] \text{ is the length of the tube segment.}$$

We will again assume that the flow is molecular throughout the length of the tube, and thus use the molecular flow relation above to calculate the pressure drop in the entire tube length, and the pressure at the tube inlet. Then we can verify the validity of this assumption by calculating the Knudsen number at the tube inlet.

$$Kn = \frac{Lm}{a} = \frac{\eta kT}{0.499v_a a m_H P}$$

Substitution of appropriate values yields Knudsen numbers at the tube inlet of 2.1, 2.6, 3, 3.3, and 3.7 for temperatures between 300K and 700K. Thus the entire tube remains in the molecular region for all temperatures.

Again we can use the relation below to obtain the pressure distribution along the length of the tube, for each temperature selected.

$$P(z) = \Delta P_{\text{OutletToZ}} + P_{\text{outlet}}$$

$$\Delta P_{\text{OutletToZ}} = \frac{3kTL_i\dot{N}_H}{2\pi v_a R^3} = \frac{3kT\dot{N}_H}{2\pi v_a R^3} (L - z), \text{ where } L \text{ is length of tube, and } z \text{ is the distance to}$$

the point of interest down the tube from the inlet.

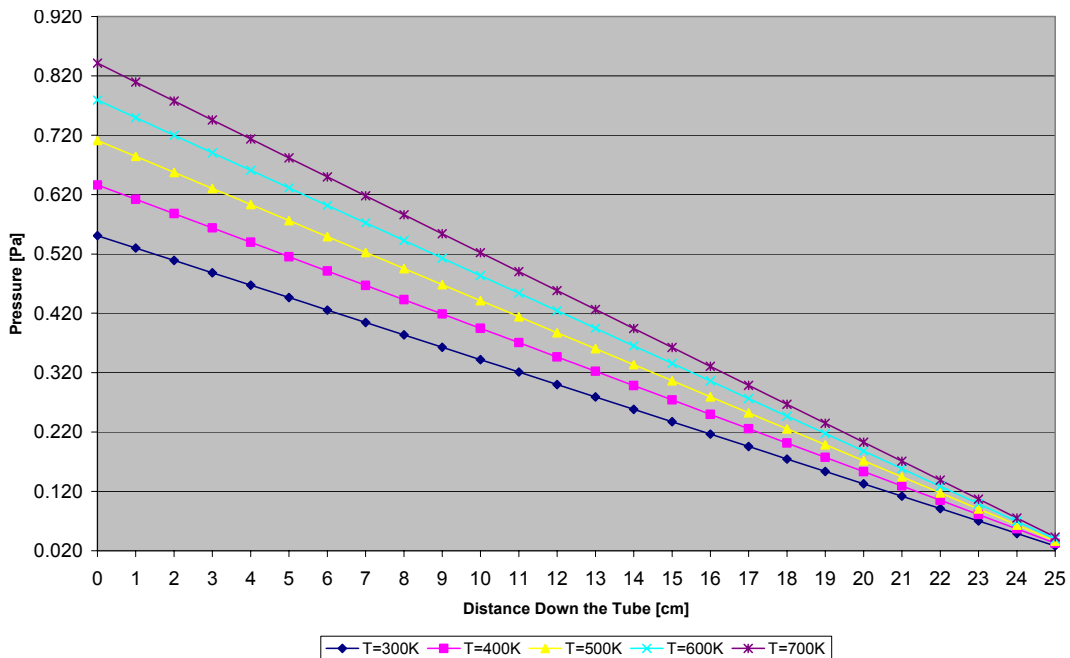


**Figure 4.19** Pressure vs. Distance Down the Tube – for Various Gas Temperatures

Effect on Other Parameters:

The effect of gas temperature on other parameters has been calculated using the same relations detailed above. The results are depicted in the following graphs: for Mach Number and Number Density vs. Distance Down the Tube. Note, gas temperature has no effect on Mach Number throughout the tube.

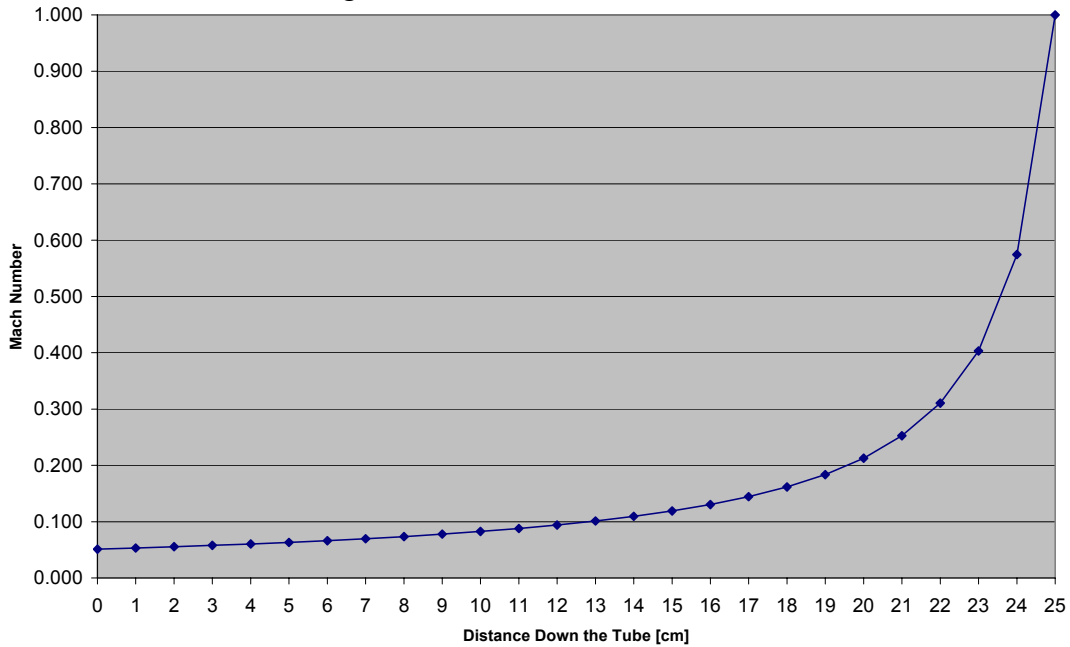


**Figure 4.20** Mach Number vs. Distance Down the Tube – for Various Gas Inlet Temperatures

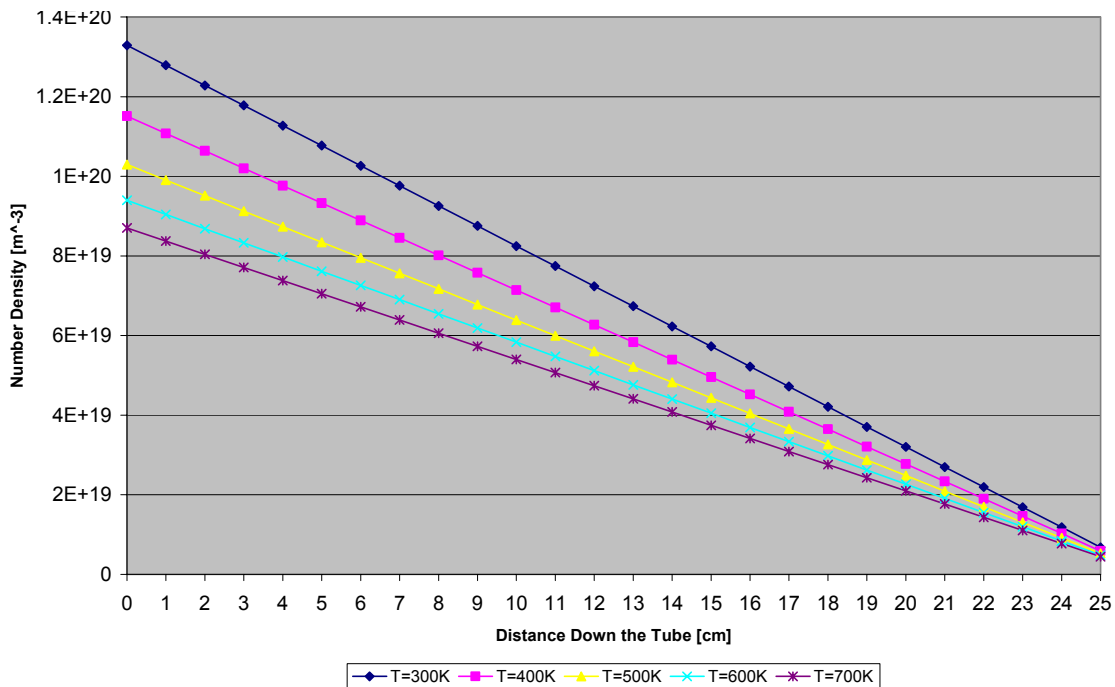


**Figure 4.21** Number Density vs. Distance Down the Tube – for Various Gas Inlet Temperatures





# Chapter 5

## MECHANICAL SUPPORT STRUCTURE DESIGN & CONSTRUCTION

One of this author's contributions to the mHTX@MIT experimental setup was the design and construction of the mechanical support structure. This structure was designed to meet certain requirements imposed by the greater experiment design and was constrained by the need to interface with the existing SPL vacuum chamber. CAD design of a proposed structure was completed. Structural analysis of that proposed structure was then undertaken, to determine if it met the applied requirements and constraints. Some modifications were made to the proposed design to improve its capabilities. Finally the structure components were machined and assembled by the author, and the completed structure was installed in the SPL vacuum chamber.

### 5.1 Structure Requirements

A mechanical structure was required in order to support the experimental setup within the SPL vacuum chamber. The desire was to create a structure that was both robust enough to support the experiment and stable enough to maintain the location of the experiment within the chamber as a fixed reference for various measurements.

The most massive elements of the experimental apparatus are the wound copper electromagnetic coils and their aluminum support bobbins. Each coil/bobbin assembly weighs approximately 60kg. Early experiments will utilize two of these coils. In order to provide experimental flexibility, it was required that the stand be designed to accommodate the future addition of a third electromagnetic coil. The design of these coils is described in Section 3.1.4, and depicted, with reference dimensions labeled, in Figure 5.1 below.

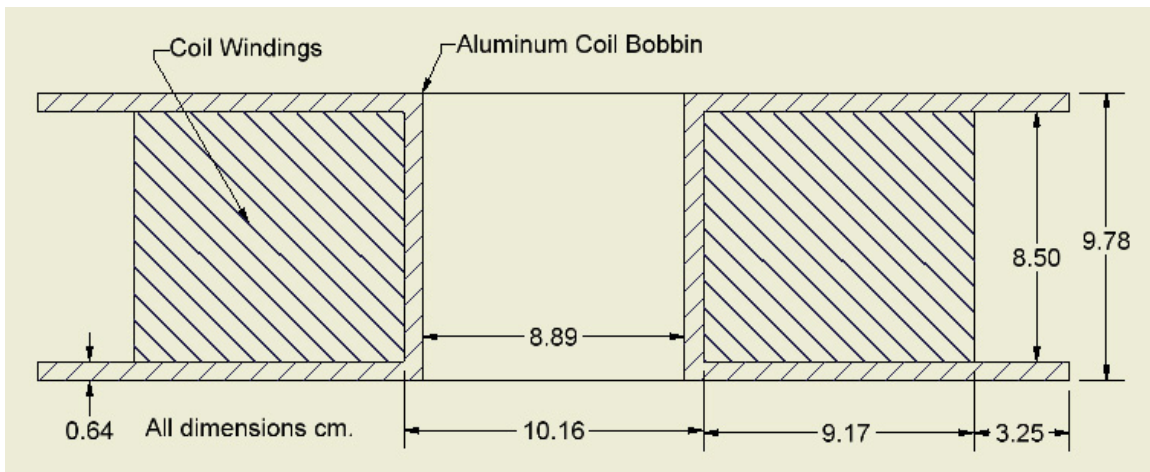


**Figure 5.1** Electromagnetic Coil on Aluminum Bobbin

As previously stated, the electromagnetic coils were designed to operate as a Helmholtz pair in order to provide a uniform axial magnetic field. This drove the design of the coil dimensions, and fixed the distance between them equal to their inner radius. This dimension is maintained by the threaded tie rods and aluminum spacers which hold the coil assembly together. Thus, the mechanical support structure, while required to support the mass of this assembly, does not need to actively maintain the coil spacing.

An additional requirement of the mechanical support structure is the ability to incorporate a plume measurement swing arm assembly at some future date. It is desirable to design the structure such that this swing arm assembly is allowed to swing through the widest possible angular displacement. This will allow for full characterization of plume parameters.

## 5.2 CAD Design

The design of the mechanical support structure involved use of Autodesk Inventor 7.0, 3D rendering software.<sup>1</sup> This software was used to draw the individual components and to combine them into a total virtual assembly. This was a very worthwhile effort, as it allowed visualization of the finished assembly prior to actual construction, providing feedback on clearances and on the validity of various dimensions. The designed structure is rendered in Figure 5.2 below, with depictions of the electromagnetic coils, quartz tube, and plume swing arm included for reference.

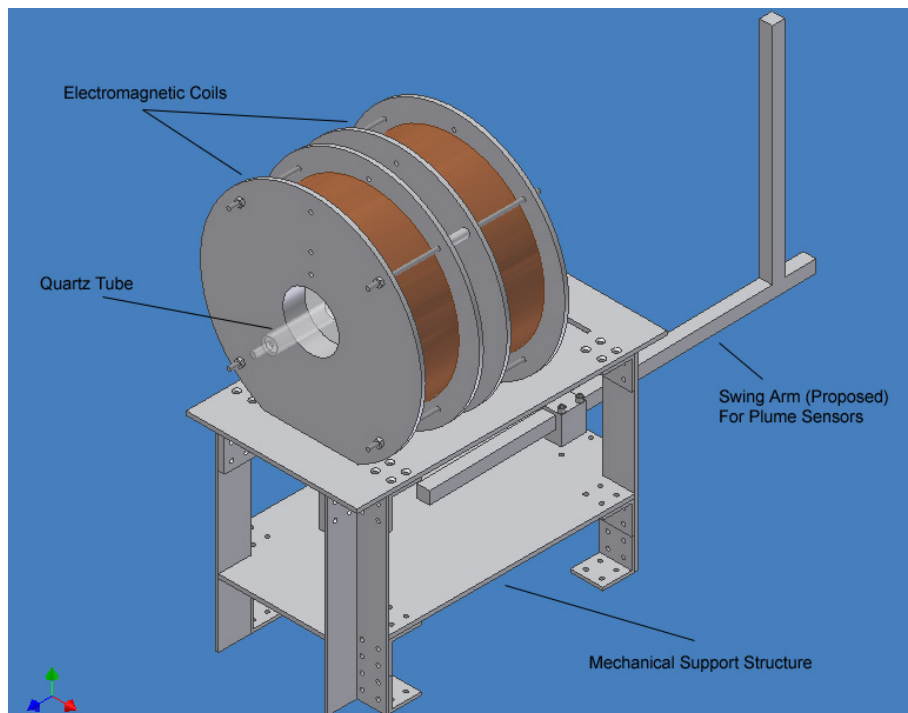


**Figure 5.2** CAD Rendering of Experiment Setup

1. All CAD designs included in this thesis have been rendered using this software package.

The proposed mechanical support structure consists of a number of components, as depicted in Figures 5.3 and 5.4 below. The four vertical legs of the structure are manufactured out of 3/16” thick angle aluminum, having a dimension of 2 inches per side. These legs are connected together by two aluminum plates, each 1/4” thick. The top plate is slotted, which provides resting locations for the electromagnetic coil bobbins.

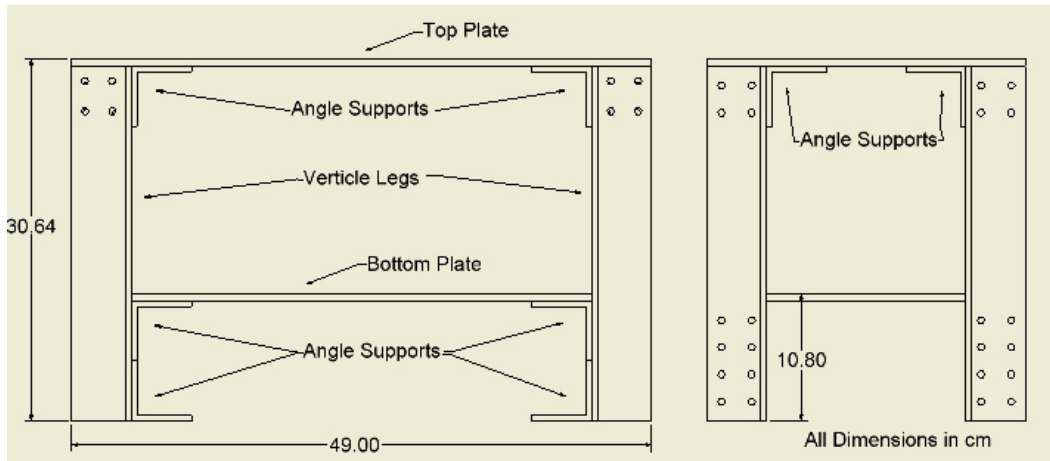


**Figure 5.3** CAD Rendering of Proposed Mechanical Support Structure, Side and Front Views

The four leg / two platform design is very stable. Notches in the bottom plate, which accept the vertical legs, help prevent the structure from distorting and add to this stability. Angle brackets reinforce each connection point, providing mating surfaces and further stability, as they force the interconnections to maintain perfect right angles. The structure components are assembled by 1/4 -20 bolts, nuts and lock washers. Each connection point provides four bolt locations which provide strong interconnections, and provide redundancy should individual bolts become loose.

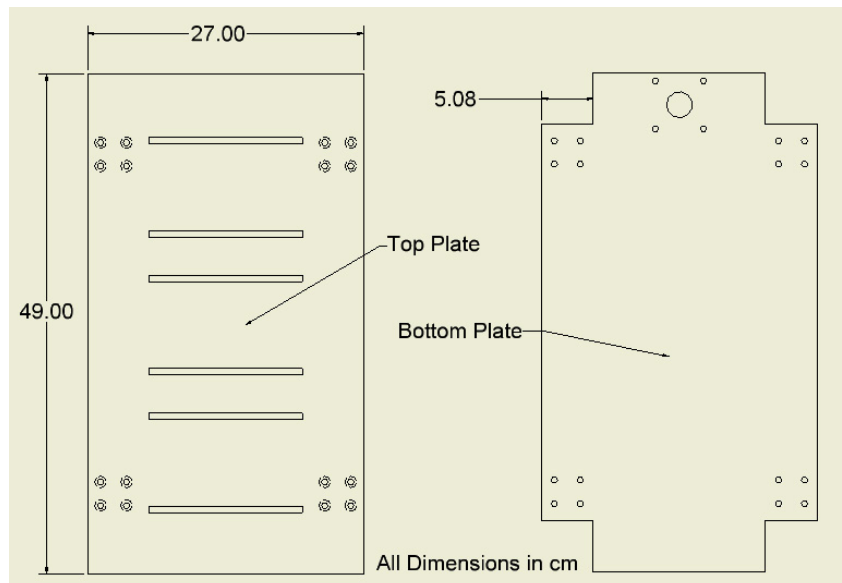


**Figure 5.4** CAD Rendering of Proposed Mechanical Support Structure Components, Top and Bottom Plates

The bolts which secure the top plate to the rest of the structure were countersunk. This provides for a smooth top surface, free of obstructions. This detail was important as it facilitated the installation and repositioning of the electromagnetic coils into their slot resting locations.

The lower platform provides a future mounting location for the proposed plume swing arm. This swing arm is depicted in Figure 5.2 above and Figure 5.5 below. By placing the pivot point of the arm in line with the vertical supports at one end of the mechanical structure, the arm - including necessary counterbalance, is provided a wide range of angular displacement.

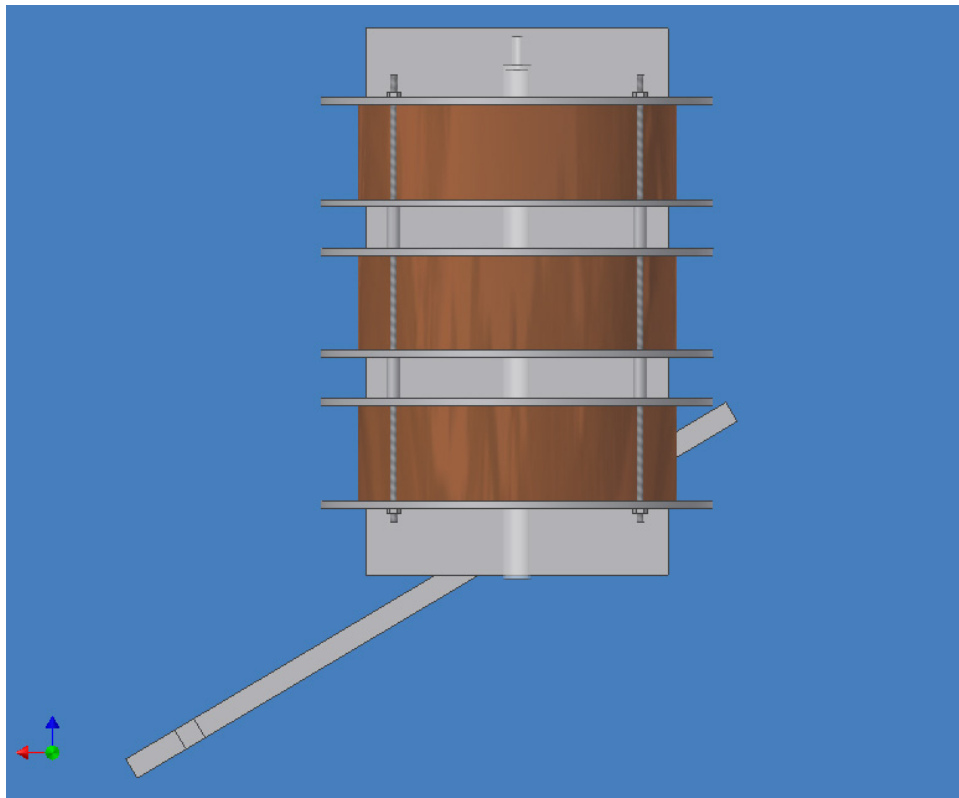


**Figure 5.5** CAD Rendering Showing the Proposed Plume Swing Arm in its Maximum Angular Displacement.

### **5.3 Design Modifications**

To further improve the capabilities of the mechanical support structure, an additional two cross beams were incorporated into the design. These beams were manufactured from 0.375 inch thick by 2 inch wide aluminum bar stock. The beams were located underneath the top plate, stretching lengthwise along the structure from one vertical support to another, as depicted in Figure 5.6 below. They replaced four angle brackets, which supported the top plate at its ends, but not in the middle. The replacement beams address this issue and transfer the load from the middle of the top plate to the vertical supports.

Dimensioned CAD drawings of these beams and of the other components which comprise the mechanical support structure are included in Appendix B.

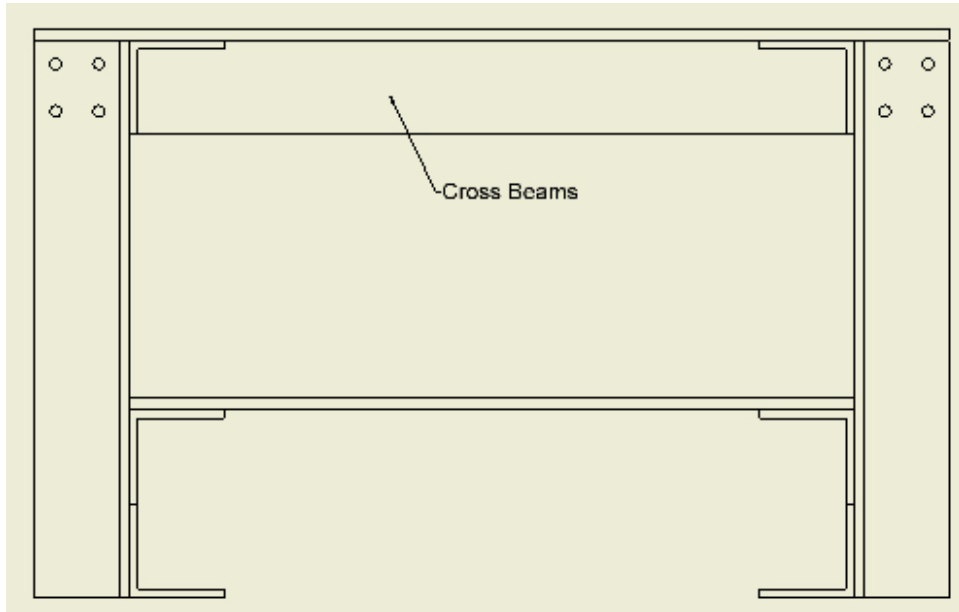


**Figure 5.6** CAD Rendering of Mechanical Support Structure, Side View. Additional Cross Beam Location Indicated.

## 5.4 Structural Analysis

A simple analysis of the proposed structure was undertaken to determine if it could support the load of the experimental setup. This load consists, for the purpose of calculation, of three coil / bobbin assemblies each weighing 60kg. It is desirable to provide at least 50% margin to account for variation in actual coil / bobbin masses and for other loading which may be imposed on the structure by the experimental setup. A model of the structure was utilized, which simplified the analysis while providing conservative results.

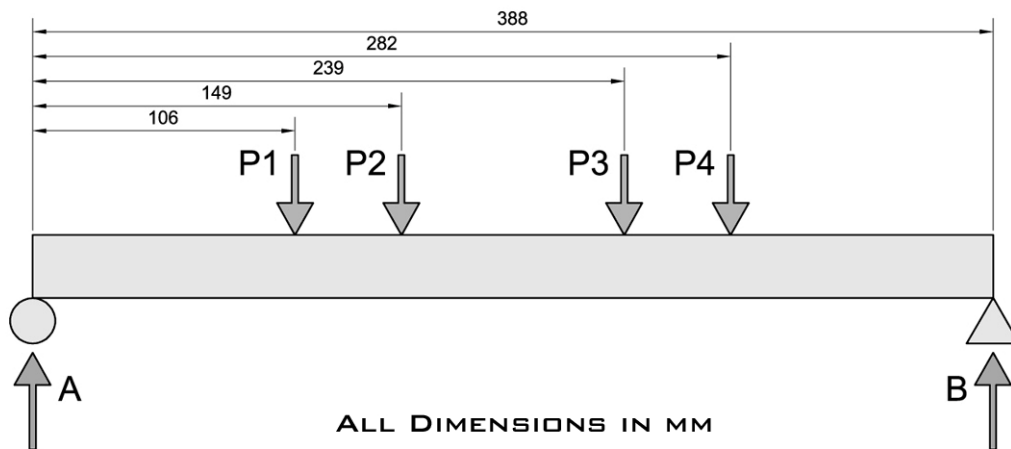


**Figure 5.7** Simplified Model of the Mechanical Support Structure

The simplified model of the experimental setup is presented in Figure 5.7 above. It was assumed that the entire load of the structure is carried by the two cross beams described in Section 5.3, thus conservatively ignoring the support capability of the top plate. Further it was assumed that the cross beams are simply supported. This assumption results in larger moments than the real situation and thus can be considered a conservative assumption.

The bobbins transfer the load of the electromagnetic coils to the mechanical support structure as what can be considered point loads. The outermost bobbin edges can be ignored, since they are in close proximity to the end of the beams and, therefore, do not contribute much to the beam moments. Each point load represents one quarter of the total weight of each coil. This is a result of the fact that each coil distributes its weight evenly on each of the ends of its bobbin, and that there are two cross beams in the structure which carry this load. Thus each point load can be considered equal to 15kg.

Point Load = 15kg

$$F = ma = (15\text{kg})(9.81\text{m/s}^2) \approx 150\text{N}$$

Thus we can see the reactions at A and B, i.e., the two frame uprights located at the ends of the beam, are 300N each.

The maximum moment in each of the beams is:

$$M = (150\text{N})(106\text{mm}) + (150\text{N})(149\text{mm}) = 38,250\text{Nmm} \approx 39\text{Nm}$$

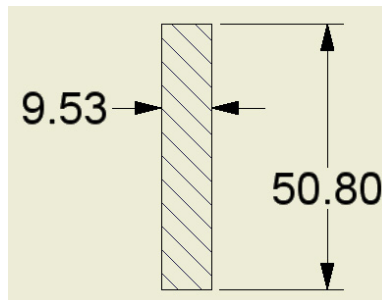


**Figure 5.8** Cross Section of the Support Beam, Dimensions in mm.

The moment of inertia of the beam's cross section can be calculated, using the dimensions illustrated in Figure 5.8 above.

$$I = \frac{bh^3}{12} = \frac{(9.53)(50.8^3)}{12} = 104,112\text{mm}^4 = 1.04 \times 10^{-7} \text{m}^4$$

Now we can calculate the highest stress in the beam.

$$f_{\text{max}} = \frac{Mc}{I},$$

where  $c$  is the distance from the central axis of the cross section to the extreme fiber. In this case,  $c = 50.8/2 = 25.4 \text{ mm} = 0.025\text{m}$   
So the maximum stress is:

$$f_{\max} = \frac{Mc}{I} = \frac{(39)(0.025)}{(1.04 \times 10^{-7})} = 9,375,000 \frac{N}{m^2}$$

This is equivalent to 9.5 MPa.

The aluminum used to construct the mechanical support structure consists of aluminum alloy 6061-T6511, which has a tensile strength of 35 KSI = 241 MPa [Alcoa, 2002]. This conservative analysis indicates significant margin, with the frame being capable of supporting up to 25 times the mass of the experimental apparatus.

## 5.5 Construction

With the design and analysis of the structure complete, the author proceeded to construct the mechanical support structure for use with the experimental setup. The aluminum angle was cut to appropriate lengths and holes were added, based on the dimensions provided by the design. The plates and cross beams were similarly prepared. The slots in the top plate were cut using a water jet machine<sup>1</sup> such that precisely dimensioned openings were obtained.

After assembling the structure components, the assembly was prepared for the vacuum chamber. This involved the use of a strong degreasing agent, followed by acetone to remove any residual cutting fluid or oils present. This was important so as to prevent volatiles outgassing from the structure surfaces, which would affect the pumping efficiency and vacuum chamber background pressure.

The structure was then installed within the SPL vacuum chamber. It was secured within the chamber to the preexisting metal grating by use of 3 inch long 1/4-20 bolts, wing nuts and fender washers. This method of installation provided quick and easy installation and repositioning of the structure within the chamber. The constructed mechanical support structure installed in the vacuum chamber is pictured in Figure 5.9 below. The final assembly proved to be both strong and stable.

---

1. Water jet cutting was performed by Adam Shabshelowitz.



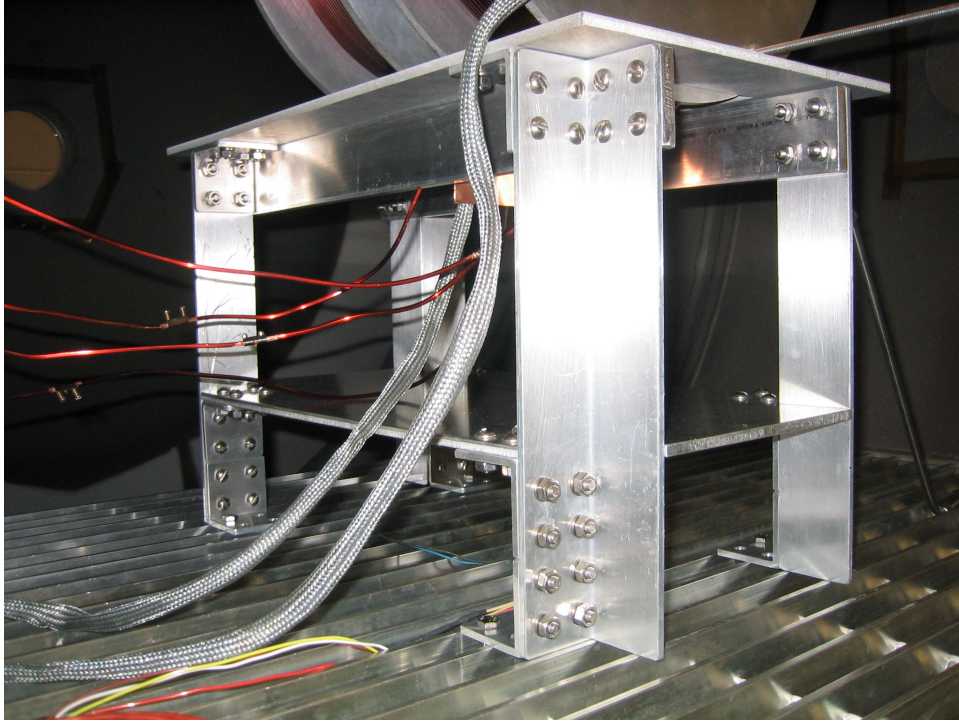


**Figure 5.9** Assembled Mechanical Support Structure, Installed in SPL Vacuum Chamber



# Chapter 6

## RADIO FREQUENCY POWER SYSTEM

The radio frequency power delivery subsystem of the mHTX@MIT is described in this chapter. The purpose of the system is to deliver RF Power to the helicon antenna, which is located at the heart of the experimental configuration. The system is comprised of a number of components, which are described here. Shielding and grounding considerations are explored, as such issues can play a critical role in the operation of RF systems. A matching network enclosure has been designed, constructed<sup>1</sup> and installed on the SPL vacuum chamber, and this effort is described. Finally, a matching network tuning procedure is discussed, by which matched or near matched impedance conditions can be achieved, which are required for optimal RF power delivery.

### 6.1 Description of Experimental Configuration

The radio frequency power delivery system of the mHTX@MIT is comprised of a number of components, which are depicted in Figure 6.1 below. Radio frequency power is provided by an RF Power Products RF-10S/PWT, 13.56 MHz generator. This rack-mounted unit is located near the experiment central control computer, where the front panel can be accessed by the experiment operator. The output of the generator is a standard RG10 connector, which is connected to a 50 ohm coaxial cable.

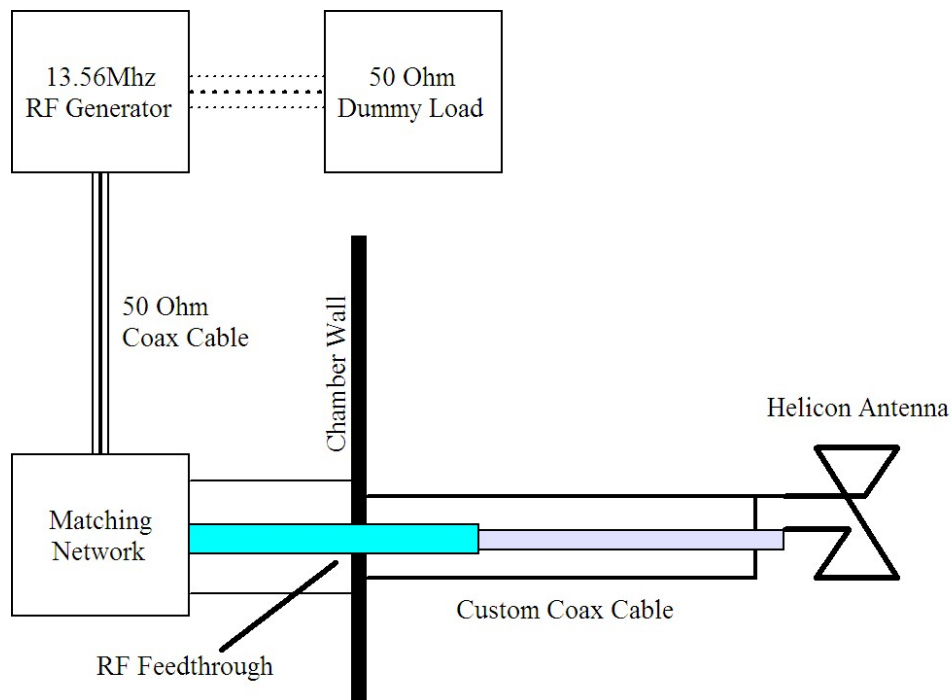


**Figure 6.1** RF Power Delivery Subsystem of the mHTX@MIT

1. The design and construction of this enclosure is one of the contributions of the author.

When testing the functionality of the RF generator, a 50 ohm dummy load can be connected to this coaxial cable. During normal operations, this dummy load is removed, and the 50 ohm coaxial cable connects to the matching network, which will be discussed in more detail in Section 6.3 below.

After the matching network, the RF signal passes through a vacuum RF feedthrough, and into the vacuum chamber. Within the chamber, a custom designed coaxial cable conducts the RF power through to the helicon antenna, which is located in the center of the experimental apparatus. This antenna couples with the gas flowing through the concentric quartz tube. Provided that an appropriate impedance match is achieved, a plasma is struck and RF power is delivered to this plasma.

The RF delivery system is deceptively simple from a component viewpoint. Due to the nature of RF energy, there are a number of considerations which must be taken into account in the design and construction of any RF system. Some of these considerations will be discussed in the next section.

## 6.2 Experiment Shielding and Grounding Considerations

Exposed RF conductors will radiate energy in all directions, causing disruption of other nearby electric circuits. Care must be taken to properly enclose all conductors which carry RF current with grounded surfaces. These ground surfaces will shield nearby conductors. Additional grounded shield may be required around nearby signal cables in order to prevent pickup of stray RF fields. Signal cables within the mHTX@MIT experiment have been covered with a grounded braid for this purpose, as shown in Figure 6.2 below for the thermocouple wires. Note that the washer in the foreground makes the electrical connection between the grounded chamber and the braid.

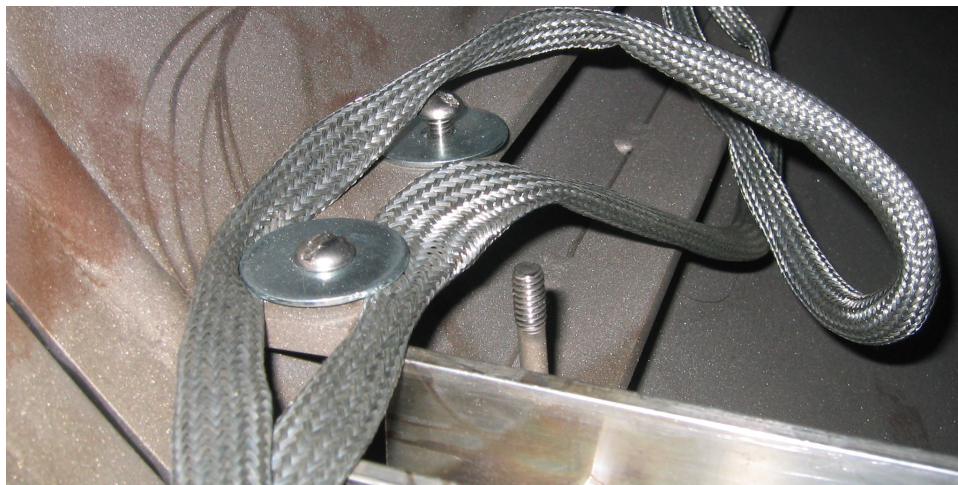


**Figure 6.2** RF Shielding Braid - Covering Thermocouple Wires.

The SPL vacuum chamber, which is constructed out of steel, acts itself as a grounding surface or Faraday cage. Stray RF fields from the experiment will impinge on the inner surface of the vacuum chamber. There they will induce surface currents. It is desirable to

shunt these surface currents to a solid earth ground, such that they do not build up and cause problems with chamber instrumentation and controls. Thus it was necessary to ground the vacuum chamber with a low impedance ground path. This has been accomplished through use of an 8 inch wide, 1 mm thick length of copper flashing<sup>1</sup> which is pictured in Figure 6.3 below.



**Figure 6.3** Low Impedance Chamber Grounding Strap

At 13.56MHz the skin depth, which is defined as the distance below the surface of a conductor where the current density has diminished to 1/e of its value at the surface, is found by:

$$\delta = (\lambda/\sigma.\pi.\mu.c)^{1/2}$$

Where:

$\lambda$  = wavelength = 22.12 meters

$1/\sigma$  = resistivity of copper =  $1.724 \times 10^{-8}$  ohm-meters

$\mu$  = the permeability constant. For copper, we assume it to be the same as that for free space =  $4 \pi \times 10^{-7}$  Henry/meter

$c$  = the speed of light in a vacuum =  $3 \times 10^8$  meters/second

Using these parameters, we obtain a skin depth at 13.56 MHz of  $\delta = 17.94\mu\text{m}$ . Thus we see that for practical purposes, all of the current flows in the surface of the copper strap. It is for this reason, that a thin, wide grounding strap is preferable to a wire conductor or narrower strap, which would have a smaller area for current to flow, and thus a higher impedance.

1. This copper flashing is widely available at home improvement stores, which is where the author obtained the material which he used for this connection, and for use in the matching network enclosure.



Care has been taken to remove the oxidation layer on the copper grounding bar (far left in Figure 6.3) which is present in the MIT Space Propulsion Laboratory, and to remove paint from the surface of the vacuum chamber. This ensures that good, low impedance electrical connections have been established.

The vacuum chamber viewing ports represent locations where there are holes in the Faraday cage. At these locations, RF energy will leave the chamber, potentially affecting instrumentation and controls throughout the Space Propulsion Lab. To address this concern, metal mesh was installed over these portals, as pictured in Figure 6.4 below.

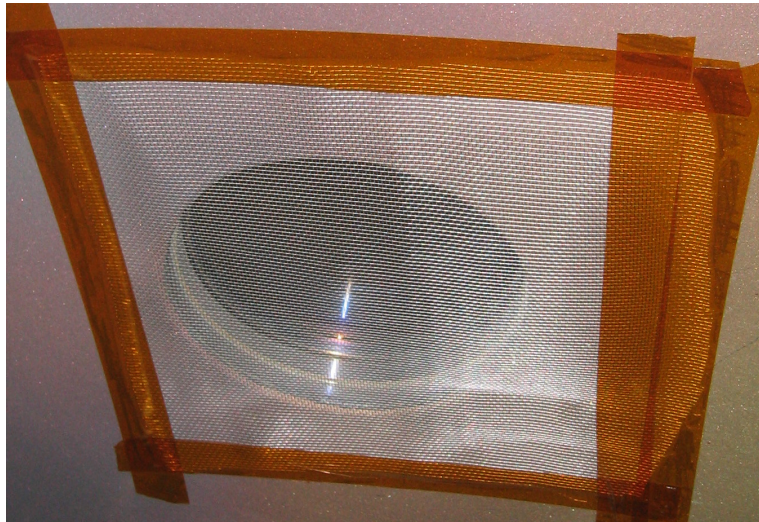


**Figure 6.4** RF Shielding Mesh, Placed Over Chamber View Ports

An additional concern regarding RF power systems is the importance of ground loops avoidance. Ground loops can cause a host of problems, from inaccurate delivered power measurement to mysterious instrumentation and controls failures. It is relatively straightforward to prevent these ground loops from occurring, provided this constraint is taken into account during the design of the experimental apparatus. In the present case, care has been taken such that the ground return path from the helicon antenna remains isolated from other grounded structures until the coaxial cable interfaces with the chamber wall. If the return current, which flows along the outer conductor of this coaxial cable, is not equal to the supply current, theory indicates that electromagnetic fields will be present outside the coax. This is undesirable because these stray fields will again be picked up by nearby instrumentation and controls.

## 6.3 Matching Network Enclosure

A critical component of the RF power delivery subsystem is the matching network. This network has been designed<sup>1</sup> to provide an impedance match between the antenna / plasma load and the 50 ohm output impedance of the RF generator. The matching circuit that is utilized in the mHTX@MIT experiment is represented schematically in Figure 6.5. It consists of two variable capacitors. The first, C1, is located in series with the RF load, while C2 is shunted to ground.

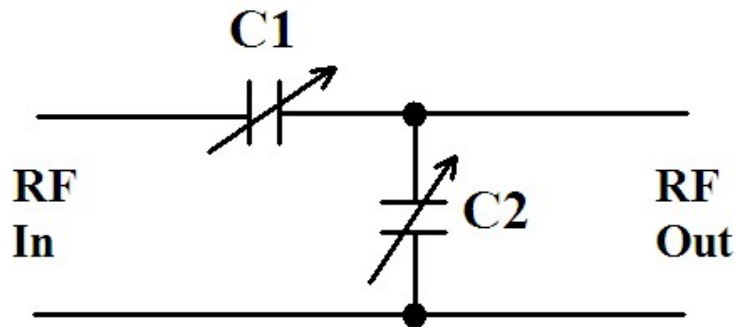


**Figure 6.5** Basic Impedance Matching Circuit.

The design and construction of a suitable mounting system and enclosure for this circuit represents a nontrivial effort, which comprises one of the contributions of this author. Autodesk Inventor 7.0 software was utilized to create a 3D CAD model of the proposed enclosure. Renderings of this model are presented in Figures 6.6 and 6.7 below.

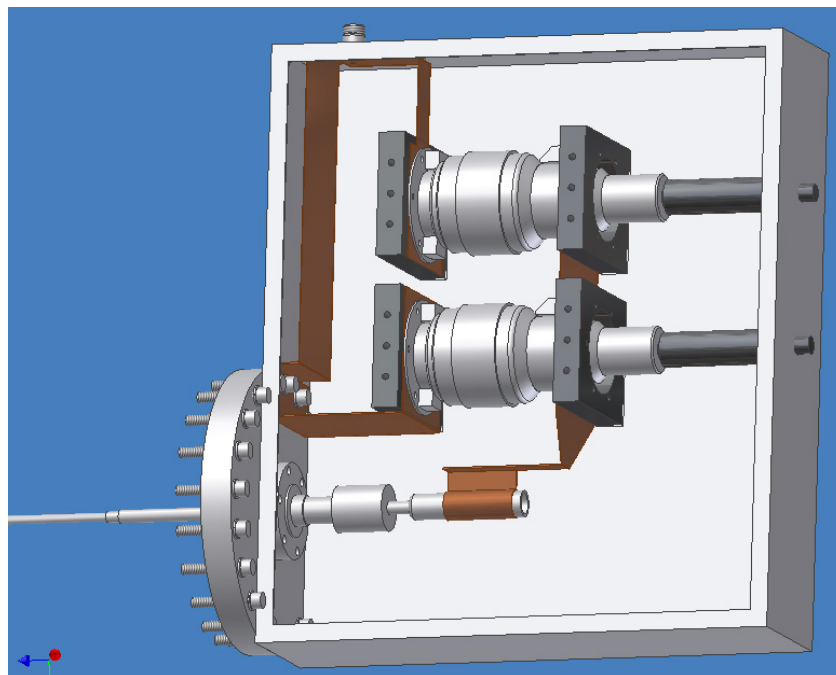


**Figure 6.6** CAD Rendering of Matching Network.

1. Matching network circuit design and calculations were performed by Justin Pucci. Physical design and construction performed by this author.

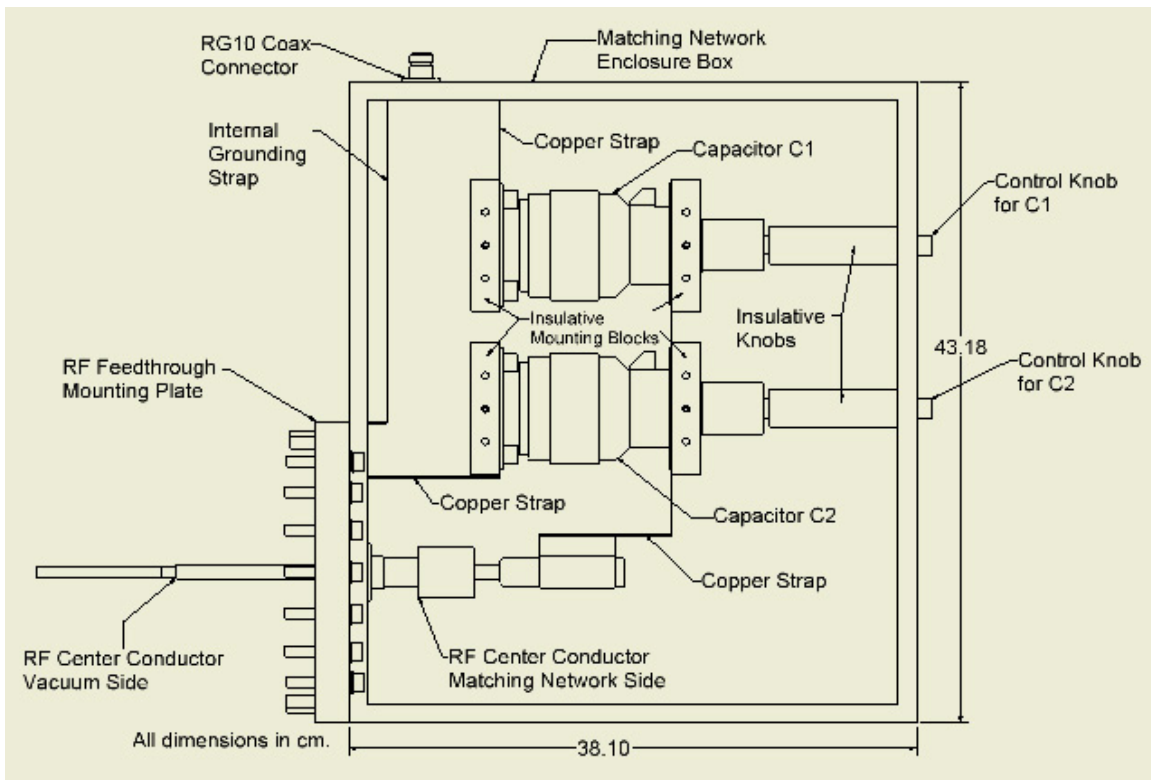


**Figure 6.7** CAD Diagram of Matching Network with Labeled Components.

The matching network circuit calls for the use of variable capacitors. It is desirable to use variable capacitors instead of fixed value capacitors in this application for two primary reasons. First, it is very difficult to take into account parasitic impedances in the RF system. These parasitic impedances alter the capacitance values required to achieve load / generator impedance matching from calculated design values. Second, it is difficult to accurately predict the impedance of the plasma load, and this value can change depending upon propellant gas used, propellant flow rate, and applied magnetic field. Thus the capability to modify these capacitor values before and during experiment operation is required. Preliminary values for these capacitors were calculated in order to size the variable capacitors needed, with C1~17pF and C2~360pF.

Variable capacitors were obtained from Jennings Technology Inc. These particular capacitors represented a unique design challenge for implementation in the matching network. The mounting surfaces for these capacitors serve dual purpose, as they are also the electrical connections to the capacitor. Additionally, the adjustment knob which is used to vary the capacitance value is metallic, and is electrically connected to one of the capacitor leads. Thus the design of the matching network enclosure required both insulated mounting locations for the capacitors, as well as insulated extensions to the control knobs.

Several additional factors had to be considered in the course of matching network enclosure design and construction. Due to the previously mentioned low thickness skin

depth at 13.56MHz, it was desirable to make use of wide copper straps for connecting together different circuit elements. One millimeter thick copper flashing was used to provide these wide, thin, strap connections. An additional concern was to minimize or remove sharp metallic points and edges. It is well known that high electric fields are developed at such locations. These tend to be locations where arcing and surface tracking can occur, and thus these conditions were avoided.

The components of the matching network were arranged within a metallic enclosure, which takes the form of a 38 cm by 43cm by 10cm wide aluminum box. This enclosure provides the mechanical backbone support for the matching network system. It mounts directly to the 8 inch vacuum access port, with the RF feedthrough passing directly into the enclosure. Mounting takes place utilizing the same mounting bolts as those used for the access port. These bolts, and the metal/metal surface contact between the matching network enclosure and the vacuum access port provide a solid electrical connection with the well grounded vacuum chamber. Thus the matching network enclosure serves as a Faraday cage, containing RF fields generated within.

The RF signal is conducted from the generator, through the 50 ohm coax cable, to a RG 10 connector which is located at the top of the matching network enclosure. A copper strap conducts the RF current to the series capacitor, C1. The opposite terminal of C1 is connect to a common node point. From this common node point capacitor C2 is shunted to ground, and the RF is also conducted via another copper strap to the RF feedthrough and into the vacuum chamber.

Return current passes through the vacuum access port mating surface and into the matching network. A separate copper ground strap directs this return current within the matching network enclosure to the RG10 coax connector, from where it returns to the RF generator. This wide copper strap presents a lower impedance to the return RF current than the surface of the aluminum matching network enclosure. Inclusion of this strap into the matching network design was important, as surface currents that would otherwise develop on the enclosure could pose a safety risk and could result in RF radiation external to the enclosure.

Dimensioned CAD drawings of the components which comprise the matching network enclosure are included in Appendix B. These CAD drawings were utilized by the author to machine and assemble the components of the matching network. The mounting blocks and control knob extensions were manufactured from G10 plastic block and rod, respectively. The completed assembly, attached to the side of the SPL vacuum chamber is pictured in Figure 6.8 below.

## **6.4 Network Tuning Procedure**

Having completed the design, assembly and installation of the matching network, a procedure was developed to tune the network for optimal RF power delivery. Initially, a Tektronix P6015A high voltage oscilloscope probe was used to observe the voltage waveform present on the RF vacuum feedthrough. It was found that in well matched

conditions the voltage waveform reached a peak to peak value of approximately 4kV. By adjusting the values of C1 and C2 to maximize this voltage, matched conditions were obtained.

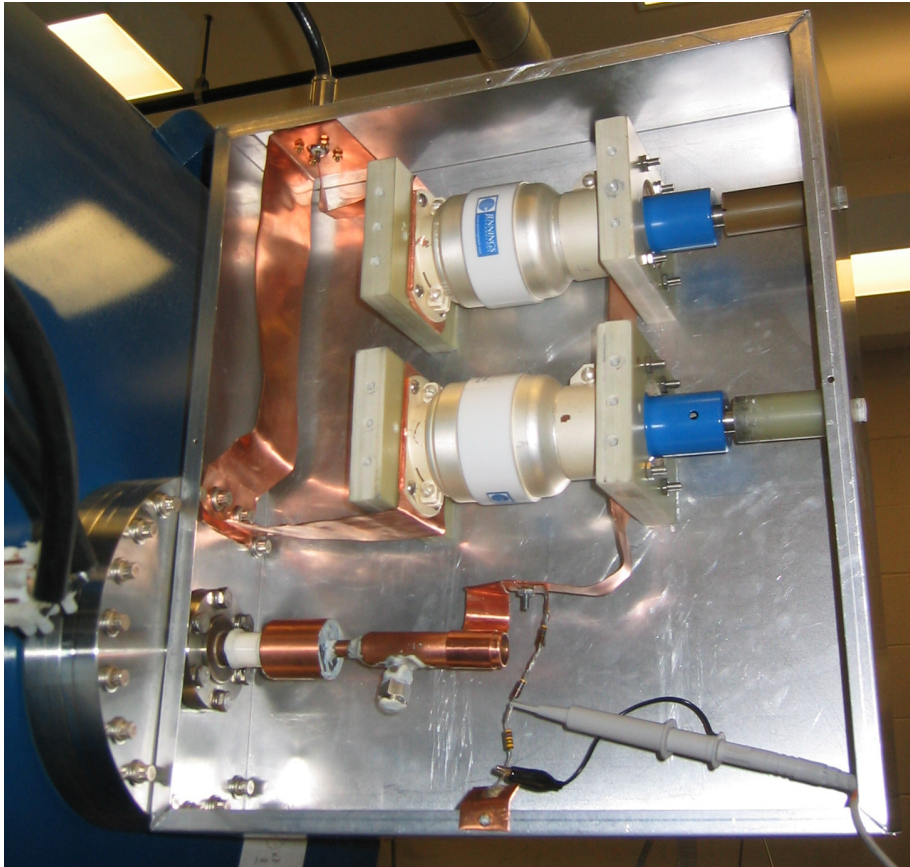


**Figure 6.8** Matching Network Mounted to the SPL Vacuum Chamber

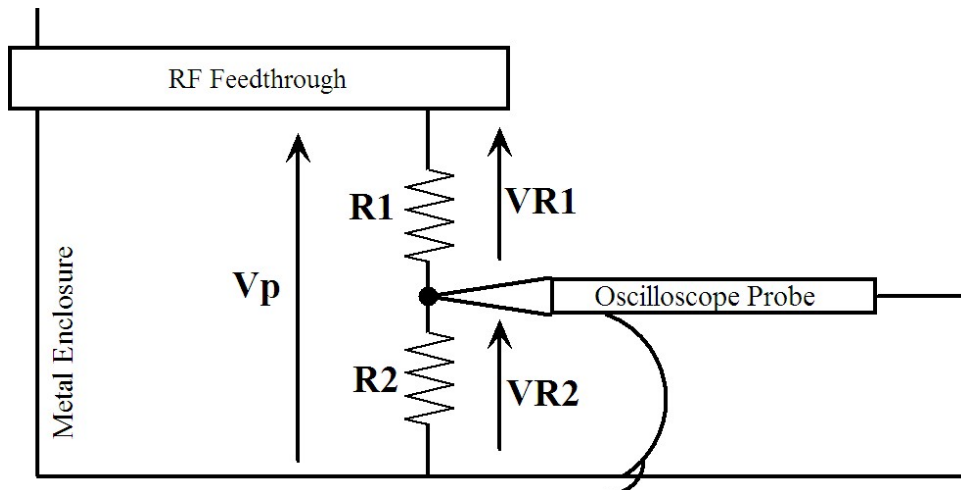


**Figure 6.9** Resistive Divider Used During Network Tuning

The P6015A is a large probe, and its presence, while helpful for obtaining matched conditions, prevented installation of the metallic covering for the matching network



enclosure. This resulted in the radiation of radio frequency energy into the Space Propulsion Laboratory. It was desirable to make use of a less unwieldy probe which would allow installation of the matching network cover. In order to accomplish this, a resistive divider was installed within the matching network enclosure, and an Agilent 10076A oscilloscope probe was utilized. This is a 100:1 probe, which operates to a maximum input voltage of 2kVpk-pk. A schematic diagram of this arrangement is shown in Figure 6.9, and pictured in the lower right of Figure 6.8 above. Note that this quick solution will be replaced at a later date with a shielded circuit which outputs a DC value proportional to the RF amplitude.

An HP 54601A 100MHz oscilloscope was used to make measurements in the matching network. The maximum input voltage of this oscilloscope is 400V. It was assumed that the voltage present on the RF feedthrough,  $V_p$  in Figure 6.9, could potentially reach a maximum value of 5kVpk-pk. The author selected a 10:1 divider, giving a maximum node voltage (between the resistors) of 500Vpk-pk. It is at this node that the oscilloscope probe is applied, and this voltage is well within the 2kVpk-pk operating limit. This also results in a maximum voltage of 5Vpk-pk applied to the oscilloscope input, well within its limits.

The selection of a 10:1 resistive divider stipulates:  $R_1 = 10R_2$

4.5M ohm  $\frac{1}{4}$  watt and 450k ohm  $\frac{1}{4}$  watt resistors were available in the lab. Calculation was performed to determine if these resistors would be sufficient for use in this resistive divider. Having selected then  $R_1 = 4.5Mohm$  and  $R_2 = 450kohm$

$$R_1 + R_2 \approx 5Mohm$$

It is assumed  $V_p = 5kV_{pk-pk} \sim 2kV_{rms}$

$$\frac{V}{R} = I = \frac{2kV}{5M} = \frac{2 \times 10^3}{5 \times 10^6} = 0.5mA$$

For  $R_1$ ,

$$P_{R1} = IV = (0.5m)V_{R1} = (0.5m)(2k) = 1W$$

For  $R_2$ ,

$$V_{R2} = 500V_{pk-pk} \sim 176V_{rms}$$

$$P_{R2} = IV = (0.5m)V_{R2} = (0.5m)(0.2k) = 0.1W$$

Thus a single 450kohm  $\frac{1}{4}$  watt resistor was used for  $R_2$ . Four 4.5Mohm resistors were used in the place of  $R_1$ . They were placed, two in parallel, in series with an additional two in parallel. This resulted in the rated  $\frac{1}{4}$  watt of total dissipation in each resistor in this worst case scenario.



# Chapter 7

## PRELIMINARY RESULTS

The experimental setup as described in this thesis has been assembled and tested, and is now operational in the MIT Space Propulsion Laboratory. Pictures of the completed apparatus are presented here to further illustrate the experiment design and construction. Early test operations of the thruster were performed, with variation of propellant gas, propellant flow rate, applied RF power and applied axial magnetic field. Some initial data was collected, including pictures of plasmas generated by the experiment in a number of distinct operating regimes. Full characterization of the operational experiment will be left for future investigation.

### 7.1 Completed Experimental Assembly

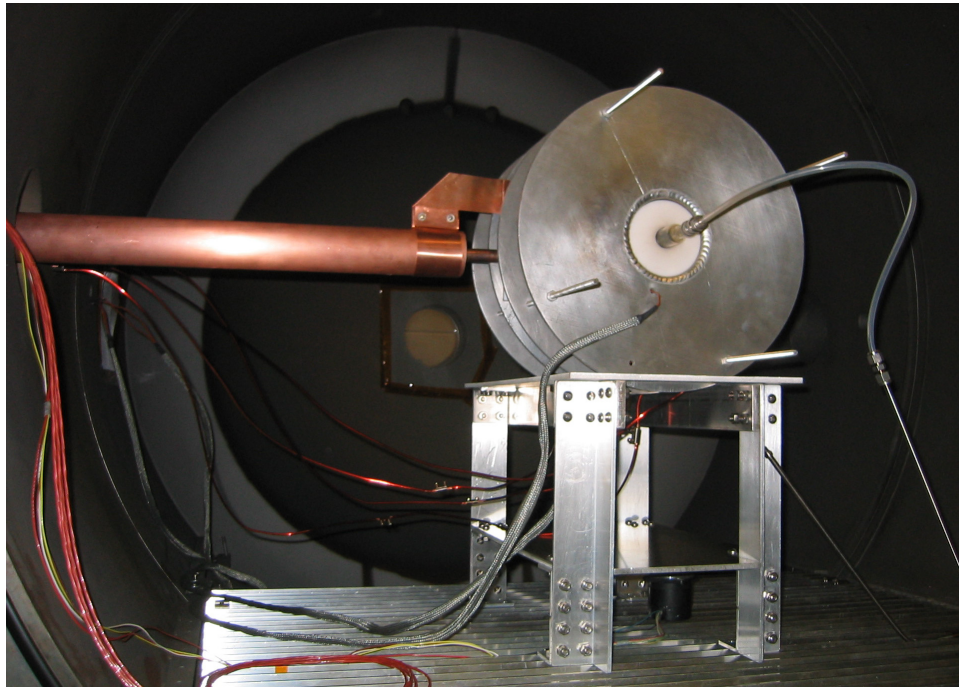


**Figure 7.1** Experimental Apparatus of the mHTX@MIT.

The core elements of the mHTX@MIT experimental setup, as installed within the MIT SPL vacuum chamber, are pictured above in Figure 7.1. The electromagnetic coil bobbin assemblies are located near the center of the vacuum chamber. This placement aligns the quartz tube with the view ports at the back, front and side of the chamber. This facilitates operator observation of the produced plasma and plume. The back view port is visible in Figure 7.1, just to the lower left of the coil bobbins.

Additional components and connections can be observed in Figure 7.1. The four threaded tie rods which connect together the two coil bobbins are shown. The coils bobbins are

supported by the mechanical support structure, which is secured to the metal grating within the chamber. The custom coaxial cable can be seen extending to the left in Figure 7.1, where it interfaces with the RF feedthrough (just out of the image). Shielded thermocouple cables are shown leading from the coil bobbins left to the electrical feedthrough, as are the electromagnet current supply wires. The quartz tube and Teflon spacer are shown within the coil bobbins. The quartz tube is connected via a metallic Swagelock connector to a short length of plastic tubing, which is then connected to stainless steel tubing, which extends out of the image and connects to the gas feedthrough.

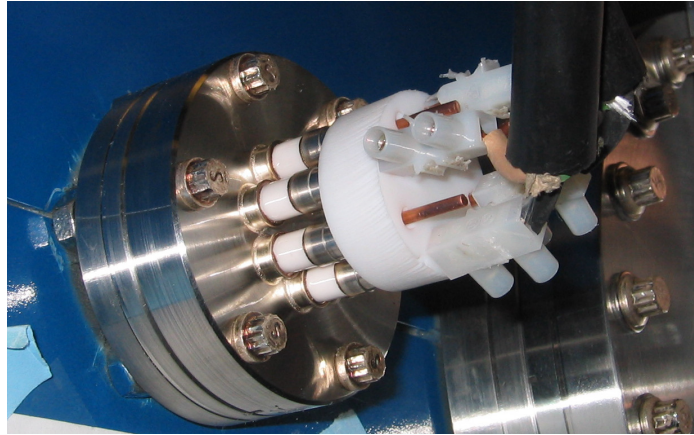


**Figure 7.2** Electrical Feedthrough for Electromagnet Power Supply.

The high current electrical feedthrough is pictured in Figure 7.2 above<sup>1</sup>. As described in Section 3.1.4, this feedthrough provides connections between the electromagnetic coils and their DC power supplies. These two power supplies, each an HP model 6479, are pictured in Figure 7.3. They can each provide between 0 and 300V and 0 and 35A.



**Figure 7.3** Electromagnet DC Power Supplies.

<sup>1</sup>. Installation of both electrical feedthroughs and their connections were completed by Nareg Sinenian.





**Figure 7.4** Electrical Feedthrough for Various Sensors.

Another electrical feedthrough is pictured in Figure 7.4 above. This feedthrough is used to connect the thermocouples to the central control computer. Future instrumentation and controls will utilize this feedthrough, as discussed in Section 3.1.5.

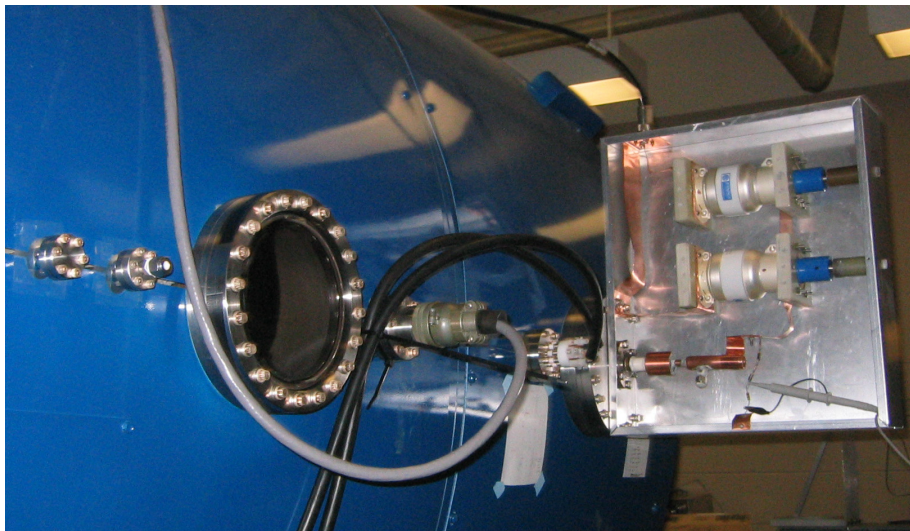


**Figure 7.5** Side of SPL Vacuum Chamber – Showing Matching Network, Electromagnet Power Supply Feedthrough and Sensor Feedthrough.

The side of the SPL vacuum chamber is pictured in Figure 7.5 above. Visible is one of the chamber side view ports. Beyond that view port is the electrical feedthrough, with a multiconductor cable shown passing over the vacuum chamber to the central control computer beyond. The next feedthrough is the high current electrical feedthrough, with

two, three conductor (power, return, and ground) cables running down to the electromagnet DC power supplies. Beyond that feedthrough is the matching network, which is mounted to the chamber access port. A flange reduces the port from 8" to a smaller diameter to accommodate the RF vacuum feedthrough. The 50 ohm coaxial cable is shown connected to the RG10 connector on the top of the matching network, and it stretches above the vacuum chamber and over to the rack mounted RF generator. Finally, the resistive divider and oscilloscope probe are shown. The probe is connected to an oscilloscope located beyond this image.

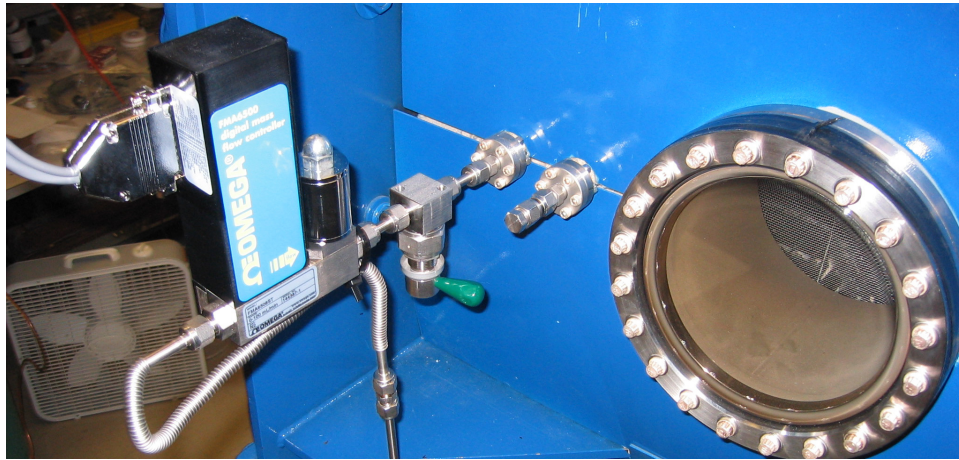


**Figure 7.6** Gas Flow System, Including Mass Flow Controller.

The opposing side of the SPL vacuum chamber is shown in Figure 7.6 above. This image includes another side view port, as well as some of the gas flow system, which is described in detail in Section 3.1.2. Shown are the mass flow controller, with interface cable leading to the central control computer, and the manual cutoff valve located between the flow controller and the gas vacuum feedthrough. The second gas vacuum feedthrough shown is unused in the present experimental setup.

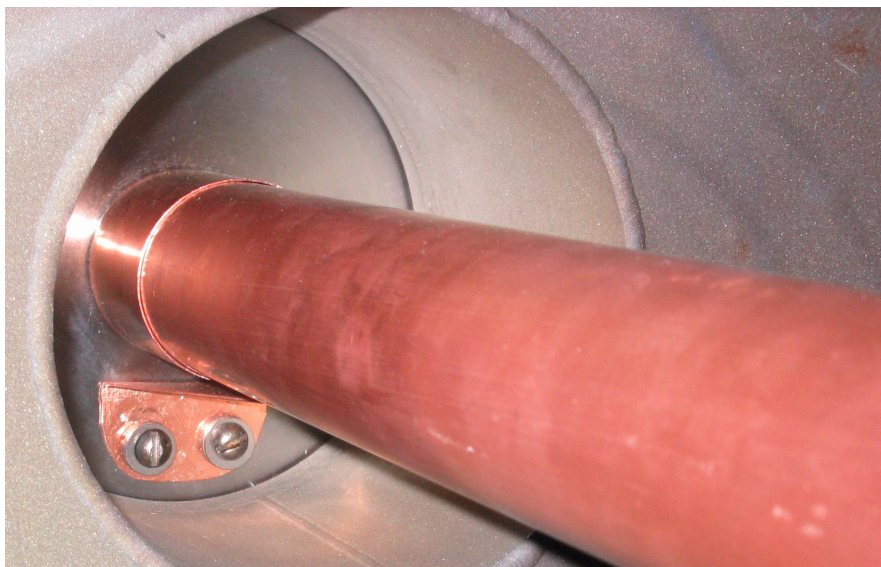


**Figure 7.7** Custom Coaxial Cable, Connected to 8 Inch Reducing Flange.



Within the vacuum chamber, a custom coaxial connection has been created. A ½ inch diameter copper water pipe serves as the center conductor, with a return shield conductor surrounding it. This return shield conductor consists of a 2 inch diameter copper water pipe<sup>1</sup>. The gap between the two conductors is a vacuum, with the exception of two thin Teflon blocks. These blocks serve to keep the two pipes concentric. They are located near the two ends of the custom coax, one of which is visible in Figure 7.8 below.

Return current flows from the helicon antenna through the outer conductor of the custom coax within the chamber, and passes into the matching network through the chamber wall. This is accomplished via an electrical connection made right at the RF feedthrough. The connection consists of a conductive strap which is manufactured from 1mm thick copper flashing. This strap wraps around the 2 inch diameter pipe, providing a large surface to surface contact for a low impedance connection. The strap is bolted to the vacuum port 8 inch reducing flange via a tapped hole which was added for this purpose. This connection is important as it provides a direct return current path, and prevents large return currents from flowing on the chamber surface.

Similar low impedance strap connections are made between the opposite end of the custom coax and the helicon antenna. The return current strap is visible in Figure 7.8 below. Care is taken to prevent this strap from coming in contact with other grounded conductors, such as the surface of the coil bobbin assemblies. Such contact would result in a division of return current between multiple paths, forming ground loops, as described in Section 6.2.

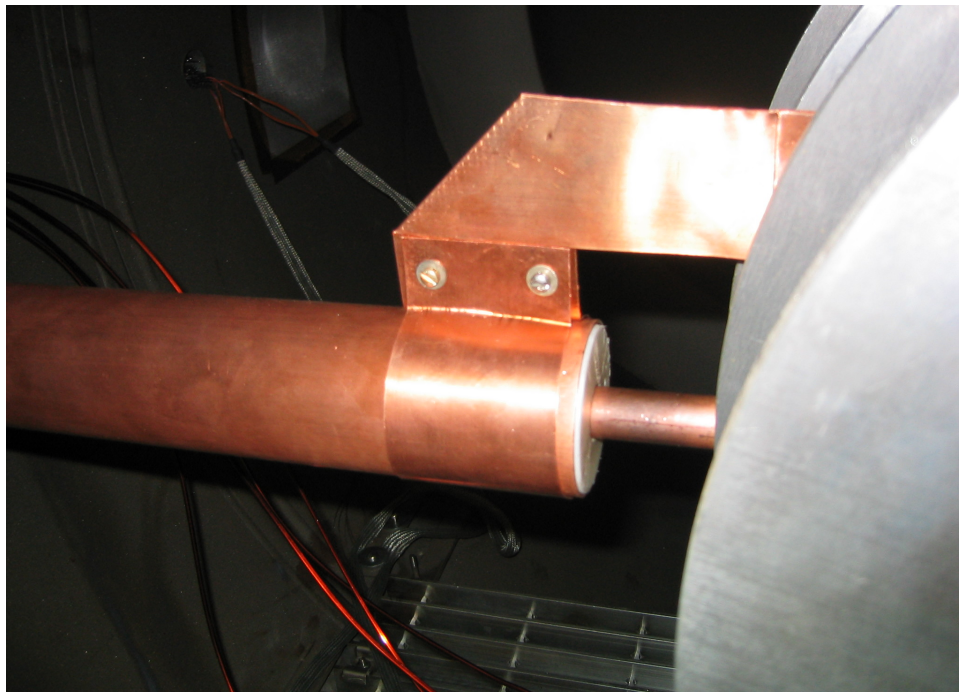


**Figure 7.8** Coaxial RF Connection with Ground Strap and Teflon Gap Spacer Shown.

1. Both the ½ inch and 2 inch copper water pipe were obtained at the local home improvement store.

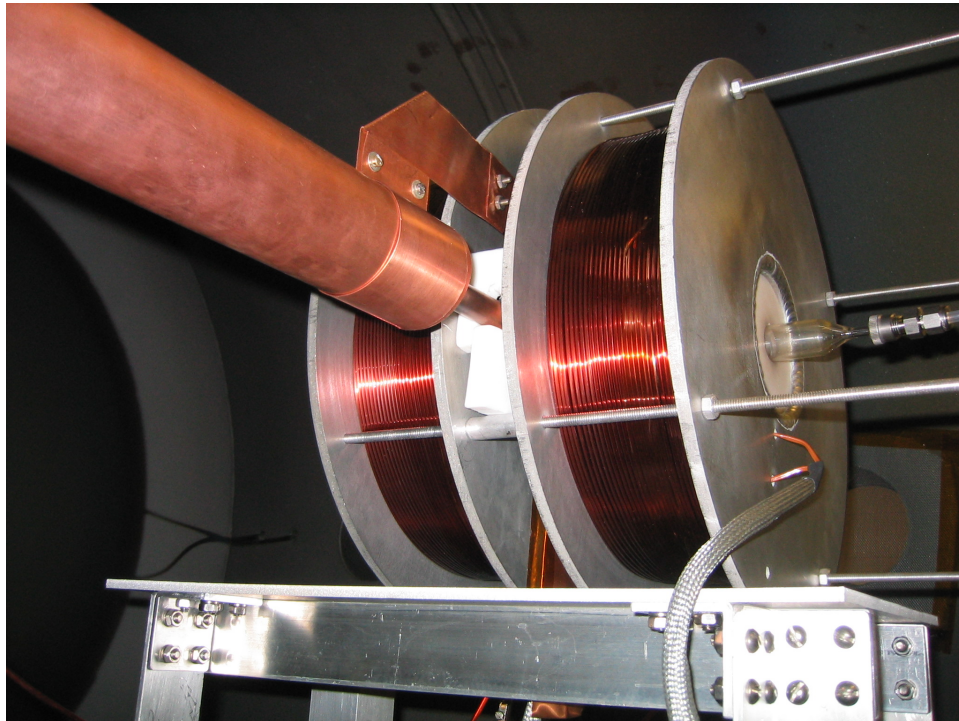


**Figure 7.9** Coaxial RF Connection with Ground Strap and Teflon Spacers.

Additional Teflon spacers were installed between the center conductor of the custom coax cable and the coil bobbins. These ensured that no contact took place between the center conductor, which carries RF current, and the grounded coil bobbins. These Teflon spacers are the white blocks visible in Figure 7.9 above.



**Figure 7.10** Copper RH Helical Antenna, With Tape Measure for Scale.

The helicon antenna was manufactured from a length of  $\frac{1}{2}$  inch diameter copper water pipe, through use of a hand held rotary tool.<sup>1</sup> The antenna, pictured in Figure 7.10 above, is approximately 4 inches in length. Straps between the custom coaxial cable and the antenna are installed using mounting holes drilled in two of the arms of the antenna. These holes are visible in the above Figure 7.10.

<sup>1</sup>. The design and construction of the helicon antenna was completed by Justin Pucci.



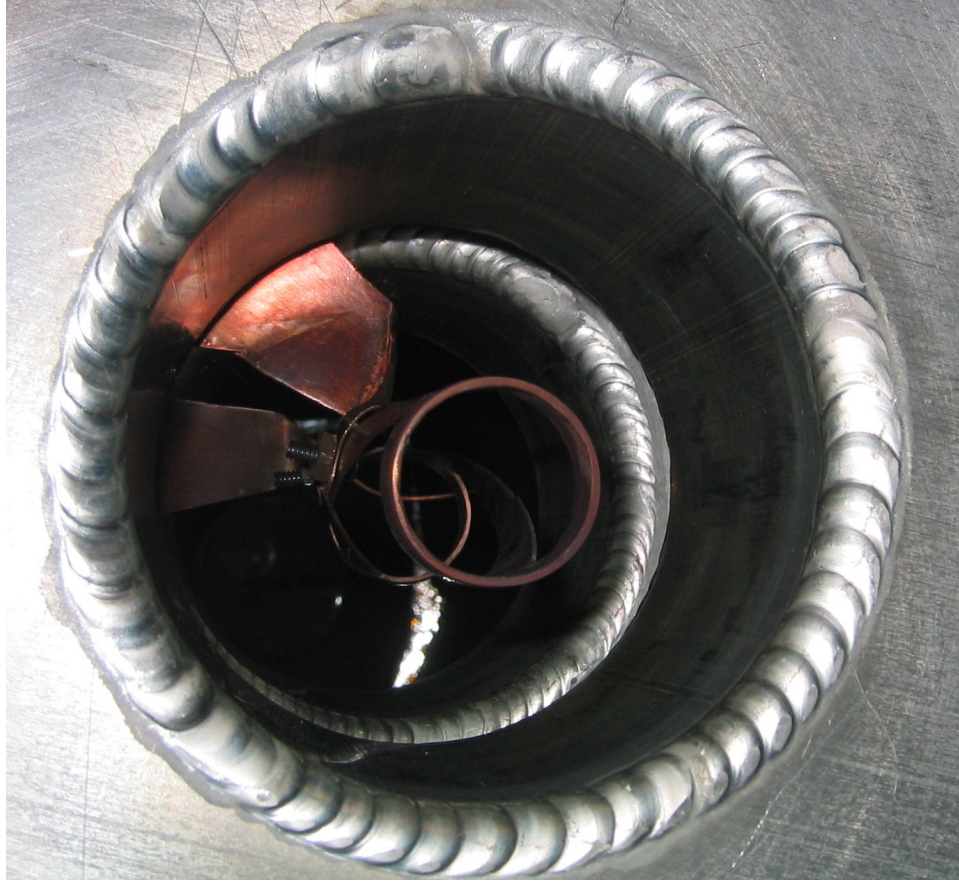


**Figure 7.11** Helicon Antenna Installed in Experimental Setup.

The helicon antenna, as installed within the experimental apparatus, is pictured in Figures 7.11 and 7.12. In Figure 7.11, the Teflon support blocks and quartz tube have been removed for this image in order to allow observation of the antenna in its installed location. Copper straps can be seen leading from the antenna between the two coil bobbins, where they then connect to the custom coax cable.

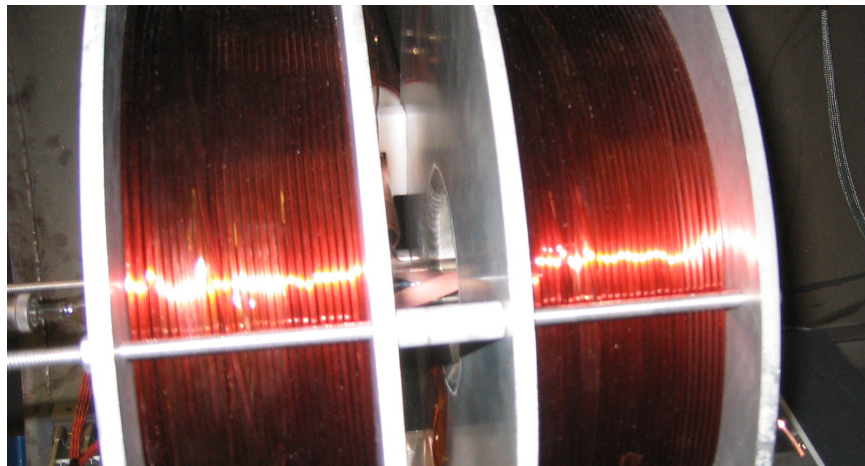


**Figure 7.12** Helmholtz Pair of Electromagnetic Coils, With Quartz Tube and Helicon Antenna Visible Along Their Axis.



An additional view of the completely assembled and operational mHTX@MIT experimental setup is provided in Figure 7.13 below.

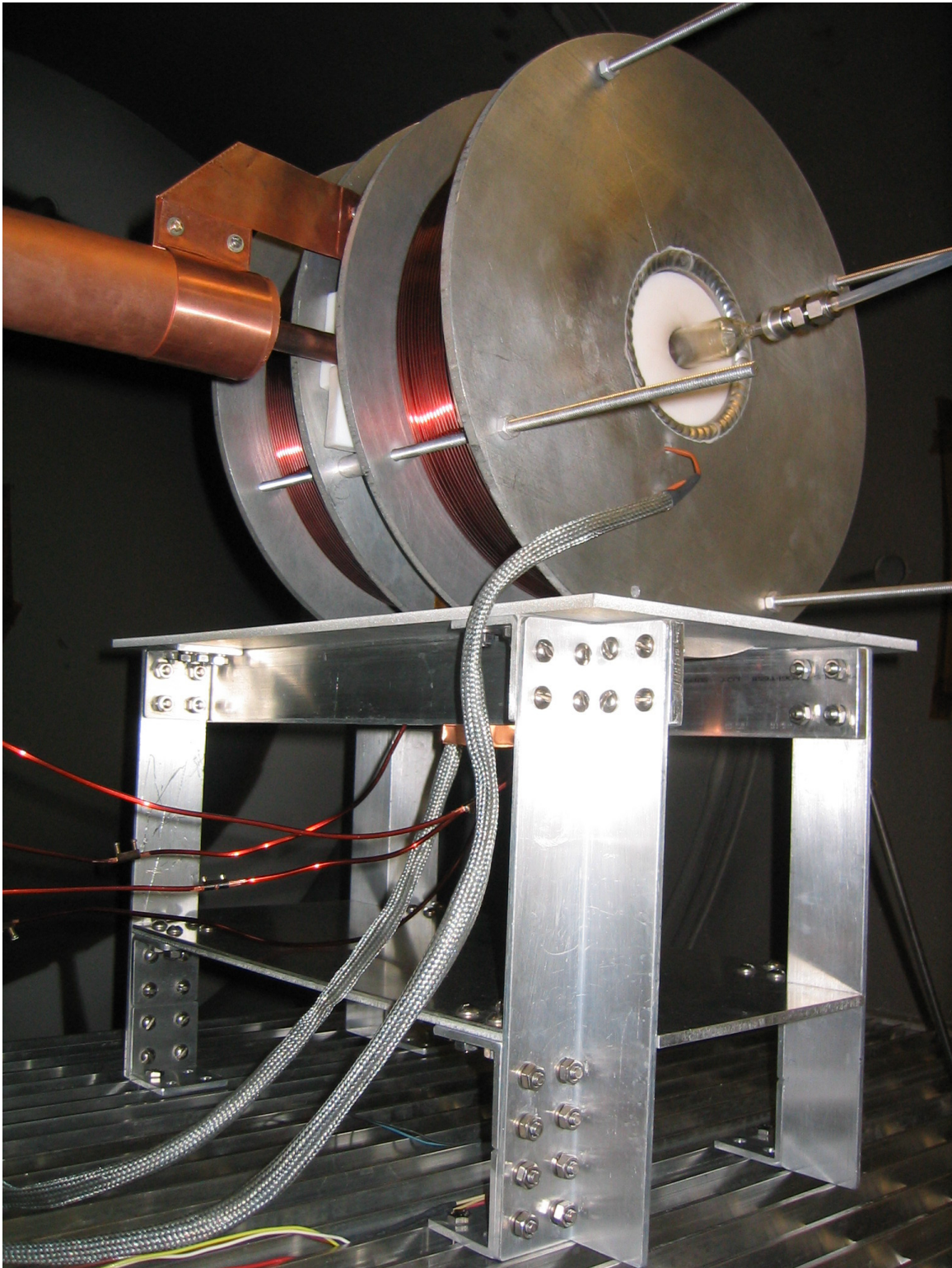


**Figure 7.13** Experimental Apparatus of the mHTX@MIT.

## 7.2 Early Plasmas in Various Operating Regimes

First plasma was obtained in the experimental setup of the mHTX@MIT at 9:19 PM EST, November 23<sup>rd</sup>, 2005. A nitrogen gas flow of 10 sccm was supplied to the device, and no magnetic field was applied. The matching network was adjusted until a power level of 40W was delivered, as indicated by the RF generator front panel display. The plasma generated is pictured in Figures 7.14 and 7.15 below. Due to the lack of an applied magnetic field and the low delivered power, this discharge is known as an ICP or inductively coupled plasma.



**Figure 7.14** First Plasma of the mHTX@MIT, as Viewed from the Chamber Side View Port. 40W, N<sub>2</sub>, 10 sccm, ICP

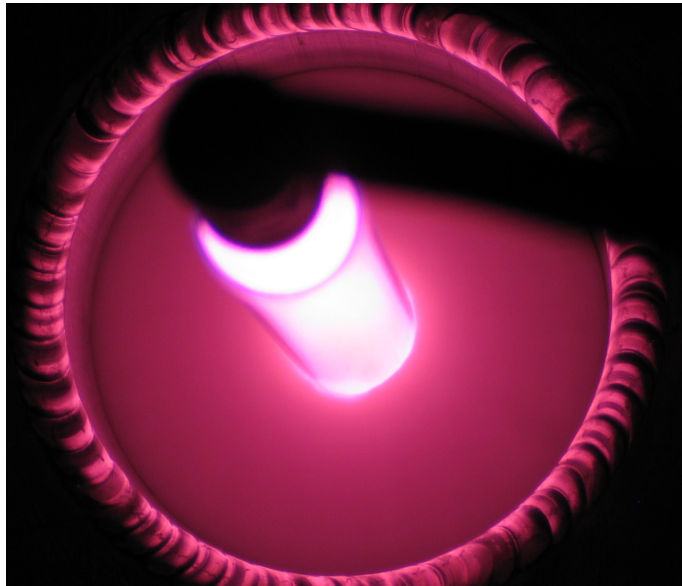


**Figure 7.15** First Plasma, as Viewed from the Chamber End View Port. 40W, N<sub>2</sub>, 10 sccm, ICP

By obtaining the plasma pictured above in Figure 7.14 and 7.15, minimal operational capability of the experimental apparatus was verified. It was evident that the various subsystems were working sufficiently to initiate and sustain a plasma discharge. However, some difficulty was experienced when attempting to increase the delivered power above 40W. The RF generator has a built in safety feature which limits the amount of reflected power, that is power which is returned to the generator due to an impedance mismatch, to a value of no more than 50W. If this limit is reached, the power output of the generator is reduced. In the first plasma obtained on November 23<sup>rd</sup>, this phenomenon had occurred, and no higher power levels were obtained.

The initial connection between the RF feedthrough and the helicon antenna was achieved through use of a standard RG10 coaxial cable. Upon inspection of this cable following the initial operation of the experiment, some melting of the insulative covering on the cable was observed. Cutting open the cable revealed a migration of the center conductor within the cross section, bringing it closer to the outer conductor, nearly to the point of creating a short circuit. The assumption is that this cable, which is designed for use in open atmosphere, overheated in the vacuum chamber, where convection was no longer a mechanism by which excess thermal energy could be dissipated. Thus the insulator between the center and outer conductors became pliable, resulting in center conductor migration. This migration would also explain the inability to obtain matched conditions which would allow higher power delivery to the plasma. The complex impedance of the cable varied from its standard 50 ohm real value as it became asymmetrical, resulting in a net impedance for the RF system outside of the range of the installed matching network.

The RG10 cable was replaced by a much larger diameter coaxial cable. This cable was used for several successful tests before it also suffered from center conductor migration, at which time it was replaced by the robust vacuum-gap custom coax assembly described in Section 7.1. The end of the large diameter coaxial cable can be seen in Figures 7.16 and 7.17 below.

After making the above described changes to the RF system, several experiments were conducted on November 30<sup>th</sup>, 2005. On that date, 8sccm of nitrogen was supplied to the device. Excellently matched conditions were obtained by adjusting the matching network capacitors. A 450W inductively coupled plasma was generated, as pictured in Figure 7.16 below. The purple and pink plasma obtained had a strong visible intensity. An axial magnetic field of ~1800G was applied, and the RF power was increased to approximately ~700W. For power levels above 450W, a distinct mode change was visible in the plasma, resulting in a significant increase in plasma brightness and intensity. Also a color change was observed to a light pink color. This discharge is pictured in Figures 7.17 and 7.18 below. The interpretation of this observed change is the onset of helicon mode operation.

The operation of the experiment was somewhat unstable. It was difficult to maintain matched conditions, as the impedance of the plasma varied with time. This effect was aggravated by oscillations in the gas flow through the system, which, in turn, varied the plasma impedance. The cause of these oscillations was determined to be the result of an



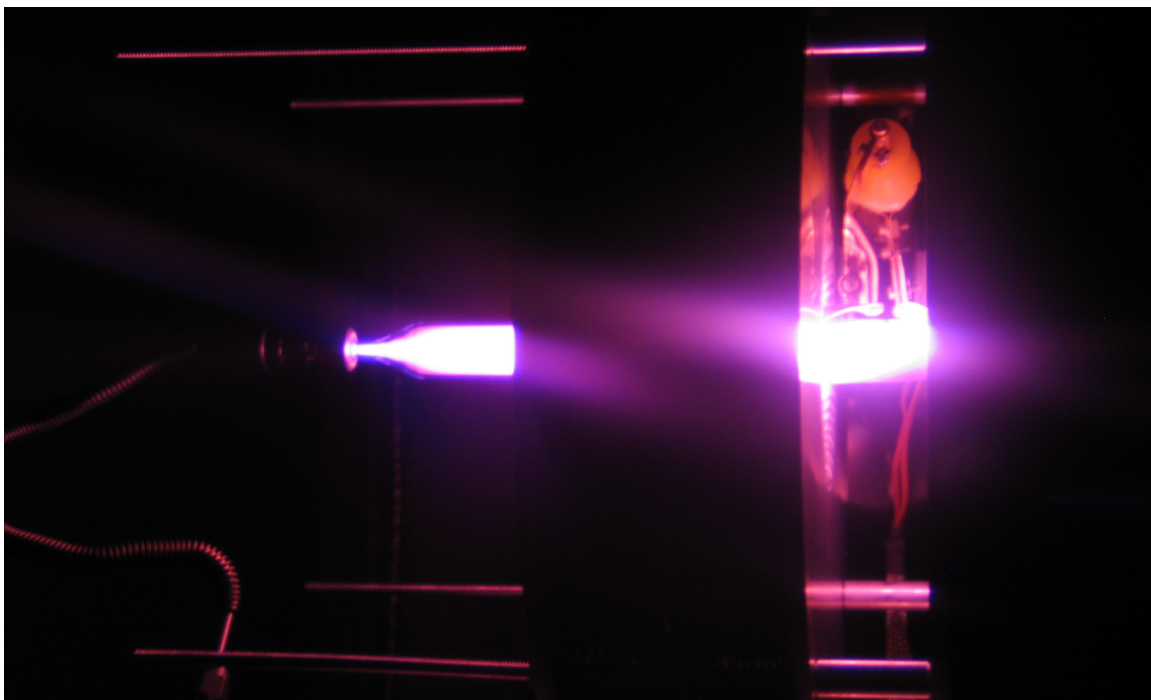


**Figure 7.16** Plasma Discharge,  $\sim 450\text{W}$ ,  $\text{N}_2$ , 8 sccm, ICP.

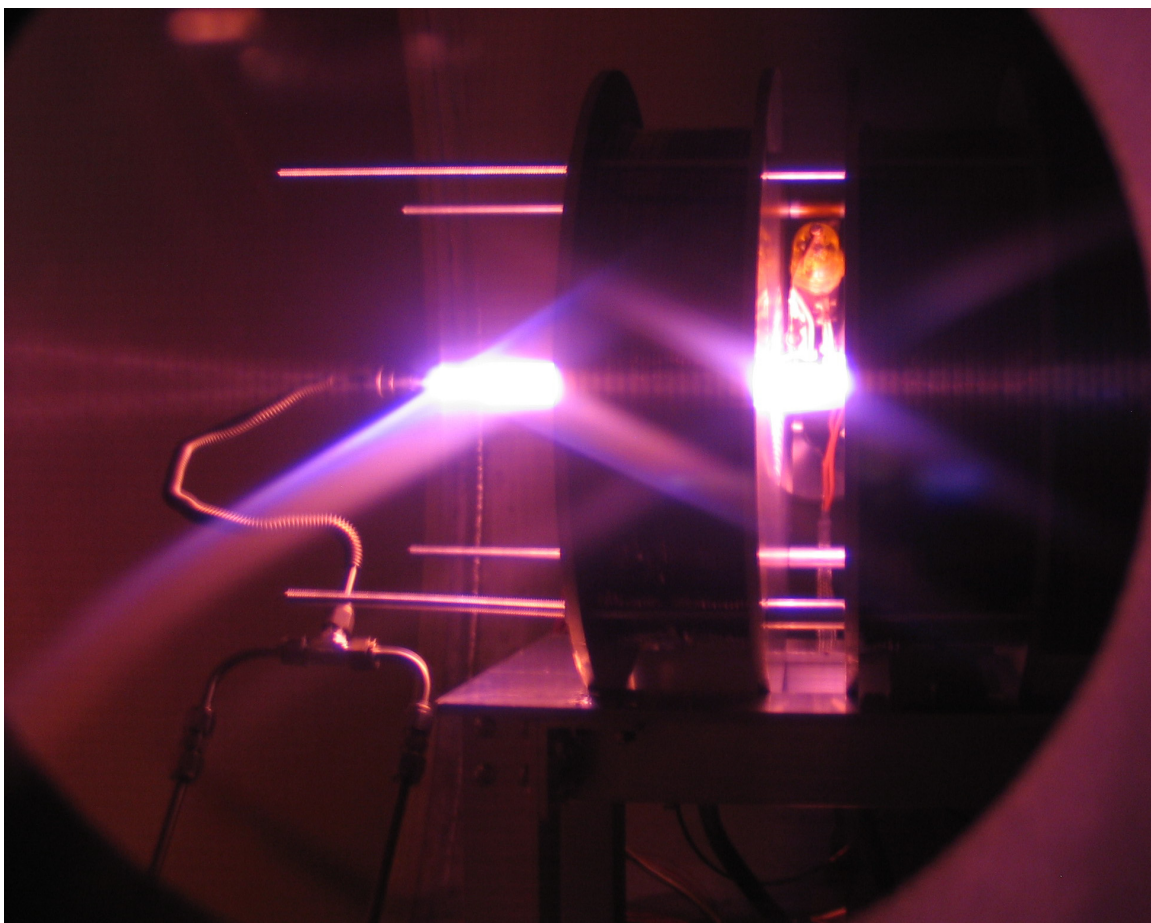


**Figure 7.17** Helicon Discharge  $\sim 700\text{W}$ ,  $\text{N}_2$ , 8 sccm,  $\sim 1500\text{G}$ .

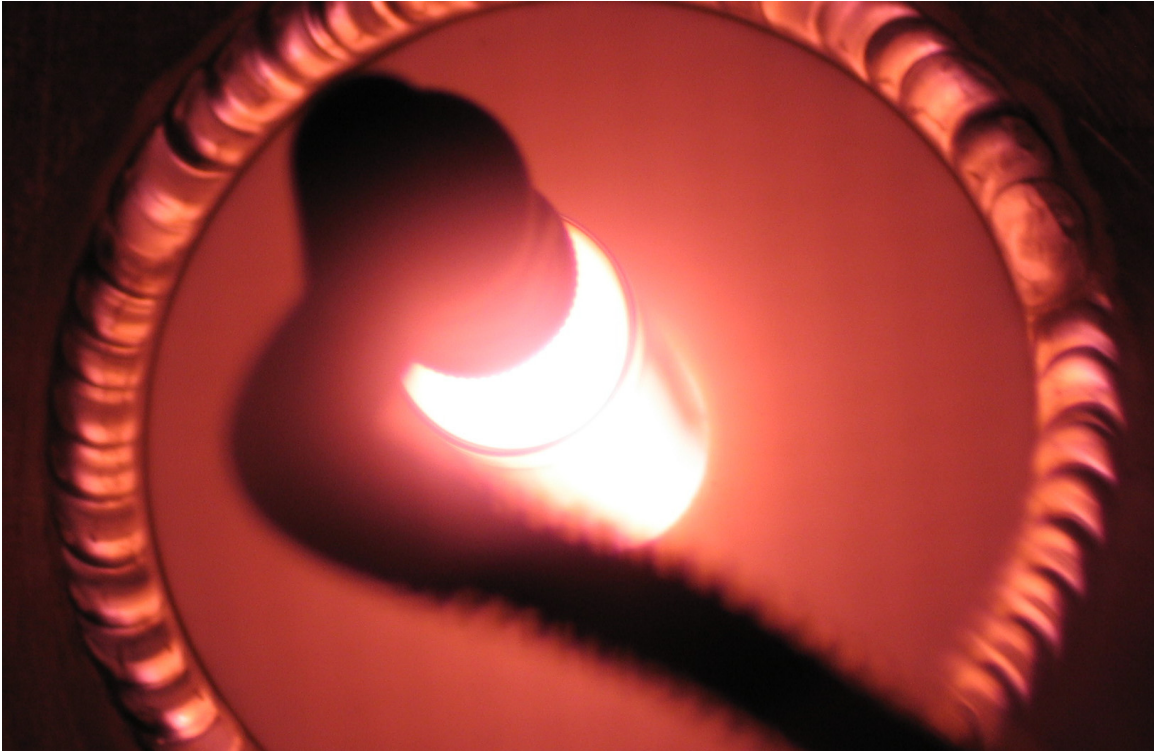


**Figure 7.18** Color and Intensity Change Indicative of a Mode Change to Helicon Wave Propagation.  $\sim 700\text{W}$ ,  $\text{N}_2$ , 8 sccm,  $\sim 1500\text{G}$ .

inadvertent ground loop in the RF return path. This loop was caused by grounding of plasma to the stainless steel gas supply line. RF return current flowed down this line to the mass flow controller, disrupting its operation, and eventually flowed through the chamber wall back to the matching network and RF generator. The contiguous stainless steel connection is clearly visible in Figures 7.16 and 7.17, as is the presence of plasma near the gas inlet. After replacing this connection with an electrically floating Swagelock connector and a short length of plastic tubing, gas oscillations were eliminated, plasma no longer migrated towards the gas inlet, and the operation of the experiment was much more stable.

During the course of troubleshooting the current loop issue described above, an abnormal operating regime was observed. When gas flow jumped rapidly between very little flow ( $\sim 2$  sccm) and high flow ( $\sim 20$  sccm) a glow discharge was observed which filled the entire vacuum chamber. This discharge is pictured in Figure 7.19 below. After maintaining itself for several seconds, the discharge returned to the confines of the quartz tube. This has been interpreted as a sudden pressure increase within the vacuum chamber, caused by the high gas flow rate, which resulted in a discharge throughout the chamber. The return to more typical behavior indicates that the vacuum system began to react to this transient, returning the chamber pressure to a lower value.



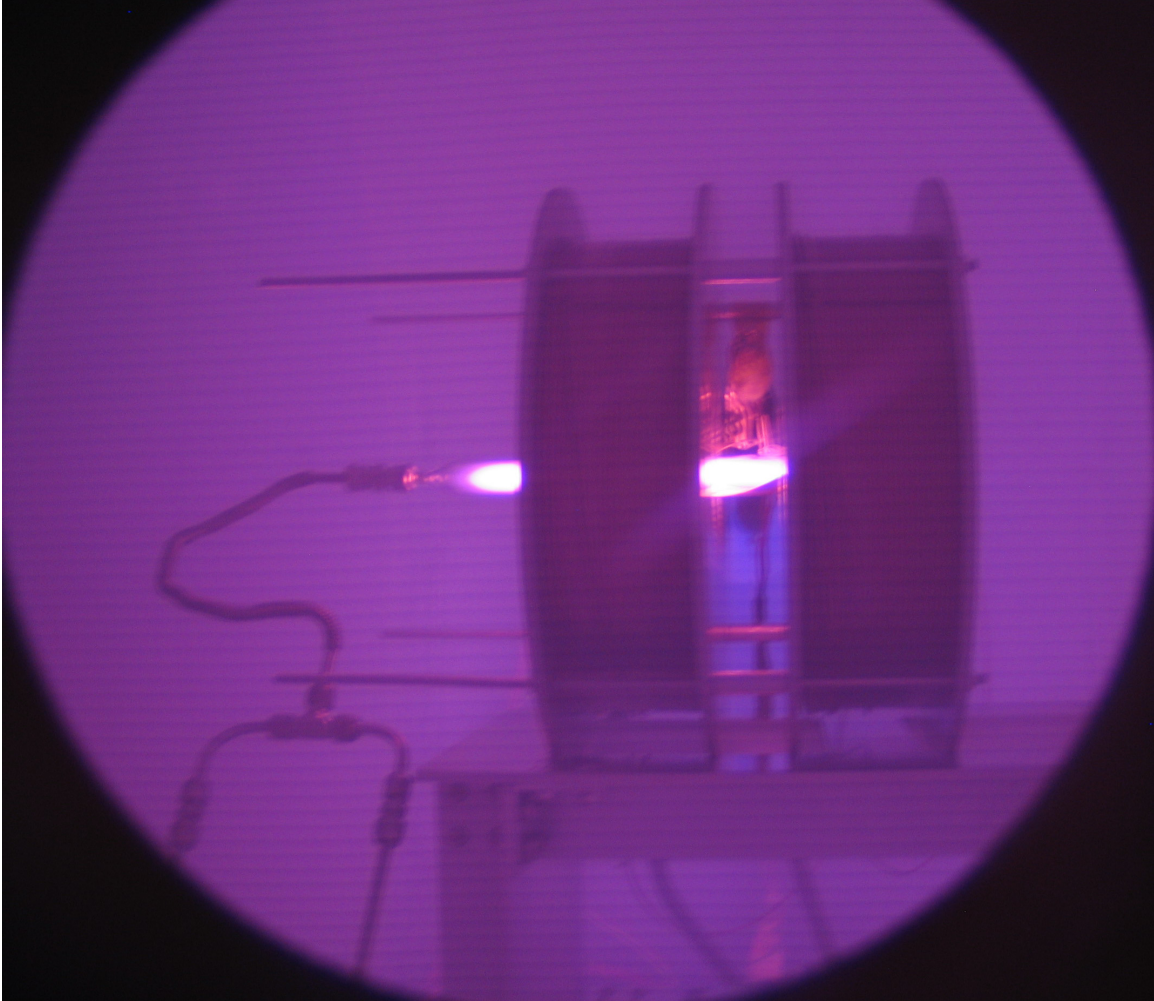


**Figure 7.19** Abnormal Operation - Glow Discharge Visible Within the Entire Vacuum Chamber.

Additional experiments were conducted on December 1, 2005<sup>1</sup>, utilizing argon gas. A stable 500W discharge was obtained, and 20 sccm flowed through the system. The current supplied to the electromagnets was continuously increased from 0 to 30A, resulting in an axial magnetic field sweep from 0 to ~2200G. A transformation of the discharge from a dim purple-pink color to an increasingly bright blue color was observed as the applied magnetic field was increased beyond 700G.

Plasmas produced at magnetic field strengths above 700G included the production of a visible plume which extended into the vacuum chamber. The plume increased in intensity as the magnetic field strength was increased. It was clearly observable that the plasma followed the magnetic field lines, as a characteristic solenoidal shape was visible. As the magnetic field strength increased, the plume became more focused and a central spike of plasma was observed, surrounded by a conical structure above ~1500G. This effect has been captured in Figures 7.20 and 7.21 below.

<sup>1</sup> Experiments on this date conducted by Justin Pucci and Nareg Sinenian. Experiments on other dates mentioned were jointly conducted by the SPL team, including the author.

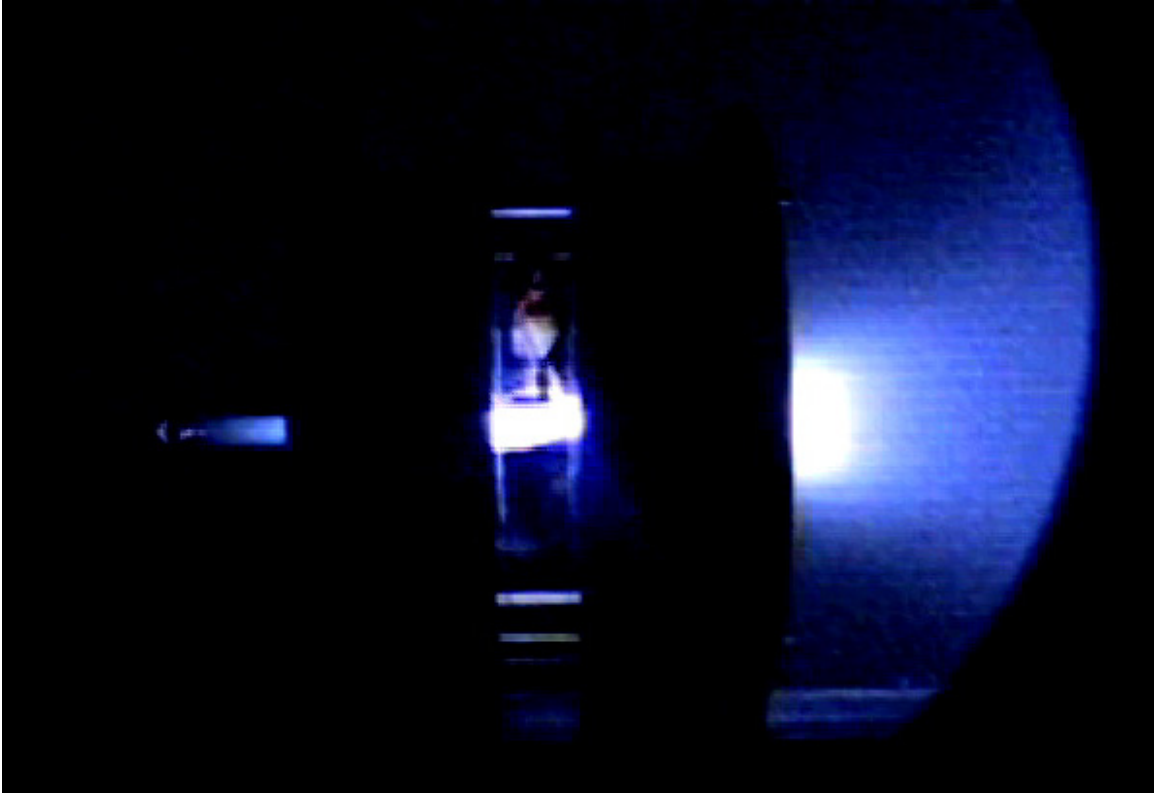


**Figure 7.20** Helicon Discharge with Visible Plume, ~500W, Ar, 20 sccm, ~850G.



**Figure 7.21** Helicon Discharge with Concentrated Plume, ~500W, Ar, 20 sccm, ~2200G.



# Chapter 8

## CONCLUSIONS

From the design, analysis and construction effort of the mHTX@MIT experimental apparatus we concluded that:

- For a hydrogen flow rate of 10 sccm, a thrust level of  $\sim 1$  mN has been predicted. This value has been calculated based on the chosen parameters of the experimental apparatus and on an assumption of a ion kinetic energy of  $\sim 2Te$ . This assumption is derived from literature review of similar Helicon sources.
- Applied axial magnetic fields above 1020G will result in electron and ion Larmour radii less of than  $1/10^{\text{th}}$  of the selected 1 cm tube radius. This is based upon elementary plasma theory.
- For a tube radius of 1.5 cm, tube length of 25 cm, and 10 sccm of hydrogen gas flow, low Mach number flow calculations indicate purely molecular flow throughout the tube length. Mach numbers are predicted to remain below the 1/3 limit at which gas inertial effects must be considered, for all but the last 12% of the tube length.
- A mechanical support structure as described in Chapter 5, can support the 180kg mass of the experimental apparatus with more than an order of magnitude safety margin. The design and construction of this robust and stable platform was required to support the massive wound copper electromagnetic coils which provide sufficient axial magnetic field strength to both obtain a helicon discharge and to achieve plasma containment.
- An RF power delivery system, as described in Chapter 6, has been assembled which can efficiently deliver power from the RF generator to the helicon antenna and plasma load. A matching network enclosure has been designed and constructed as described in Chapter 6.3, and this network can be manually tuned to provide matched impedance conditions. Instrumentation and procedures to support network tuning have been established as described in Section 6.4.
- Shielding and grounding concerns related to RF system design have been taken into consideration to prevent RF radiation from escaping into the lab environment and to prevent ground loops which can cause operational instabilities and disruption of controls and instrumentation. Wide and thin conductors have been used in the RF system to take into account the 18  $\mu\text{m}$  skin depth of copper at 13.56MHz.

From the early experimental investigations conducted with the operational mHTX@MIT apparatus we concluded that:

- A small-scale, operational helicon plasma source apparatus can be designed and constructed with minimal equipment and instrumentation.
- Inductively coupled plasmas between 40 and 700W, utilizing N<sub>2</sub> and argon propellant flows between 2 and 20 sccm, can be obtained in the experimental apparatus.
- For applied axial magnetic fields above ~800G a mode transition is visible in the plasma discharge resulting in an increase in discharge intensity and a change in color. These changes are interpreted as the onset of helicon wave propagation into the plasma, and the excitation of the next higher energy ions in the propellant gas being utilized. This applied magnetic field strength corresponds well with the requirement for plasma containment at this flow rate and tube radius.
- Boundary conditions play an important role in plasma stability. The presence of a ground path for plasma in the tube near the gas injection point resulted in plasma migration to this upstream location and caused plasma impedance changes which lead to instabilities. Replacement of this conductive path with an insulative connection resulted in less plasma migration and more stable operation.
- Plume formation was visible for operation with argon gas for applied axial magnetic field strengths above ~800G. As the intensity of this field is increased, a change in the plume is visible, whereby it is concentrated more into the axial direction, exhibiting less plume divergence. The presence of the plume is a positive indication that plasma remains at high energies beyond the tube region. For lower energy and less well contained propellants, wall collisions result in energy transfer and an extinguishing of the plasma prior to the end of the quartz tube.

## **8.1 Suggestions for Experiment Improvements and Future Research**

This thesis, and the work of the mHTX@MIT team to this date, represent the initial steps of a continuing and expanding research program. The development of the experimental apparatus and early plasma measurements provide a framework on which this further research can be conducted. A number of improvements and additions to the experimental apparatus are here suggested, as well as future research directions.

In the near future, a full characterization of the experiment's operation should be investigated utilizing a variety of propellant gases, power levels, flow rates and applied axial magnetic fields. This will allow greater understanding of the interaction of the

various subsystems which comprise the experiment, and provide a wealth of useful data which can be compared to theoretical calculations.

Present control of the experiment involves operation of a number of systems manually via front panel displays. This is the case for both the RF generator and the two electromagnet DC power supplies. It is suggested that these systems can be interfaced with the control computer, providing centralized experiment control and monitoring. With the present Labview implementation, this would allow the creation of pre-designed programs whereby experimental parameters could be manipulated in a controlled and repeatable manner, and feedback data could be recorded for future reference.

The addition of numerous sensor systems to the experimental apparatus is highly desirable, as such will provide additional knowledge on system operation. Some of the proposed sensor systems are described in Section 3.1.5 of this thesis.

One potential sensor system would consist of a number of gaussmeters which would provide measurement of magnetic field strength. Creating an axial profile of applied magnetic field may yield further insight into plasma conditions. Variation of this profile by varying applied coil current may result in changes to the plume and other plasma parameters.

Some initial spectrometry data has been collected of the plasma discharge, by making use of an optical sensor applied to the vacuum chamber view port<sup>1</sup>. This data will be published at a future date. It may be desirable to obtain additional spectroscopy data by utilizing an optical vacuum feedthrough and a variable position optical pickup within the chamber. This would allow adjustment of the axial location in the discharge to be observed, a result not possible when locating the optical pickup outside the chamber view port. Optical spectrum obtained in such a manner could indicate the axial location at which different ion species are developed.

Another desirable modification would be the installation of a mechanical swing arm, to which various sensors may be installed and moved through the plume region in a controlled manner. This would allow a greater understanding of the plume region. Such a swing arm is described in more detail in Section 5.2.

Thrust is another parameter, the measurement of which is highly desirable. In order for this device to eventually become a working space electric propulsion system, thrust generation must be optimized. This optimization may not be possible without a direct measurement of the thrust which the experimental apparatus is generating. Potential means for executing this measurement include the use of a pusher plate and a mechanical thrust balance stand on which the entire experimental apparatus would be located.

Additional improvements may be possible in many of the other experiment subsystems. One such improvement would be the addition of an active cooling system to the electromagnetic coils. The present coils have no such cooling system, and must depend

---

1. Data collection, and collection system design, by Murat Celik.

upon radiative and conductive heat transfer to dissipate a buildup in thermal energy. The temperatures of the coils are monitored to prevent them from exceeding the 200C limit of the coil wire lacquer insulation. When this limit is approached, experiment investigations must cease until their temperature has returned to a lower level. An active cooling system would allow continuous experiment operation, at the cost of increased system complexity.

Another potential improvement involves the RF power delivery subsystem. Plasma impedance changes as other experiment parameters are varied, requiring manual tuning of the present network. Implementation of an automatic matching network, which tracks the plasma impedance, and through use of a feedback loop automatically maintains matched conditions, may be desirable.

A number of potential helicon antenna geometries are known beyond the common design implemented in this experimental apparatus. Experimentation with various helicon antenna geometries may provide additional insight, potentially making this a desirable research path.

Finally, it is suggested that investigation of the changes necessary to create a flight ready device would be of value. Such an investigation would consider, among other factors, the potential use of superconducting magnets to provide the necessary axial magnetic field.

It is hoped that this thesis research and the continuing efforts of the mHTX@MIT team lead to further investigation on the creation of a small, efficient and unique plasma thruster. The experimental setup established at the MIT SPL will provide new capabilities for realizing these investigations and provide opportunities for future students, professors, and the scientific community at large.





# REFERENCES

- [Pucci, 2006] Pucci, J. M., Sinenian, N., Palaia, J., LaBry, Z., Shabshelowitz, A., Celik, M., Batishchev, O., and Martinez-Sanchez, M., *mHTX@MIT: Characterization of a Mini Helicon Plasma Thruster*, MIT, 2006.
- [LaBry, 2006] Pucci, J. M., LaBry, Z., Batishchev, O., and Martinez-Sanchez, M., *mHTX@MIT: An Overview of Current Modeling Efforts of a Mini Helicon Plasma Thruster*, MIT, 2006.
- [ESA, 2005] European Space Agency, *ESA accelerates towards a new space thruster*, December 13, 2005. [http://www.esa.int/esaCP/SEM6HSVLWFE\\_index\\_0.html](http://www.esa.int/esaCP/SEM6HSVLWFE_index_0.html)
- [Lozano, 2005] Lozano, P., *Vacuum System Procedures*, MIT Space Propulsion Laboratory, MIT, 2005.
- [Squire, 2004] Squire, J., *Deuterium 20 kW helicon operations at 13.56 MHz Helicon B-field scaling*, NASA Johnson Space Center Advanced Space Propulsion Lab, December 2004.
- [Boswell, 2004] Boswell, Sutherland, Charles, Squire, ChangDiaz, Glover, Jacobson, Chavbers, Bengtson, Bering, Goulding, Light. *Experimental evidence of parametric decay processes in the variable specific impulse magnetoplasma rocket (VASIMR) helicon plasma source*, Physics of Plasmas, Vol 11, No 11, November 2004.
- [CRC Press, 2004] Handbook of Chemistry and Physics, 85<sup>th</sup> Ed., CRC Press, LLC., 2004, <http://www.hbcnetbase.com>.
- [Charles, 2004A] Charles, C., and Boswell, R.W., *Time development of a current-free double-layer*, Phys. Plasmas, Vol. 11, No. 8, August 2004.
- [HDLT, 2004] Helicon Double Layer Thruster webpage, Australian National University, Space Plasma and Plasma Processing Group, May 2004  
<http://prl.anu.edu.au/020research/130SP3/020research/HDLT/background/>
- [Charles, 2004B] Charles, C. and Boswell, R.W., *Laboratory evidence of a supersonic ion beam generated by a current-free ‘helicon’ double-layer*, Phys. Plasmas., Vol. 11 No. 4., pp. 1709, April 2004.
- [Tysk, 2004] Tysk, S. M., Denning, C. M., Scharer, J. E., and Akhtar, K., *Optical, wave measurements, and modeling of helicon plasmas for a wide range of magnetic fields*, Physics of Plasmas, March, 2004.

- [NRL, 2004] Naval Research Laboratory (NRL), *NRL Plasma Formulary*, Washington D.C., NRL/PU/6790—04-477, Rev 2004.
- [Pucci, 2004] Pucci, J. M., *Helicon Wave Theory: Current Understanding*, MIT Department of Aeronautics and Astronautics, 2004.
- [HPHT, 2004] High Power Helicon Thruster Website, University of Washington, 2004, <http://www.ess.washington.edu/Space/propulsion.html>
- [LMNO Eng, 2003] *Gas Viscosity Calculator.*, LMNO Engineering, Research, and Software, Ltd., 2003, <http://www.lmnoeng.com/Flow/GasViscosity.htm>.
- [Batishchev, 2003] Batishchev, O., Molvig, K., Chang-Diaz, F., Squire, J., *Study of Gas Burn-out Regime in the VASIMR Helicon Plasma Source*, Paper O-3.3D, -4p, 30<sup>th</sup> EPS CFPP Conference, St. Petersburg, Russia, July 7-11, 2003.
- [Chen, 2003] Chen, F.F., *The low-field density peak in the helicon discharges*, Phys. Plasmas, Vol. 10, No. 6, June 2003.
- [Molvig, 2003] Batishchev, O., and Molvig, K., *VASIMR Thruster Operation with Hydrogen and Helium Gas Propellants*, paper IEPC03-191, -12p, 28<sup>th</sup> IEPC, Toulouse, France, March 17-21, 2003.
- [ASPL, 2003] Advanced Space Propulsion Laboratory Website, NASA Advanced Space Propulsion Laboratory, 2003, <http://spaceflight.nasa.gov/shuttle/support/researching/aspl/plasma.html>
- [Alcoa, 2002] Alcoa Aluminum, *Understanding Extruded Aluminum Alloys*, December 2002, [http://www.galcit.caltech.edu/~tongc/html/data/elastic/Extruded\\_Alloy\\_6061.pdf](http://www.galcit.caltech.edu/~tongc/html/data/elastic/Extruded_Alloy_6061.pdf)
- [UWM, 2002] University of Wisconsin-Madison Helicon Plasma Research Website, University of Wisconsin-Madison, August 2002, <http://legolas.ece.wisc.edu/helicon/>
- [Perry, 2002] Perry, A., Conway, G., Boswell, R., Persing, H., *Modulated plasma potentials and cross field diffusion in a Helicon plasma*, Phys. Plasmas, Vol. 9, No. 7, July 2002.
- [David, 2002] David, Leonard, *NASA's Need for Speed: Advanced Propulsion Comes of Age*, Space.com Tech Wednesday, May 22, 2002, [http://www.space.com/business/technology/technology/advanced\\_propulsion\\_020522-1.html](http://www.space.com/business/technology/technology/advanced_propulsion_020522-1.html).



- [Sankovic, 2002] Sankovic, J. M., *NASA Technology Investments in Electric Propulsion: New Directions in the New Millennium*, Prepared for the Third International Conference on Spacecraft Propulsion cosponsored by the Centre National d'Etudes Spatiales and the European Space Agency, Cannes, France, October 10-13, 2000. NASA/TM—2002-210609, February 2002, <http://gltrs.grc.nasa.gov/reports/2002/TM-2002-210609.pdf>
- [Barber, 2002] Barber, R. W., and Emerson, D. R., *Hydrodynamic Development Length of Gas Flows in Micro-scale Pipes and Channels*, Daresbury Laboratory, 2002, <http://www.cse.clrc.ac.uk/ceg/devlen/devlen.shtml>.
- [Watts, 2001] Watts, C., *Multi-helicon operation in alpha*, New Mexico Tech, 2001 APS-DPP Meeting – mini-conference on Helicon Plasma Sources, October 2001, <http://ulysses.phys.wvu.edu/~escime/miniconference/watts.pdf>
- [Batishchev, 2001] Batishchev, O., Molvig, K., *Kinetic model for a mixed collisional rarified gas flow*, First M.I.T conference on computational fluid and solid mechanics, Cambridge, MA, June 12-15, 2001.
- [Molvig, 2001] Batishchev, O., Molvig, K., *Kinetic Model of a Helicon Plasma Source for VASIMIR*, 39<sup>th</sup> ASME, AIAA technical paper 2001-0963, 12 p, 2001.
- [Chen, 2001] Chen, F.F., Evans, J.D., Tynan, G.R., *Design and performance of distributed helicon sources*, Plasma Sources Sci. Technol. 10, 236, 2001; UCLA LTP-008 August 2000.
- [ALESPI, 2001] Auburn Linear Experiment for Space Plasma Investigations (ALESPI) Webpage, Auburn University, August 2001, <http://www.physics.auburn.edu/~plasma/basic/spacelab/alespi.html>
- [Schofield, 2001] Schofield, David. W., Online Resume, <http://www.icubed.com/~control>
- [ORNL, 2001] Oak Ridge National Labs (ORNL) Fusion Energy Division Webpage, Oak Ridge National Labs, 2001, <http://www.ornl.gov/sci/fed/Technology/tsa/tsa.htm>
- [M2P2, 2001] Mini-Magnetospheric Plasma Propulsion (M2P2) Webpage, University of Washington, 2001, <http://www.ess.washington.edu/Space/M2P2/>
- [Charles, 2000] Charles, Degeling, Sheridan, Harris, Lieberman, Boswell. Absolute measurements and modeling of radio frequency electric fields using a retarding field energy analyzer, Phys. Plasmas, Vol.7, No. 12, December 2000.
- [Batishchev, 2000] Batishchev, O., Molvig, K., *Study of Operational Regimes of the VASIMR Helicon Plasma Source*, Bull. APS 45 (7) 130, DPP/ICPP 2000 Meeting, Quebec City, Canada, 2000.

- [Scime, 2000] Scime, E., *Laboratory Flow Measurements in a Helicon Plasma Source Thruster*, West Virginia University, Mini Conference on Plasma Propulsion, APS Division of Plasma Physics, Quebec City, 2000
- [WVU, 2000] Hot hELIcon eXperiment – HELIX Webpage, West Virginia University, 2000, <http://www.as.wvu.edu/coll03/phys/users/escime/plasma/expdevices/helix/helicon.html>
- [Chen, 1997] Chen, F.F. and Arnush, D., *Generalized theory of helicon waves. I. Normal modes*, Phys. Plasmas., Vol. 4 No. 9., pp. 3411-3421, Sept. 1997.
- [Degeling, 1997] Degeling and Boswell, Modeling Ionization by Helicon Waves., Phys. Plasmas., Vol. 4 No. 7., July 1997.
- [Chen, 1996] Chen, F.F., *Physics of Helicon Discharges*, Phys. Plasmas, Vol. 3, No. 5, May 1996.
- [Filliben, 1996A] Filliben, J. D., *Electric Propulsion for Spacecraft*, Chemical Propulsion Information Agency, Johns Hopkins University, 1996, [http://www.cpia.jhu.edu/pdfs/cptrs/cptr\\_96-64.pdf](http://www.cpia.jhu.edu/pdfs/cptrs/cptr_96-64.pdf)
- [Filliben, 1996B] Filliben, J.D., *Electric Thruster Systems*, Chemical Propulsion Information Agency, Johns Hopkins University, 1996, [http://cpia.jhu.edu/pdfs/cptrs/cptr\\_96-65.pdf](http://cpia.jhu.edu/pdfs/cptrs/cptr_96-65.pdf)
- [McFall, 1995] McFall, K.A., Tilley, D.L., Gulczinski, F.S., III, *Low Power Arcjet Performance Evaluation*, Philips Lab., Edwards AFB, CA USA, Report No.(s) AD-A439301; IEPC-95-18, January 1, 1995, <http://aero.ihs.com/news-05Q4/star-1202-launch-vehciles.jsp>
- [Popov, 1995] Popov, O. A., *High Density Plasma Sources. Design, Physics and Performance*, Noyes Publications, Park Ridge, NJ, 1995.
- [Campbell, 1992] Campbell, G.A., de Chambrier, A., Mendoza, F., Parker, N.W., Pearson, D. I. C., Tokunaga, K., Tsukada, T., Mashiro, S., and Nogami, H., *Proceedings of the Society of Photo-Optical Instrumentation Engineers*, 1803:226, 1992.
- [Chen, 1992] Chen, F.F., Decker, C.D., *Electron Acceleration in Helicon Sources*, Plasma Physics and Controlled Fusion, Vol. 34, No. 4, pp635 – 640, 1992.
- [Chapman, 1991] Chapman, B., Benjamin, N., van Os, C. F. A., Boswell, R. W., and Perry, A. J., *Plasma dry processing in the helicon reactor*, 12<sup>th</sup> Symposium on Dry Process, Denki-Gakkai, Tokyo, 1991.

- [Olson, 1990] Olson, R. M. and Wright, S. J., *Essentials of Engineering Fluid Mechanics*, 5<sup>th</sup> Ed., Harper & Row Publishers, New York, 1990.
- [Martinez-Sanchez, 1998] Martinez-Sanchez, M. and Pollard, J. E., *Spacecraft Electric Propulsion - An Overview*. Journal of Propulsion and Power, 0748-4658, Vol.14 No. 5, pp 688-699, 1998.
- [Cheng, 1989] Cheng, D. K. Field and Wave Electromagnetics, 2<sup>nd</sup> Edition, Addison-Wesley Publishing Company, Reading, MA, 1989.
- [Chen, 1984] Chen, F.F., Introduction to Plasma Physics and Controlled Fusion, 2<sup>nd</sup> Edition, Plenum Press, New York, 1984.
- [Dushman, 1962] Dushman, S., and Lafferty, J.M., Scientific Foundations of Vacuum Technique, 2<sup>nd</sup> Ed., John Wiley & Sons, Inc., New York, 1962.
- [Loeb, 1961] Loeb, L. B., The Kinetic Theory of Gases, Dover Publications, Inc., New York, 1961.
- [Shapiro, 1953] Shapiro, A. H., The Dynamics and Thermodynamics of Compressible Fluid Flow, Vol 1, John Wiley & Sons, Inc., New York, 1953.



# Appendix A

## Experiment Component Data

This appendix contains additional specific data on components and equipment used in the mHTX@MIT experimental setup. This additional data is included here for reference purposes.

Component	Manufacturer	Model / Part #	Serial #	Description
Flow Meter	Omega	FMA6508ST	144387-1	Digital Mass Flow Controller, 0-100mL/min N2
Magnet DC Power Supply 1	HP	6479C	1125A00226	0-300V, 0-35A DC PS
Magnet DC Power Supply 2	HP	6479C	1125A00228	0-300V, 0-35A DC PS
Oscilloscope	HP	54601A	-	100Mhz Scope
Scope Voltage Probe	Agilent	10076A	-	100:1 Probe. 66.7Mohm 3pf, 1Mohm 7-20pf 1kVpk CAT II, 4kVpk CAT I
RF Generator	RF Power Products Inc.	RF-10S/PWT	-	1KW, 13.56MHz, pulse capable
Data Acquisition System Breakout box	National Instruments	SCB-100	-	-
Cryo Pump #1	CTI-Cryogenics	8018184	13E841912	Cryo-Torr 10 Cryopump
Cryo Pump #2	CTI-Cryogenics	8115801G002	OL9911422	On-Board 400 Cryopump

### Materials List for Helicon Experiment Stand

Piece	# of Pieces	Material	Description & Dimensions
Top & Bottom Plates	2	Aluminum	Plate - 1/4" thick, 49cm x 27cm
Frame Uprights	4	Aluminum	Angle, 3/16" thick wall, 2" on a side, 30cm long ea
Brackets	16	Aluminum	Angle, 3/16" thick wall, 2" on a side, 2" long ea
Cross Beams	2	Aluminum	Strip, 0.375" thick, 2" wide, 49cm long ea.

Actual Pieces Ordered From McMaster Carr to Satisfy Above

Number of Pieces	Material	Shape	Description & Dimensions	McMaster Carr Part #	Price Ea	Total Price
1	Aluminum	Angle	3/16" thick wall, 2" on a side, 8' length	88805K64	\$ 39.23	\$ 39.23
2	Aluminum	Plate	1/4" thick, 12" x 24"	1651T42	\$ 82.50	\$ 165.00
1	Aluminum	Strip	Rectangular Strip 0,375" thick, 2" wide, 6' long ea.	8975K51	\$ 33.22	\$ 33.22

Total: **\$ 237.45**



# Appendix B

## Additional Experiment CAD Drawings

Various CAD drawings were created during the course of this thesis work. This appendix contains drawings that were not included in the thesis text, but provide additional details of the experimental assembly.

### **A.B.01** Support 1 of the Mechanical Support Structure.....125

Component to the mechanical support structure, manufactured from angle aluminum. This component comprises two of the vertical legs that make up the structure and carry the weight of the experimental apparatus.

### **A.B.02** Support 1b of the Mechanical Support Structure.....126

Component to the mechanical support structure, manufactured from angle aluminum. This component comprises two of the vertical legs that make up the structure and carry the weight of the experimental apparatus.

### **A.B.03** Support 2 of the Mechanical Support Structure.....127

Component to the mechanical support structure, manufactured from angle aluminum. This component serves as a connector, linking other components together. Twelve identical pieces are used in the final assembly.

### **A.B.04** Top Plate of the Mechanical Support Structure.....128

Component to the mechanical support structure, manufactured from aluminum plate. This component is the top platform which cradles the electromagnetic coil bobbins and supports their weight. It also connects all four legs together.

### **A.B.05** Bottom Plate of the Mechanical Support Structure.....129

Component to the mechanical support structure, manufactured from aluminum plate. This component is the bottom platform which provides stability to the structure by tying the vertical legs together at a second location. It also provides a mounting surface for the proposed plume sweep arm assembly.

### **A.B.06** Support 3 of the Mechanical Support Structure.....130

Component to the mechanical support structure, manufactured from aluminum bar stock. This component was added after the frame analysis, to provide additional support of the top plate.

**A.B.07** Plastic Mounting Block 1 of the Matching Network.....131

Component to the matching network, manufactured from G10 plastic block. This component serves as an insulating mounting location for one end of the two variable capacitors. It is installed in the matching network enclosure by use of three ¼-20 bolts.

**A.B.08** Plastic Mounting Block 2 of the Matching Network.....132

Component to the matching network, manufactured from G10 plastic block. This component serves as an insulating mounting location for the opposite end of the two variable capacitors. It is installed in the matching network enclosure by use of three ¼-20 bolts.

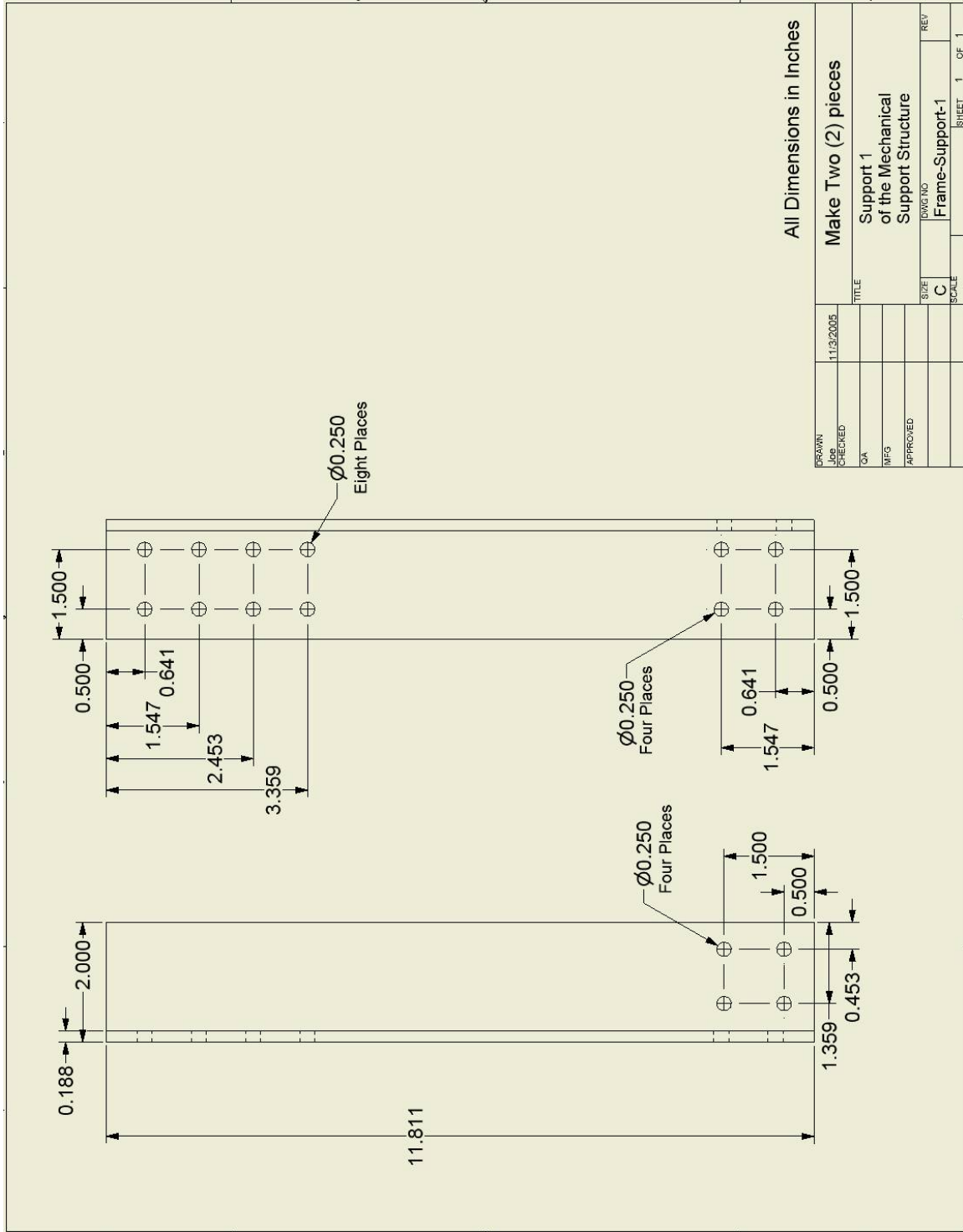
**A.B.09** Plastic Control Knob Extension of the Matching Network.....133

Component to the matching network, manufactured from G10 plastic rod. This component serves as an insulating extension of the control knobs for the two variable capacitors. The ends of these knobs extend through a hole in the matching network enclosure. Slots (which are not shown in the drawing) have been added to the ends of these knobs, into which a screwdriver can be inserted and used to make capacitance value adjustments.

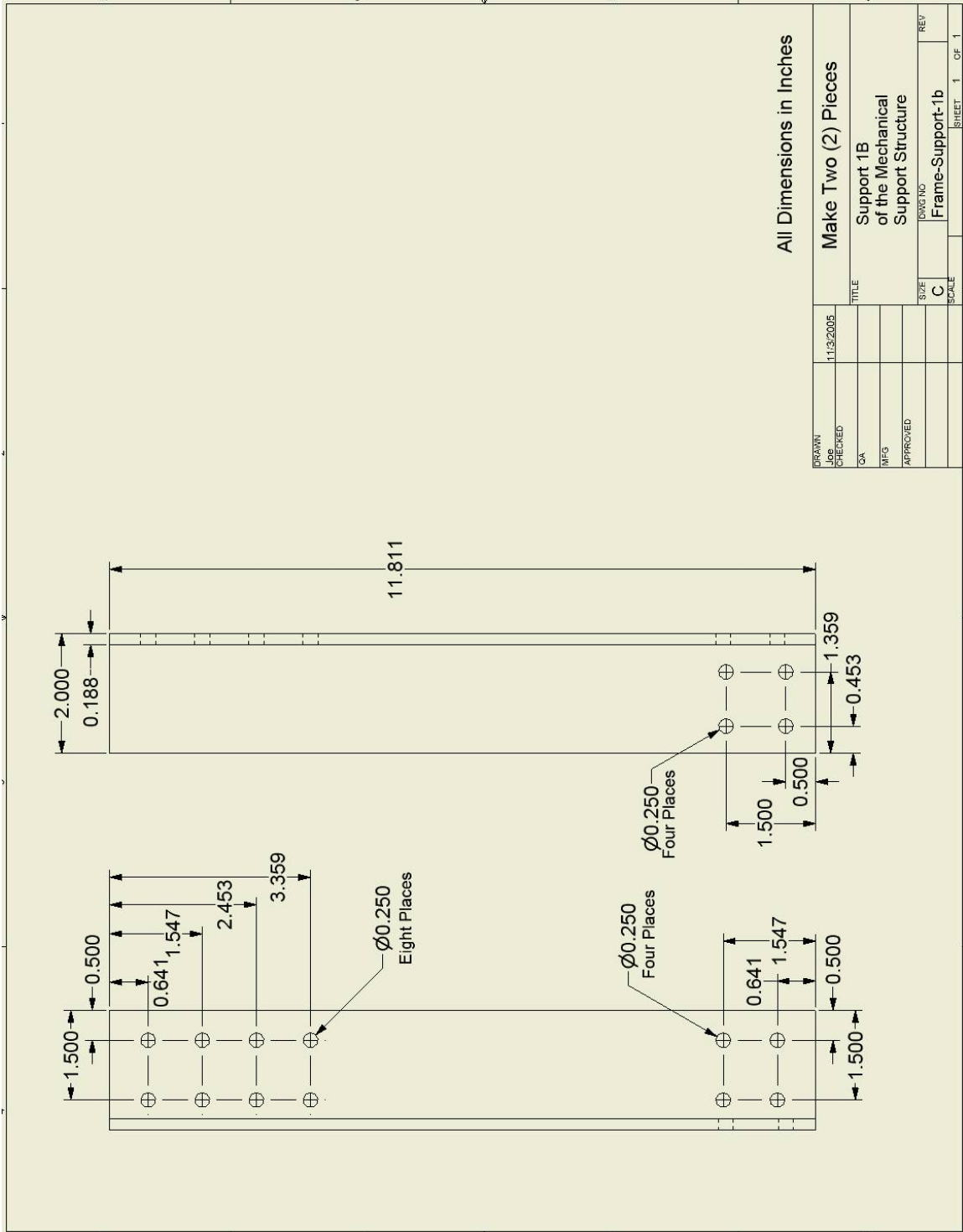
**A.B.10** Matching Network Metal Enclosure.....134

Component to the matching network, manufactured from sheet aluminum. This component is the backbone of the matching network, providing a common mounting interface. It also acts as a Faraday cage, shielding the RF fields which are generated within.

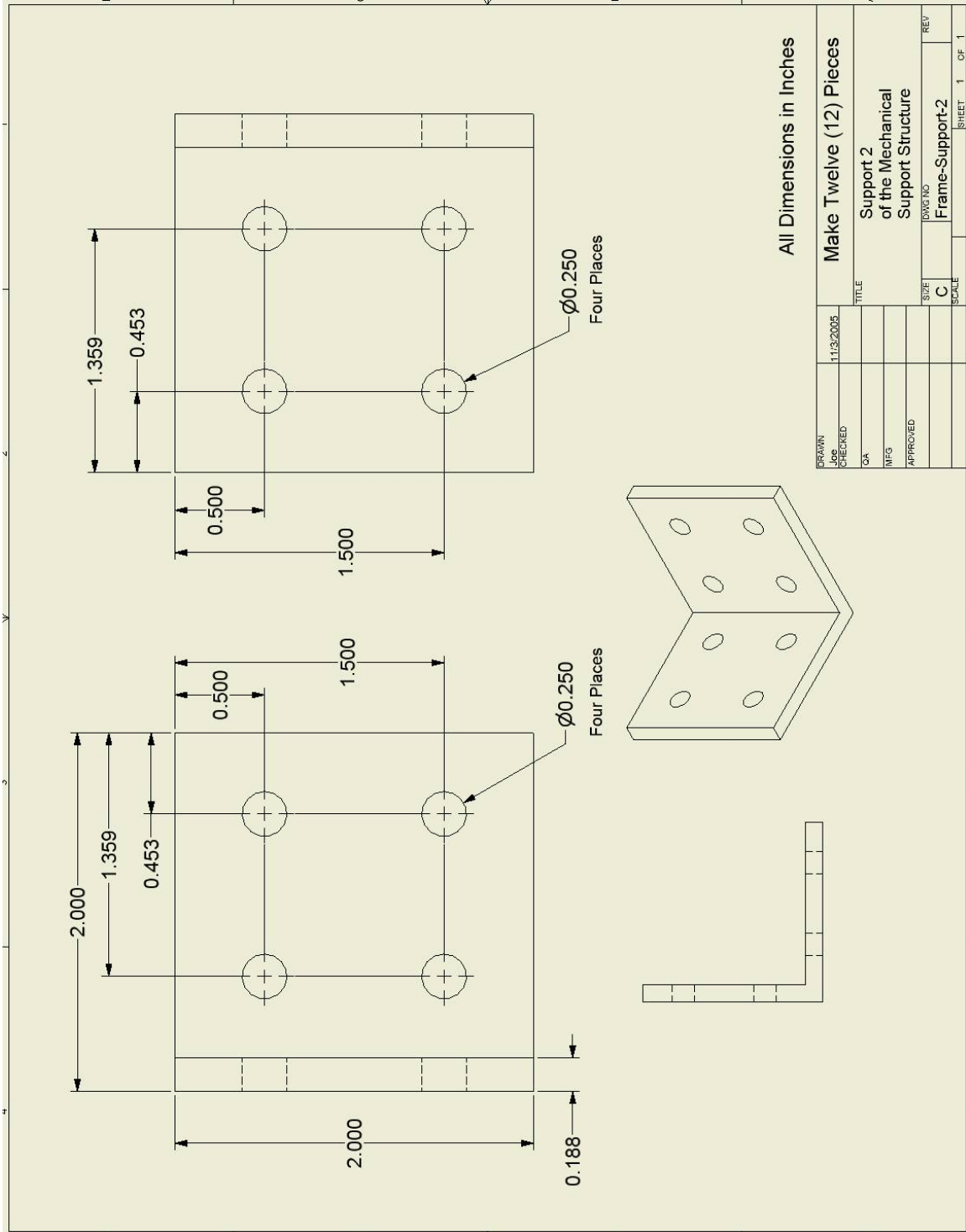




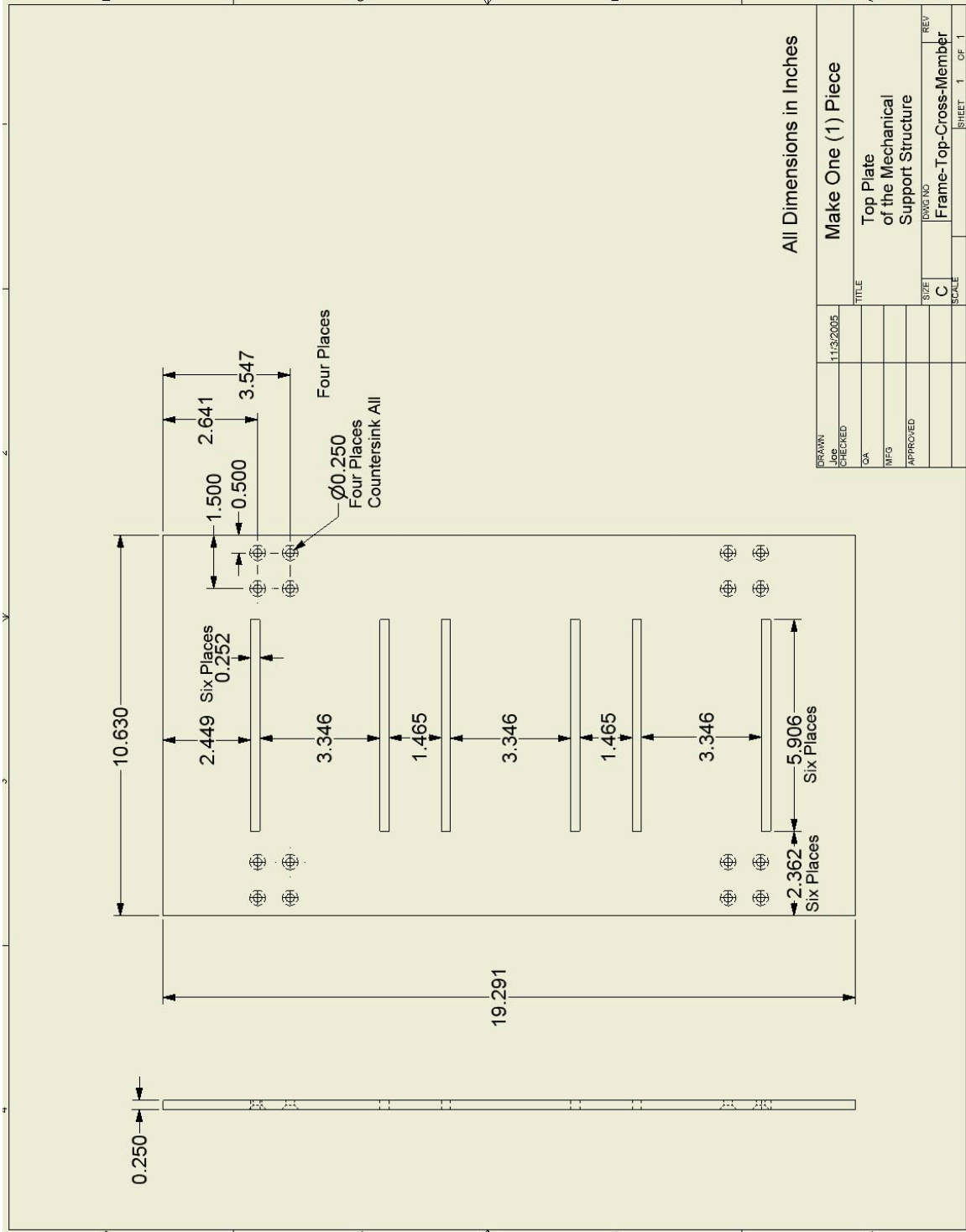
A.B.01 Support 1 of the Mechanical Support Structure



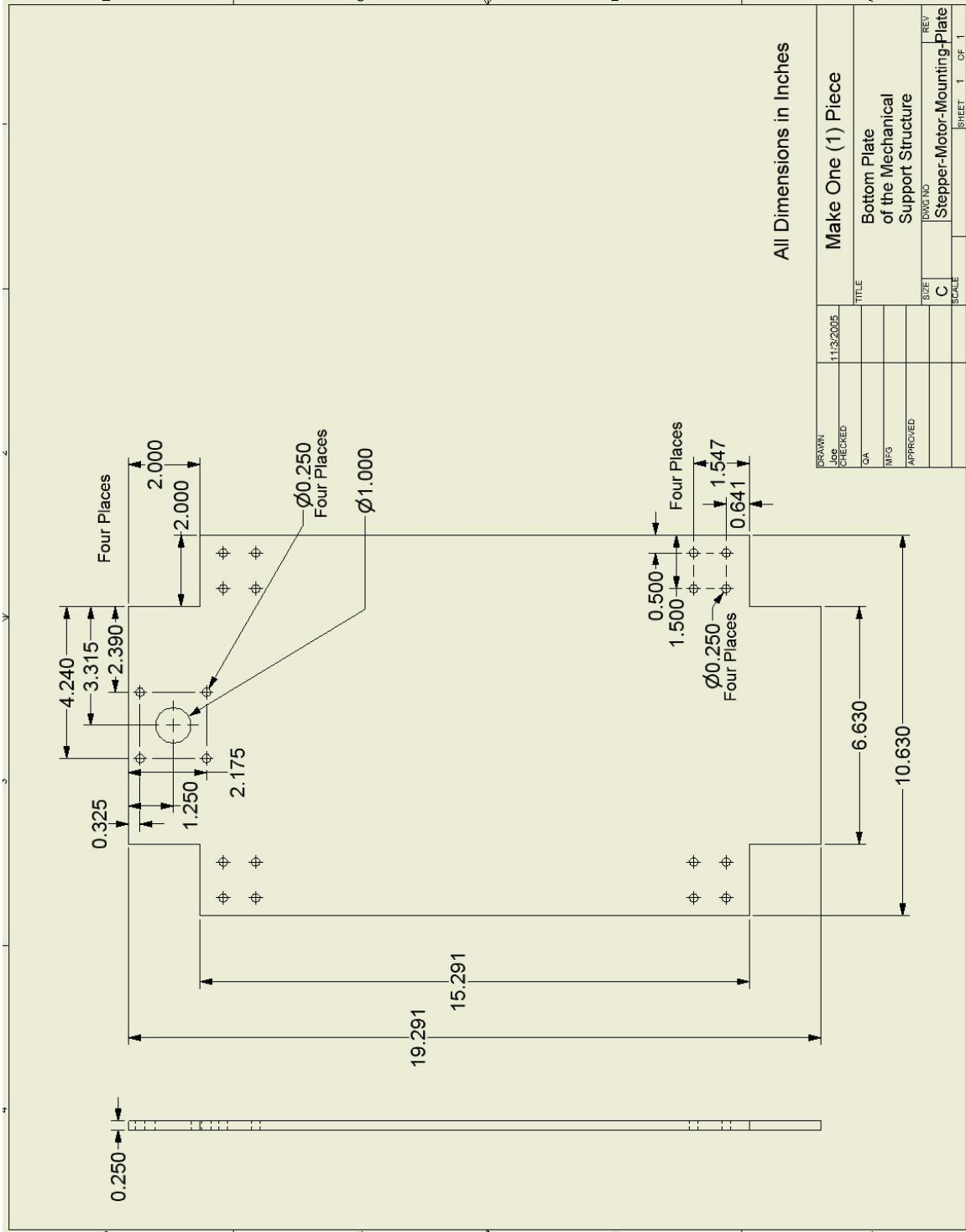
A.B.02 Support 1b of the Mechanical Support Structure



A.B.03 Support 2 of the Mechanical Support Structure



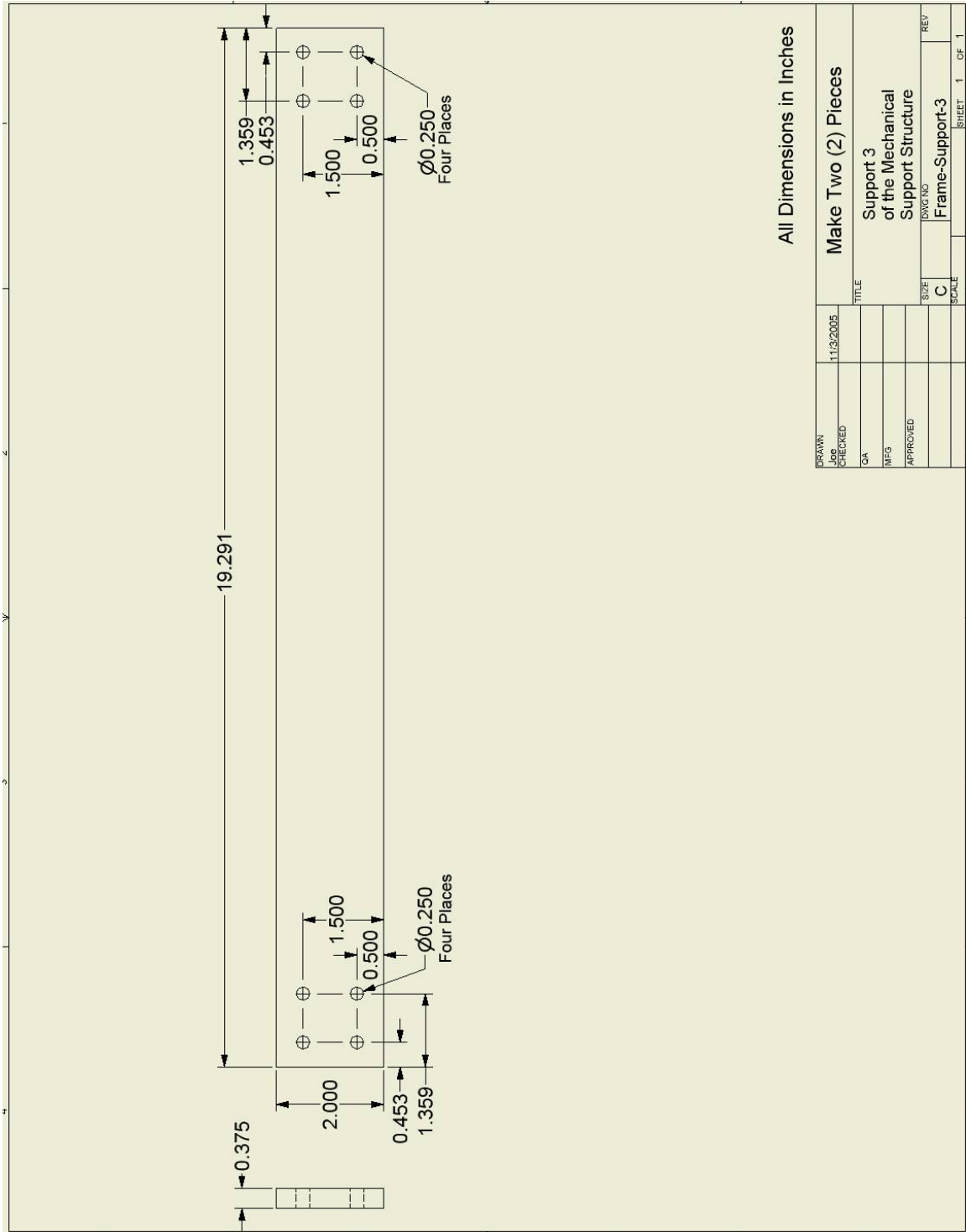
**A.B.04** Top Plate of the Mechanical Support Structure



**A.B.05** Bottom Plate of the Mechanical Support Structure

All Dimensions in Inches

DATE	11/13/2005	TITLE	Make One (1) Piece
DESIGNED		SIZE	C
CHECKED		SCALE	
QA		REV	
INFO		Bottom Plate of the Mechanical Support Structure	
APPROVED		Stepper-Motor-Mounting-Plate	
		DRAWING NO. 1 OF 1	
		SHEET 1 OF 1	

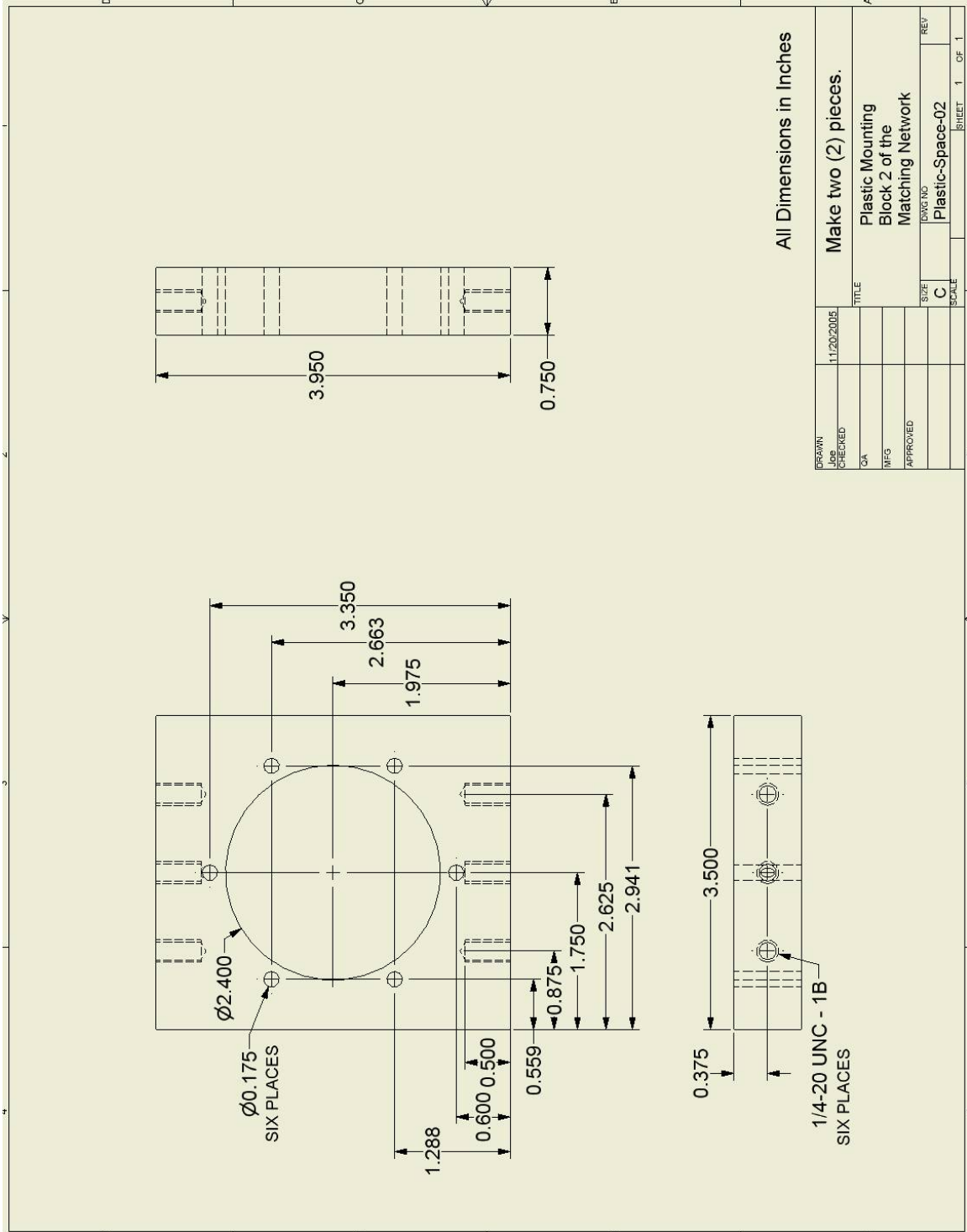


**A.B.06** Support 3 of the Mechanical Support Structure

All Dimensions in Inches

DRAWN	11/13/2005				
CHECKED	Joe				
QA					
MFG					
APPROVED					
SIZE					
SCALE					
TITLE		Make Two (2) Pieces			
REV		Support 3 of the Mechanical Support Structure			
DWG NO		Frame-Support-3			
C		1			
SHEET		1 OF 1			





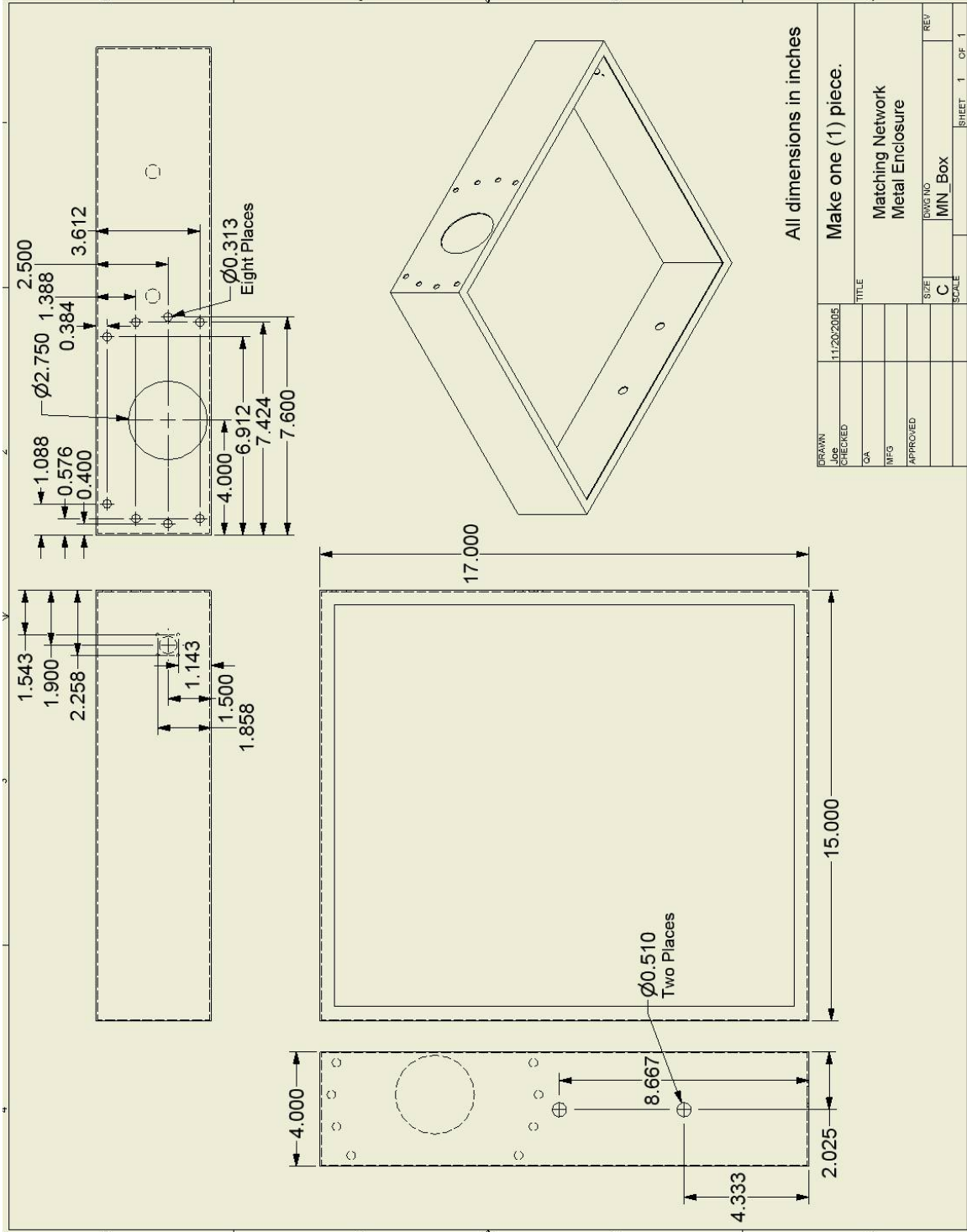
All Dimensions in Inches

DRAWN	11/20/2005	TITLE	Plastic Mounting Block 2 of the Matching Network
Job CHECKED		Make two (2) pieces.	
QA		Plastic-Space-02	
MFG		SIZE C	
APPROVED		DWG. NO.	REV
		SCALE	SHEET 1 OF 1

A.B.08 Plastic Mounting Block 2 of the Matching Network







A.B.10 Matching Network Metal Enclosure

# Appendix C

## Physical Constants

Boltzmann constant  $k = 1.3807 \times 10^{-23} \left[ \frac{J}{K} \right] = 1.3807 \times 10^{-23} \left[ \frac{kgm^2}{Ks^2} \right]$  (NRL,15)

Elementary charge  $|e| = 1.6022 \times 10^{-19} [C]$  (NRL,15)

Electron mass  $m_e = 9.1094 \times 10^{-31} [kg]$  (NRL,15)

Proton mass  $m_p = 1.6726 \times 10^{-27} [kg]$  (NRL,15)

Avogadro's number  $N_A = 6.0221 \times 10^{23} \left[ \frac{molecules}{mole} \right]$  (NRL,16)

Mass of Hydrogen Atom  $H_2$   $m_{H_2} = 2m_p + 2m_e = 3.3470 \times 10^{-27} [kg]$

Speed of light in vacuum  $c = 2.9979 \times 10^{10} [cm/sec]$  (NRL,17)

Atomic weight of H  $A = 1.00794$  amu

Specific heat of H2 at const pressure  $c_p = 28.836 \left[ \frac{J}{molK} \right] = 14.304 \left[ \frac{J}{gK} \right]$  (CRC)

Adiabatic index ( $\kappa$ ) for H2  $\kappa = 1.4$



# Appendix D

## Useful Conversions and Relations

$$\left[ T = \frac{kg}{s^2 A} \right], [C = As], [1T = 10^4 G], [1000cm^3 = 1L], [2\pi \text{ radians} = 1 \text{ cycle}], f = \frac{1}{T}$$
$$\omega = 2\pi f, \mu_m = m_i / m_p, [11,605 \text{ deg } K = 1eV], 2.54[cm / in], \left[ J = \frac{kgm^2}{s^2} \right], \left[ N = \frac{kgm}{s^2} \right],$$
$$[Nm = J], \left[ Pa = \frac{kg}{ms^2} \right], c_p - c_v = \frac{R}{M_{Gas}}, [1atm = 101.325kPa], [1Pa = 0.0075torr],$$
$$[1atm = 760torr]$$